The Astrophysical Journal, 933:172 (33pp), 2022 July 10 https://doi.org/10.3847/1538-4357/ac755b

Cosmological Results from the RAISIN Survey: Using Type Ia Supernovae in the Near Infrared as a Novel Path to Measure the Dark Energy Equation of State

D. O. Jones[1,24], K. S. Mandel[2], R. P. Kirshner[3,4], S. Thorp[2], P. M. Challis[4], A. Avelino[4], D. Brout[4,24], C. Burns[5], R. J. Foley[1], Y.-C. Pan[6], D. M. Scolnic[7], M. R. Siebert[1], R. Chornock[8], W. L. Freedman[9], A. Friedman[10], J. Frieman[9], L. Galbany[11,12], E. Hsiao[13], L. Kelsey[14], G. H. Marion[15], R. C. Nichol[14], P. E. Nugent[8,16], M. M. Phillips[17], A. Rest[18,19], A. G. Riess[18,19], M. Sako[20], M. Smith[21], P. Wiseman[22], and W. M. Wood-Vasey[23]

[1] Department of Astronomy and Astrophysics, University of California, Santa Cruz, CA 92064, USA; david.jones@ucsc.edu
[2] Institute of Astronomy and Kavli Institute for Cosmology, Madingley Road, Cambridge, CB3 0HA, UK
[3] Gordon and Betty Moore Foundation, 1661 Page Mill Road, Palo Alto, CA 94304, USA
[4] Harvard-Smithsonian Center for Astrophysics, 60 Garden Street, Cambridge, MA 02138, USA
[5] Observatories of the Carnegie Institute for Science, 813 Santa Barbara Street, Pasadena, CA 91101, USA
[6] Graduate Institute of Astronomy, National Central University, 300 Zhongda Road, Zhongli, Taoyuan 32001, Taiwan
[7] Department of Physics, Duke University, Durham, NC 27708, USA
[8] Department of Astronomy, University of California, Berkeley, CA 94720, USA
[9] Department of Astronomy & Astrophysics & Kavli Institute for Cosmological Physics, University of Chicago, 5640 South Ellis Avenue, Chicago, IL 60637, USA
[10] 1 Center for Astrophysics and Space Science, University of California San Diego, La Jolla, CA 92093, USA
[11] Institute of Space Sciences, Campus UAB, Carrer de Can Magrans, s/n, E-08193 Barcelona, Spain
[12] Institut d'Estudis Espacials de Catalunya (IEEC), E-08034 Barcelona, Spain
[13] Department of Physics, Florida State University, 77 Chieftain Way, Tallahassee, FL 32306, USA
[14] Institute of Cosmology and Gravitation, University of Portsmouth, Portsmouth, PO1 3FX, UK
[15] University of Texas at Austin, 1 University Station C1400, Austin, TX 78712-0259, USA
[16] Lawrence Berkeley National Laboratory, 1 Cyclotron Road, Berkeley, CA, 94720, USA
[17] Carnegie Institution of Washington, Las Campanas Observatory, Casilla 601, Chile
[18] Department of Physics and Astronomy, The Johns Hopkins University, Baltimore, MD 21218, USA
[19] Space Telescope Science Institute, Baltimore, MD 21218, USA
[20] Department of Physics and Astronomy, University of Pennsylvania, Philadelphia, PA 19104, USA
[21] Institut de Physique des Deux Infinis, Université de Lyon 1, CNRS/IN2P3, F-69622 Villeurbanne Cedex, France
[22] School of Physics and Astronomy, University of Southampton, Southampton, SO17 1BJ, UK
[23] Pittsburgh Particle Physics, Astrophysics, and Cosmology Center, Physics and Astronomy Department, University of Pittsburgh, Pittsburgh, PA 15260, USA

Received 2022 January 19; revised 2022 April 1; accepted 2022 May 31; published 2022 July 13

Abstract

Type Ia supernovae (SNe Ia) are more precise standardizable candles when measured in the near-infrared (NIR) than in the optical. With this motivation, from 2012 to 2017 we embarked on the RAISIN program with the Hubble Space Telescope (HST) to obtain rest-frame NIR light curves for a cosmologically distant sample of 37 SNe Ia ($0.2 \lesssim z \lesssim 0.6$) discovered by Pan-STARRS and the Dark Energy Survey. By comparing higher-z HST data with 42 SNe Ia at $z < 0.1$ observed in the NIR by the Carnegie Supernova Project, we construct a Hubble diagram from NIR observations (with only time of maximum light and some selection cuts from optical photometry) to pursue a unique avenue to constrain the dark energy equation-of-state parameter, w. We analyze the dependence of the full set of Hubble residuals on the SN Ia host galaxy mass and find Hubble residual steps of size ∼0.06-0.1 mag with $1.5\sigma - 2.5\sigma$ significance depending on the method and step location used. Combining our NIR sample with cosmic microwave background constraints, we find $1 + w = -0.17 \pm 0.12$ (statistical + systematic errors). The largest systematic errors are the redshift-dependent SN selection biases and the properties of the NIR mass step. We also use these data to measure $H_0 = 75.9 \pm 2.2$ km s^{-1} Mpc^{-1} from stars with geometric distance calibration in the hosts of eight SNe Ia observed in the NIR versus $H_0 = 71.2 \pm 3.8$ km s^{-1} Mpc^{-1} using an inverse distance ladder approach tied to Planck. Using optical data, we find $1 + w = -0.10 \pm 0.09$, and with optical and NIR data combined, we find $1 + w = -0.06 \pm 0.07$; these shifts of up to ∼0.11 in w could point to inconsistency in the optical versus NIR SN models. There will be many opportunities to improve this NIR measurement and better understand systematic uncertainties through larger low-z samples, new light-curve models, calibration improvements, and eventually by building high-z samples from the Roman Space Telescope.

Unified Astronomy Thesaurus concepts: Observational cosmology (1146); Hubble constant (758); Type Ia supernovae (1728)

1. Introduction

After five decades of development as cosmological distance probes (Kirshner 2010), Type Ia supernovae (SNe Ia) are now mature tools for understanding cosmic acceleration (Riess et al. 1998; Perlmutter et al. 1999), and systematic errors will soon become the largest source of uncertainty in the parameters of cosmic expansion (Betoule et al. 2014; Riess et al. 2016; Scolnic et al. 2018; Brout et al. 2019b; Jones et al. 2019;

---

[24] NASA Einstein Fellow.

Brout et al. 2022). In the optical bands, where most SN Ia data have been obtained, substantial deviations from the behavior of a standard candle are reduced by correcting for the observed relations between light-curve shape and luminosity (Pskovskii 1977; Phillips 1993; Hamuy et al. 1996; Riess et al. 1996; Guy et al. 2007; Jha et al. 2007; Conley et al. 2008; Mandel et al. 2011; Burns et al. 2014), reddening by dust (Riess et al. 1996; Phillips et al. 1999; Burns et al. 2014; Thorp et al. 2021; Mandel et al. 2022), and the intrinsically redder color of less luminous SNe Ia (Tripp 1998; Mandel et al. 2017).

However, SNe Ia have been found to be more nearly standard candles in the near-infrared (NIR; wavelengths covered by the rest-frame *zYJHK* bands), and their light is also less sensitive to the effects of dust extinction at these wavelengths (Krisciunas et al. 2004, 2007; Wood-Vasey et al. 2008; Mandel et al. 2009, 2011; Barone-Nugent et al. 2012; Phillips 2012; Avelino et al. 2019; Mandel et al. 2022). This paper reports an attempt to realize these advantages in a cosmologically distant SN Ia sample.

At low redshift, significant samples of SNe Ia have been observed in the NIR by the Carnegie Supernova Project (CSP-I; Contreras et al. 2010; Stritzinger et al. 2011; Krisciunas et al. 2017) at Las Campanas Observatory in Chile and the CfA Supernova Survey (Wood-Vasey et al. 2008; Friedman et al. 2015) using PARITEL at the F. L. Whipple Observatory in Arizona. NIR SN Ia light curves from SweetSpot (Weyant et al. 2018) using the WIYN telescope at Kitt Peak National Observatory in Arizona have also been assembled, and additional data from CSP-II (Hsiao et al. 2019; Phillips et al. 2019), the VISTA Extragalactic Infrared Legacy Survey (VEILS),[25] UKIRT (Konchady et al. 2022), and the Hubble Space Telescope (HST) through the SIRAH program (HST-GO 15889; PI: Jha) are forthcoming.

Measurements of the dark energy equation-of-state parameter, w, require comparing low-z SNe to those at larger cosmological distances. Measurements of $z > 0.1$ SNe in the rest-frame NIR have only been obtained by Stanishev et al. (2018; four SNe) and Freedman et al. (2009). The only previous measurement of the dark energy equation of state using NIR data was the pioneering study of Freedman et al. (2009), who found $w = -1.05 \pm 0.13\,(\mathrm{stat}) \pm 0.09\,(\mathrm{sys})$ by comparing 21 low-z SNe to 35 high-z SNe using templates as red as the rest-frame I band with observations in YJ from the Magellan Baade telescope. This analysis was unable to apply a number of corrections that are now commonly included in cosmology analyses but were less well studied or entirely unknown at the time when Freedman et al. (2009) was published, including corrections for distance (Malmquist) biases and the dependence of Hubble residuals on host galaxy mass (Kelly et al. 2010; Lampeitl et al. 2010; Sullivan et al. 2010).

Though high-z NIR SN Ia observations are rare, the value of NIR data is clear from low-z analyses. Avelino et al. (2019) used CSP-I and CfA data to show in head-to-head comparisons of the same SNe that the scatter in the distances as measured in the infrared is smaller by 35% than distances determined from optical light curves. Studies such as Wood-Vasey et al. (2008), Mandel et al. (2009), Kattner et al. (2012), and Mandel et al. (2022) have also shown evidence that SNe at NIR wavelengths yield more precise distance measurements.

Low-z NIR data have recently been used to demonstrate a significant relationship between SN Ia distance residuals and the mass of the SN Ia host galaxy (Uddin et al. 2020; Ponder et al. 2021), which was originally discovered at optical wavelengths (Kelly et al. 2010; Lampeitl et al. 2010; Sullivan et al. 2010), although Johansson et al. (2021) found mildly conflicting results with no evidence for a mass step in the JH bands and $\sim 2\sigma$ evidence for a step in the Y band. Burns et al. (2018) and Dhawan et al. (2018) used NIR data to measure the Hubble constant, H_0, using this new SN Ia wavelength range to provide additional evidence for tension between Cepheid+SN distance ladder measurements of H_0 (e.g., Riess et al. 2021) and the cosmic microwave background (CMB; Planck Collaboration et al. 2020).

With the advent of the Nancy Grace Roman Space Telescope, developing the optimal ways to measure NIR distances at cosmological redshifts is now urgent. Although Roman will observe SNe Ia primarily at rest-frame optical wavelengths at maximum redshifts up to $\gtrsim 2.5$ (Hounsell et al. 2018), Roman SN Ia observations will be in the rest-frame NIR in the important regime at $z \lesssim 0.7$, where baryon acoustic oscillation constraints will be limited by the cosmic volume (Weinberg et al. 2013).

Here we present NIR cosmological parameter measurements from the RAISIN survey. RAISIN (an anagram for "SNIA in the IR") used 23 SNe Ia discovered in the Medium Deep Survey (MDS) of Pan-STARRS (Chambers et al. 2016) in Hawaii and another 23 discovered by the Dark Energy Survey (DES) at Cerro Tololo Inter-American Observatory in Chile (The Dark Energy Survey Collaboration 2005). We triggered Hubble Space Telescope observations of those objects with WFC3-IR using the F125W and F160W filters. After applying a number of well-motivated cuts to the data, we use 42 low-z SNe Ia from CSP-I (hereafter CSP) and 37 high-z ($z > 0.2$) SNe Ia from RAISIN to measure w.

In this work, we pursue an "NIR-only" cosmological analysis that uses a different wavelength range than previous cosmological analyses with SNe and will have reduced systematic uncertainties due to dust. An optimal combination of optical+NIR data would yield the most precise cosmological constraints, but we show that an NIR-only analysis offers additional independent distance information. Throughout this paper we enumerate areas that will be improved to shrink these errors in future NIR studies and compare our results to a combined optical+NIR measurement.

In Section 2 we describe the RAISIN data, including survey properties, classifications, and photometric measurements. In Section 3 we describe our analysis method. In Section 4 we present our baseline cosmological results, and in Section 5 we discuss additional analysis variants and measure the correlation of Hubble residuals with host galaxy mass. In Section 6 we discuss the implications of our results for future missions such as the Roman Space Telescope. In Section 7 we conclude.

2. The RAISIN Sample

2.1. Overview and Strategy

The RAISIN program was carried out in cycle 20 through HST-GO 13046 (hereafter RAISIN1; PI: Kirshner) and cycle 23 through HST-GO 14216 (hereafter RAISIN2; PI: Kirshner). RAISIN1 followed 23 spectroscopically classified SNe from the Pan-STARRS MDS (Chambers et al. 2016), and RAISIN2

---

[25] https://www.eso.org/sci/publications/announcements/sciann17237.html

followed 23 spectroscopically classified SNe from DES (The Dark Energy Survey Collaboration 2005). RAISIN1 observed SNe in the redshift range of $0.22 \leqslant z \leqslant 0.50$ and RAISIN2 observed SNe at $0.35 \leqslant z \leqslant 0.61$ to observe at redshifts where the available HST filters overlap with the rest-frame *YJH* filters to minimize *K*-correction uncertainties. The median redshifts of PS1 and DES SNe aligned well with these targeted redshift ranges.

Due to occasional poor weather during PS1 and DES observing seasons and the need for HST template imaging after each SN had faded, RAISIN observations for each program extended over a period of 1.5−2 yr; RAISIN1 observations were taken from 2012 October 29 to 2014 June 17, and RAISIN2 observations occurred from 2015 September 28 to 2017 November 21.

To select RAISIN candidates, we identified Pan-STARRS and DES SNe that were likely to be SNe Ia discovered before maximum light. These candidates were then classified spectroscopically; classifications for MDS and DES SNe were carried out either by the RAISIN team in collaboration with the survey teams or by the MDS or DES teams themselves. For RAISIN1, we selected candidates that had been discovered by the Pan-STARRS team and were consistent with having a light-curve phase approximately 5−10 days before maximum light. For RAISIN2, we similarly selected candidates based on their apparent light-curve phase and additionally required that the photometric redshifts of their host galaxies were consistent with the target redshift range of $\sim 0.5 \pm 0.1$.

Most classifications were from Magellan (16 SNe) and Gemini South (13 SNe), with additional classifications from Gemini North (four SNe), the MMT (six SNe), the AAT (three SNe), and Keck (three SNe). Each classification was determined using the SN IDentification software (SNID; Blondin & Tonry 2007), which uses cross-correlation matching to template SNe to yield SN types, light-curve phases, and redshifts. Representative spectra for RAISIN targets are shown in Figure 1. Spectroscopically classified SNe Ia with rising light curves within the target redshift range were submitted to STScI for scheduling as nondisruptive targets of opportunity on HST. To improve the distance measurement, two additional epochs were obtained for each SN after the initial HST observation, spaced by approximately 5 rest-frame days. Template images for each SN were taken at least 6 months after the initial observations, with the exception of a single SN for which no template was needed because it was located in a region with no apparent galaxy light.

2.2. Ground-based Data and Photometry

2.2.1. The Pan-STARRS Medium Deep Survey

The Pan-STARRS MDS, the source of RAISIN1 SNe, observed 70 $\deg^2$ in *griz* filters over approximately 4 yr, with *gr*, *i*, and then *z* observations on successive nights. MDS also observed in the *y* filter, primarily during bright time, but the signal-to-noise ratio (S/N) of *y*-band observations for objects in our targeted redshift range was too low to be of use for SN Ia cosmology. Approximately 5200 SNe were discovered across the 4 yr of the MDS, with over 3000 host galaxy redshifts measured (Jones et al. 2017). A total of 520 SNe were spectroscopically classified during the survey, with ∼350 of these being SNe Ia and having a median redshift of ∼0.35 (Scolnic et al. 2018). Cosmological parameter measurements from these data are presented in Scolnic et al. (2018) for the spectroscopically classified sample and in Jones et al. (2018b) for the full sample. Further details regarding the MDS are given in Chambers et al. (2016).

The optical photometry for RAISIN1 comes from the Pantheon cosmological analysis (Scolnic et al. 2018), with the exception of five SNe that were not included in Scolnic et al. (2018).[26] Light curves of those five SNe were published by Villar et al. (2020) and are included in the data release that accompanies this paper. Pan-STARRS SN photometry is from `Photpipe` (Rest et al. 2005), with details specific to the MDS given in Rest et al. (2014) and Scolnic et al. (2018). In brief, MDS images are astrometrically aligned, and their zero-points are measured using the PS1 catalog. PS1 zero-points have been calibrated to a 3 mmag relative precision across the sky (Schlafly et al. 2012; Scolnic et al. 2015; Brout et al. 2021). Single-season, inverse-variance-weighted template image stacks are then convolved and subtracted from the nightly images, and SNe are discovered and their light curves subsequently measured by performing DAOPHOT forced photometry on the resulting difference images (Stetson 1987).

2.2.2. The Dark Energy Survey

DES observed in *griz* filters over 27 $\deg^2$ with a cadence of approximately once per week. These 27 $\deg^2$ were split into eight 2.7 $\deg^2$ "shallow" fields, with depths of ∼23.5 mag, and two "deep" fields, with depths of ∼24.5 mag. DES spectroscopically classified 251 SNe Ia at redshifts $0.02 < z < 0.85$ (Abbott et al. 2018). After sample cuts, their 3 yr spectroscopic sample includes 207 SNe Ia at a median redshift of $z = 0.36$. Cosmological parameter measurements from the DES spectroscopic sample are given in Abbott et al. (2018), with additional publications describing the calibration (Burke et al. 2018; Lasker et al. 2019), primarily based on observations of the CALSPEC standard star C26202, bias corrections (Kessler et al. 2019), photometry (Brout et al. 2019a), spectroscopic classification (Smith et al. 2020), and systematic uncertainties (Brout et al. 2019b) of these data.

For RAISIN2, DES SN discovery uses a difference imaging procedure similar to the MDS, but final optical photometry is carried out using the scene-modeling algorithm presented in Brout et al. (2019a). Scene modeling (Holtzman et al. 2008) uses imaging data to build a pixel-based model of the galaxy +SN that is convolved with each night's measured point-spread function (PSF) model. The amplitude of the SN is allowed to vary epoch to epoch, while the galaxy brightness is fixed. The robustness of the algorithm has been tested with artificial sources and recovers fluxes to an accuracy of 3 mmag.

2.2.3. The Carnegie Supernova Project

There are two sources of well-sampled low-*z* NIR SN Ia data, the CfA and CSP samples (Friedman et al. 2015; Krisciunas et al. 2017). These were combined to yield a sample of 89 low-*z*, NIR-observed SNe in Avelino et al. (2019). However, most CfA SNe either are at redshifts where the effect of peculiar flows dominates the distance uncertainty ($z \lesssim 0.01$)

---

[26] SN 520107 has a large shape uncertainty, while SN 470240 has an unusually blue optical color but passes the NIR-based cuts in Table 1. The other three SNe, SN 480794, SN 540087, and SN 540118, appear to pass standard cosmology cuts and were used for the cosmological analysis in Jones et al. (2018b).

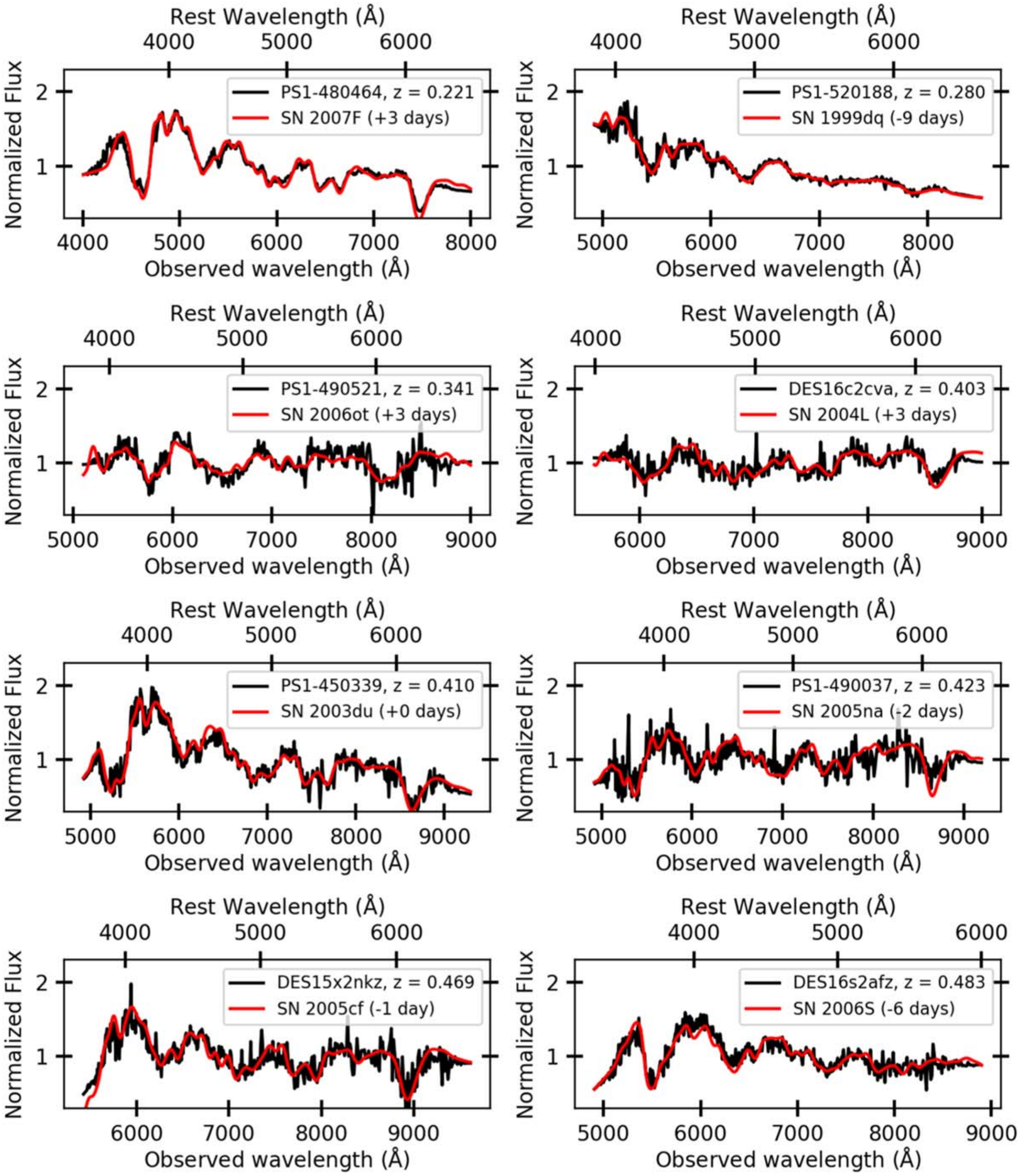

Figure 1. Representative classification spectra for RAISIN SNe (black) with the best template matches from SNID (red). Though the template match to PS1-490521 (SN 2006ot) is a peculiar Ia, the SNID matches to normal SNe Ia are also excellent.

or lack data prior to maximum light, which makes the determination of the time of maximum light uncertain and increases distance uncertainties. Therefore, we restrict ourselves to the CSP data for the low-z SN sample used in this work, although the CfA data remain extremely useful for training SN standardization models in the NIR. The release of CSP-II data in the near future will add an additional 125 SNe with NIR light curves and 90 SNe with NIR spectra (Hsiao et al. 2019; Phillips et al. 2019).

CSP uses DAOPHOT (Stetson 1987) to measure natural-system photometry on SN images after a template image, taken once the SN light has faded, has been subtracted. CSP images are calibrated with respect to primary standards BD +17°4708 (optical bandpasses) and Vega (NIR), with additional details given in Krisciunas et al. (2017).

2.2.4. Spectroscopic Classifications and Redshifts

Spectroscopic classifications and SN redshifts for each RAISIN SN were determined using SNID (Blondin & Tonry 2007). SNID determines a classification quality through a combination of the overlap between the observed spectrum and a template spectrum (*lap*) and the height of the cross-correlation peak (r). We ensure that the best template match has an $rlap > 5$, indicating a good match, and that the top three spectroscopic matches are all normal SNe Ia. For SN PS1-520107, the classification was unclear, so we remove this SN

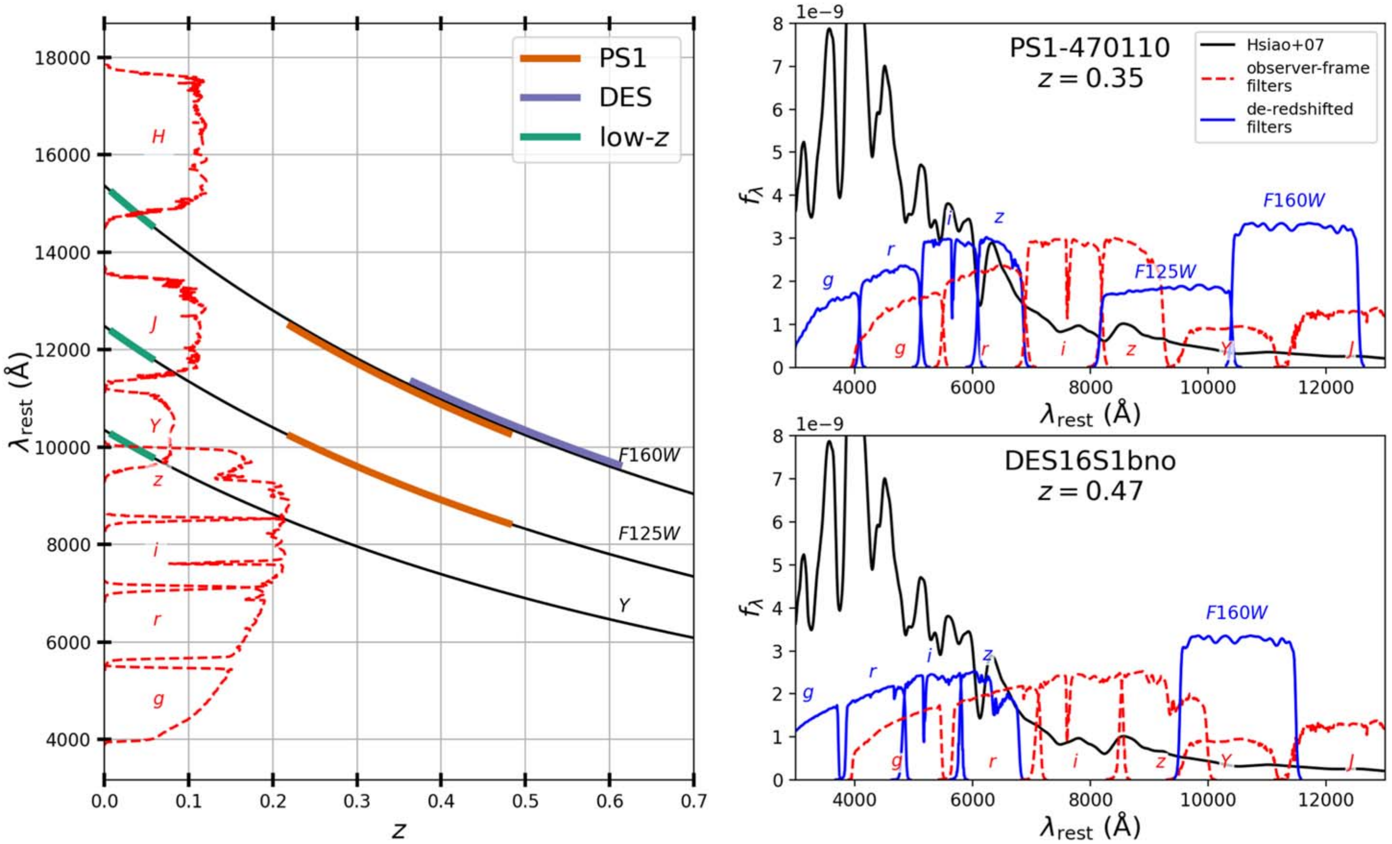

Figure 2. Rest-frame wavelengths probed by RAISIN observations as a function of redshift. Left: rest-frame wavelengths corresponding to the observer-frame *Y*, F125W (HST's *J* band), and F160W (HST's *H* band) as a function of redshift, with the low-*z*, RAISIN1 (PS1) and RAISIN2 (DES) redshift ranges highlighted. The shapes of *grizYJH* filter throughputs (red; arbitrary units) are shown for illustration. Right: de-redshifted (solid blue) and observer-frame (dashed red) filters for the median-redshift RAISIN1 (top) and RAISIN2 (bottom) SNe. The Hsiao et al. (2007) model (black) is shown for illustration.

from our sample. For SN PS1-490521 the best-matched spectrum was to the peculiar SN Ia 2006ot, but, as discussed in Section 3.4, we choose to include 06bt- and 06ot-like SNe in our cosmology analysis, as they cannot be reliably classified (or ruled out) from noisier high-*z* spectra.

The PS1 and DES teams measured host galaxy redshifts for these objects using cross-correlation matches to galaxy templates. For PS1, redshifts were estimated using the `rvsao` package (Kurtz & Mink 1998), and for DES the `Marz` package was used (Hinton et al. 2016).

For CSP classifications and redshifts, see Krisciunas et al. (2017) and references therein. SN classifications were measured from SNID, as well as SN redshifts. As discussed in Krisciunas et al. (2017), all CSP SNe have host galaxy redshifts, and nearly all of these are measured from the NASA/IPAC Extragalactic Database (NED[27]). We also use updated group redshifts from the Pantheon+ analysis (Scolnic et al. 2021) for SN 2005al and SN 2009ab, which differ significantly from the values in the latest CSP data release.

2.3. HST Data and Photometry

The HST data for RAISIN1 SNe were taken with three epochs each of F125W (approximately the *J* band) and F160W (approximately the *H* band). For RAISIN2 SNe, only the F160W band was used for most SNe; five RAISIN2 SNe included data in both filters. Figure 2 illustrates the rest-frame wavelengths probed by the HST data as a function of redshift.

The first HST observations occurred at a median of 12.2 observer-frame days relative to *B*-band maximum light for RAISIN1 (+9.2 rest-frame days) and 13.9 observer-frame days (+9.5 rest-frame days) for RAISIN2 owing to the time required for SN discovery, classification, and the latency in the HST scheduling. The median S/N is 12.5 for RAISIN1 and 12.9 for RAISIN2, with template observations taken at an average of 189 days after the first SN detection. See Appendix A for a discussion of how we correct for a small amount of late-time SN flux in some template images.

Examples of RAISIN observations are shown in Figure 3. Optical photometry and spectra of these SNe are provided in the online data release accompanying this paper to allow these measurements to be of use in future NIR analyses such as SIRAH (HST-GO 15889).

Our team measured photometry from the RAISIN images according to the following steps:

1. For each epoch, FLT images, which are images that have been bias-subtracted, dark-subtracted, and flat-fielded, are drizzled[28] together, and the final (template) epoch is subtracted.
2. We then measured SN centroids from the difference images and performed 0$''$.4 aperture photometry on the

---

[27] The NASA/IPAC Extragalactic Database (NED) is funded by the National Aeronautics and Space Administration and operated by the California Institute of Technology.

[28] "Drizzling" refers to the process of linearly reconstructing an image from undersampled, dithered data (Fruchter & Hook 2002).

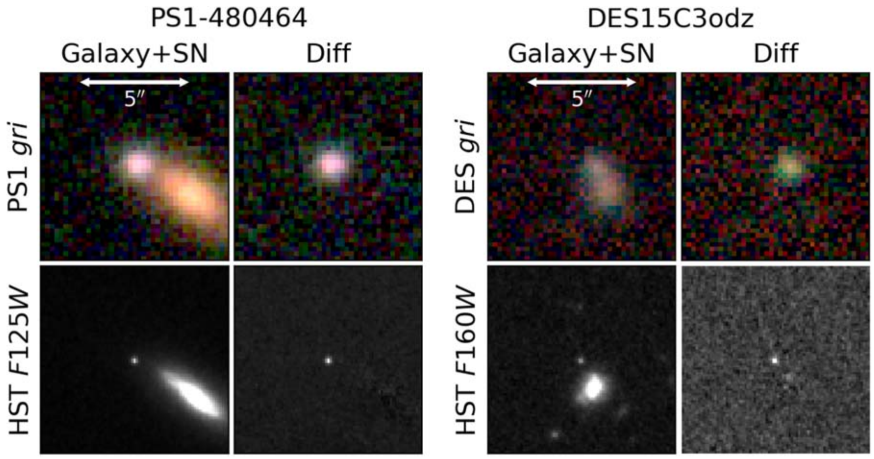

Figure 3. Stamp images of RAISIN SNe from Pan-STARRS (left) and DES (right) with *gri* images (top) and RAISIN images from HST (bottom). The SN location is centered in each image.

difference images with aperture corrections from HST. We verified these aperture corrections using drizzled images of the CALSPEC standard star P330E.

3. Using artificial stars injected into the data frames, we corrected the resulting measurements and uncertainties for host galaxy noise.
4. We calibrated the data using publicly available zeropoints that were measured from observations of four white dwarf standards (GD153, G191B2B, GD71, GRW +70D5824) and the G-type star P330E.[29]

We describe these steps in additional detail in Appendix A. Coordinates of the RAISIN SNe and the final RAISIN photometry are given in Appendix B.

3. Analysis

In this section, we describe the NIR light-curve models we used (Section 3.1), present our method for distance measurements (Section 3.2), create a dispersion model to measure distance-dependent biases (Section 3.3), apply sample selection cuts (Section 3.4), measure the dependence of distance on host galaxy mass (Section 3.6), and estimate each source of systematic uncertainty in our NIR measurement of w (Section 3.7). Our cosmological parameter measurements are then presented in Section 4.

3.1. NIR Light-curve Models

SN Ia standardization models rarely make use of the NIR owing to the small number of well-calibrated, high-cadence NIR light curves. In the past decade, only the SALT2 (Guy et al. 2007, 2010) and SiFTO (Conley et al. 2008) light-curve fitters have been used for measurements of w, with SALT2 being by far the most common model. SALT2, however, extends only to a central filter wavelength of approximately 7000 Å, with the recently developed SALT3 model (Kenworthy et al. 2021) now extending this wavelength to 8700 Å to include the rest-frame z band.

However, there are now two well-vetted light-curve models extending to the NIR: the SNooPy model (Burns et al. 2011, 2014) and the BayeSN model (Thorp et al. 2021; Mandel et al. 2022). SNooPy benefits from over a decade of use by the community and includes light-curve templates for the *uBVgriYJH* bands that have been trained using well-calibrated CSP light curves. BayeSN is a hierarchical Bayesian spectral energy distribution (SED) model for SNe Ia (BayeSN) that models time-dependent optical−NIR (to 1.8 μm) SN Ia SEDs as a combination of physically distinct intrinsic spectral components and host galaxy dust effects. By having an SED-based model continuous in both time and wavelength, BayeSN removes the need to compare high-redshift photometric data to an approximate rest-frame filter and effectively allows a K-correction that varies with light-curve stretch. At the same time, BayeSN has yet to be integrated in publicly available tools like SNANA (Kessler et al. 2010), so the simulation of distance-dependent biases for a cosmology analysis is not yet feasible.

Though we incorporate both SNooPy and BayeSN in our analysis, we use SNooPy as our baseline method owing to the greater ease of determining distance biases and because BayeSN was under development during the time when much of this analysis was carried out. The advantages of BayeSN's statistical framework are somewhat mitigated owing to the limited number of NIR observational epochs in the RAISIN data. Still, we find good consistency between the distance measurements from these two models, as demonstrated in Section 5.2.1; we plan to use BayeSN in a future optical+NIR analysis of these data.

3.1.1. SNooPy Model Philosophy

The SNooPy model philosophy assumes that the observed variation in SN colors is caused by extinction in the SN host galaxy but allows the selective-to-total extinction ratio R_V to be specified by the user—the nominal method in this analysis—or fit by the data. We also allow SNooPy to fit negative extinctions for a more agnostic treatment of SN color; SNooPy assumes the luminosity versus color relationship to be linear with no minimum value (the same philosophy as the Tripp relation; Tripp 1998). This effectively means that R_V should be interpreted as a luminosity versus color trend in this work, rather than a physical dust law.

SNooPy also includes options to correct for the dependence of SN luminosity on light-curve shape. We adopted the "EBV_model2," which uses the s_{BV} parameter to determine the relation between SN light-curve shape and luminosity

---

[29] https://www.stsci.edu/hst/instrumentation/wfc3/data-analysis/photometric-calibration/ir-photometric-calibration

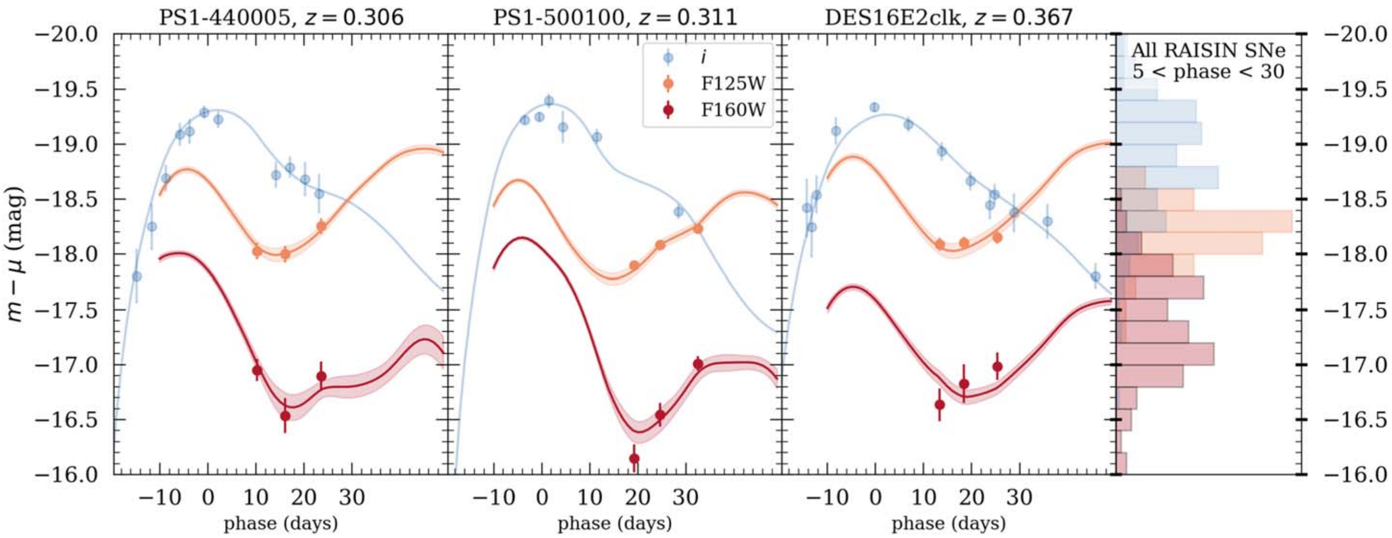

Figure 4. Examples of RAISIN SN light curves. Apparent magnitude minus distance modulus (a proxy for absolute magnitude) versus phase is shown for three RAISIN SNe with observations in i (PS1 or DES), F125W, and F160W. Solid lines show the SNooPy model fit to the data. The optical bands, including i, are used to estimate the time of maximum light, while the HST NIR bands are used to measure the distance (we allow s_{BV} fitting to show the best-fit NIR model in this example). Histograms with approximate absolute magnitude distributions for all RAISIN SNe are shown on the right after applying the sample selection cuts discussed in Section 3.4.

(Burns et al. 2018). The s_{BV} parameter is a stretch parameter that is insensitive to extinction because it takes advantage of the fact that the delay between time of maximum light and the time of reddest color is insensitive to reddening (Lira et al. 1998). To enable easier determinations of distance biases and systematic uncertainties in later stages of the analysis, we incorporated this SNooPy model into the SNANA software (Section 3.5; Kessler et al. 2010) and used the SNooPy *iYJH* templates generated from low-z CSP data to fit our NIR data and measure distances. Example RAISIN light curves with SNooPy fits are shown in Figure 4.

3.2. Distance Measurement Method

Because RAISIN NIR light curves include just three post-maximum light epochs per SN, we are unable to make robust shape and color corrections or determine the time of maximum light from NIR data alone; we find a Hubble residual rms of 0.24 mag when fitting A_V and 0.28 mag when fitting s_{BV} from NIR-only RAISIN data (in Appendix C, we will use simulations to confirm that larger rms values are expected given the small number of post-maximum light epochs per SN).

Therefore, our nominal distance measurement approach is to use the SNooPy model to fit *only* the NIR SN amplitude; we use optical data to determine the time of maximum light and fix the SN shape and color to a nominal value.[30] This approach yields a Hubble residual rms of 0.18 mag.

We relax either the NIR-only aspect of this analysis or the nominal approach of fitting only the amplitude of the NIR data—i.e., not fitting s_{BV} or A_V—in several places in this analysis as described below:

1. **Selection cuts**. Optical data are used to make sample selection cuts to remove SNe with high values of $E(B-V)$, which cannot be estimated from NIR data alone. This is discussed in Section 3.4.
2. **Time of maximum light**. Because we do not have NIR data near maximum light in the high-z sample, we must use optical data to constrain the phase of the SN observations.
3. **Scatter model**. SNe Ia were discovered and spectroscopically classified at optical wavelengths, so we determine the consequence of these selection effects on our sample. To estimate distance-dependent selection effects for the SNooPy model, we use optical+NIR CSP data to estimate the covariance matrix of the distance residuals after estimating and correcting for s_{BV} and A_V. This is described below in Section 3.3.
4. **Bias corrections**: To determine and correct for the redshift dependence of the intrinsic populations of s_{BV}, we fit s_{BV} using the NIR data. Though the resulting Hubble residual scatter increases, as discussed above, this is a useful tool to compare data distributions of s_{BV} to simulated distributions of s_{BV}. This is described in Appendix C.
5. **Wavelength dependence of the mass step**. In Section 5.1, we compare estimates of the host galaxy mass step between optical and NIR data in a self-consistent manner that accounts for the correlation between s_{BV} and galaxy mass. Therefore, in this section we will correct the NIR Hubble residuals for their dependence on the optical+NIR-measured s_{BV} parameter. We use both the SNooPy derived s_{BV}—NIR luminosity correlation and the directly measured dependence of our NIR Hubble residuals on s_{BV}. An s_{BV}-corrected mass step is not used for cosmological parameter estimation but only to investigate the physics and wavelength dependence of the mass step.
6. **Comparing to optical and optical+NIR measurements of w**. In Section 4.1, we compare the baseline results to results that fit the SNooPy model to optical and optical +NIR data.

---

[30] We adopt arbitrary values of $s_{BV} = 1$ and $A_V = 0$ for simplicity, as the bias correction stage will adjust the derived distances for the average s_{BV} and A_V of the data themselves. We have confirmed that adjusting the nominal value of these parameters in the distance fits does not change the scatter by more than ∼0.01 mag.

3.3. Dispersion Model and Distance Biases

Because we compare SNe Ia across a large span of redshift, we must determine distance-dependent biases, which are caused by the increased likelihood of discovering higher-luminosity SNe at larger redshifts in magnitude-limited surveys; these can be up to ∼5% in distance for the PS1 and DES samples (Scolnic et al. 2018; Brout et al. 2019b). To determine these biases, we build a dispersion covariance matrix from the optical to NIR to understand the ways in which optical SN Ia selection effects—which are caused by PS1 and DES selection criteria—affect distances measured in the NIR.

Because there has been no measurement of the covariance in magnitude between different SNooPy bands, we estimated this model from the low-z CSP data in our sample. To generate this model, we use low-z SNe at $0.015 < z < 0.1$ to ensure that the results are minimally dependent on cosmological parameters while also mitigating the effect of peculiar velocity uncertainties at $z < 0.015$ (Peterson et al. 2021).

We then simultaneously fit the SNooPy model to all the optical and NIR bands in the low-z CSP sample to estimate the time of maximum light, s_{BV}, and A_V for each SN. Keeping these parameters fixed, we then fit the low-z data with the SNooPy model for each of the $BVgriYJH$ bands individually. We use the resulting Hubble residuals in each band to generate a band-to-band covariance matrix that can be used to generate large Monte Carlo simulations and determine wavelength-dependent distance biases. We note that the additional distance scatter predicted from a peculiar velocity uncertainty of 250 km s^{-1} (Scolnic et al. 2018) is smaller than the scatter observed in each band at the median redshift $z = 0.023$, and we find that the observed optical-to-NIR covariances are very similar when restricting the sample to $z > 0.025$ or $z > 0.03$.

The resulting covariance matrix is shown in Figure 5 and is now included in the public SNANA software.[31] We find similar dispersion measurements in most bands, with values ranging from ∼0.116 to 0.136 mag; the maximum dispersion is in the H band, and the minimum is in Y, but the band-to-band differences are not highly significant in this sample. Covariance is on the order of ∼0.015 mag^2 between neighboring optical bands (correlations of $\gtrsim$0.95) and ∼0.010 mag^2 between NIR-to-NIR and optical-to-NIR bands (correlations of ∼0.78−0.86). These correlations can be understood as the correlation between Hubble residuals measured using one band at a time. Slightly higher correlations are found when we examine the Uddin et al. (2020) data, which might be due to the exclusion of fast-declining, red, and low-z SNe in the present analysis. NIR-derived distances in our sample are well correlated with optical distances—implying a significant wavelength-independent component of SN Hubble residual scatter—but are less correlated with optical bands than optical bands are with each other, implying that NIR data contain additional information useful for constraining SN Ia distances.

3.4. Sample Selection Cuts

Next, we apply selection cuts to our sample to ensure that each SN has well-measured photometry and distances. First, as discussed in Appendix A.1, we remove five SNe with host galaxy noise contributions that add greater than 0.1 mag to the photometric errors, based on an injected star analysis, as these are indications of subtraction residuals. Due to PSF variation caused by the breathing of HST, it is difficult to have clean subtractions on galaxies that are bright relative to the SN; this is because even few-percent variations in the PSF when multiplied by a bright galaxy core can cause large residuals relative to the brightness of the SN. This PSF variation will unavoidably bias our sample against SNe in high surface brightness environments, making it even more important to better characterize the SN–host galaxy environment correlation. We visually inspect each difference image to ensure that the remaining SNe appear to have high-quality subtractions. We also remove SN PS1-520107, which has an unclear spectroscopic classification. We note that SN 2006bt is peculiar (Foley et al. 2010), but we chose to include it for consistency across the redshift range, as similar events would be impossible to identify and exclude in our high-z sample given the noisier spectra at those redshifts. However, SN 2006bt subsequently fails Chauvenet's criterion (see below). We further remove SNe that lack either optical or NIR data before maximum light, as this makes it impossible to accurately determine the phase of a given observation. We also ensure that pre-maximum light data exist both before and after removing $>10\sigma$ SNooPy light-curve fit outliers from the data; if an SN had a misidentified time of maximum light, we found that an SN could appear to have pre-maximum light data when in reality it did not, but this issue was fixed once we removed outlying data points from the fit.

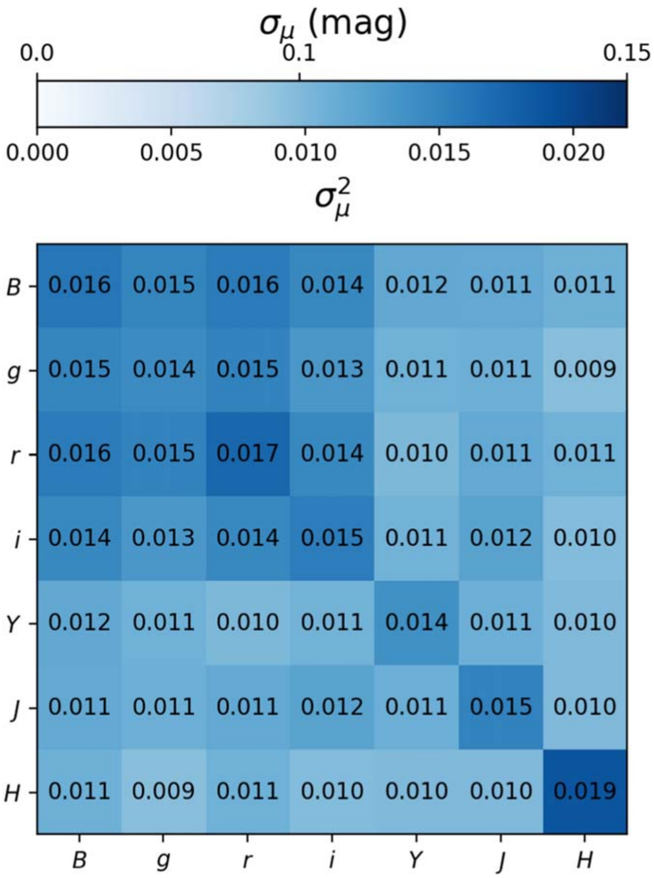

	B	g	r	i	Y	J	H
B	0.016	0.015	0.016	0.014	0.012	0.011	0.011
g	0.015	0.014	0.015	0.013	0.011	0.011	0.009
r	0.016	0.015	0.017	0.014	0.010	0.011	0.011
i	0.014	0.013	0.014	0.015	0.011	0.012	0.010
Y	0.012	0.011	0.010	0.011	0.014	0.011	0.010
J	0.011	0.011	0.011	0.012	0.011	0.015	0.010
H	0.011	0.009	0.011	0.010	0.010	0.010	0.019

Figure 5. Optical-to-NIR covariance matrix for the SNooPy model computed from CSP data (similar to Figure 6 of Mandel et al. 2011), with covariance values labeled and the top axis of the color bar indicating the uncertainties on the diagonal in each band. After shape and color correction, we found the maximum dispersion to be ∼0.15 mag in the optical bands and the minimum to be ∼0.12 mag in the Y band.

---

[31] https://snana.uchicago.edu/

Table 1
RAISIN Cuts

	CSP DR3		RAISIN1		RAISIN2	
	$N_{\rm cut}$	$N_{\rm rem}$	$N_{\rm cut}$	$N_{\rm rem}$	$N_{\rm cut}$	$N_{\rm rem}$
	⋯	134	⋯	23	⋯	22
$\sigma_{\rm host} < 0.1$ mag	0	134	2	21	3	19
Spec. SN Ia	0	133	1	20	0	19
$z > 0.01$	21	116	0	20	0	19
Pre-max	22	92	0	20	0	19
Pre-max, χ^2 cut	35	57	0	20	0	19
NIR data	8	49	0	20	0	19
SNooPy fitting	0	49	0	20	0	19
$E(B-V) < 0.3$	1	49	0	20	0	19
$0.75 < s_{BV} < 1.18$	4	45	1	19	0	19
$\sigma(s_{BV}) < 0.2$	2	43	0	19	0	19
Chauvenet	1	42	0	19	1	18

Note. The effect of selection cuts on the low-z and RAISIN data sets. These include requiring (1) photometric uncertainty from bright hosts $<$ 0.1 mag, including systematic uncertainty due to subtraction residuals; (2) spectroscopic confirmation that the SN is Type Ia; (3) redshift $>$ 0.01, to limit peculiar velocity errors; (4) data taken before maximum light, before removing points with $\chi^2 > 10$ from the light-curve fit; (5) data taken before maximum light, after removing those points (see text); (6) existence of NIR data; (7) successful convergence of the fit to the SNooPy light-curve model; (8) $E(B-V) < 0.3$; (9) values for the s_{BV} parameter that indicate a normal SN Ia light curve; and (10) two remaining Hubble diagram outliers (SN 2006bt, DES15C1nhv) that fail Chauvenet's criterion (see text).

Next, we remove SNe measured to have $E(B-V) >$ 0.3 mag from optical data. Though only a single SN in our sample fails this cut, these SNe could in principle cause large outliers on our NIR-only Hubble diagram given that we perform light-curve fits with fixed A_V. High-A_V SNe could also have some sensitivity to differences in R_V that are difficult to measure owing to the extrinsic/intrinsic degeneracy in SN colors (e.g., Mandel et al. 2022). We also remove SNe with extreme values of the s_{BV} parameter that are not well represented in the SNooPy training sample. These include $s_{BV} > 1.18$ and $s_{BV} < 0.75$, values for which SNooPy is not well trained. Cutting at $s_{BV} > 0.75$ also excludes 91bg-like and transitional SNe Ia (see Burns et al. 2014; Gall et al. 2018), which removes SNe that would be poorly standardized by our baseline method that does not fit for s_{BV}. At $s_{BV} > 1.18$ in particular, only a single high-stretch SN is included in the SNooPy model training. SNe with s_{BV} measurement uncertainties >0.2 are also removed, as we cannot reliably estimate whether they pass cuts. Finally, two SNe—SN 2006bt and DES15C1nhv—fail Chauvenet's criterion as 2.8σ and 3.1σ outliers on the Hubble diagram. A sample of 38 objects (the high-z sample) is expected to have just 0.07 3.1σ (or greater) outliers on average, and a sample with 44 objects (the CSP sample) is expected to have just 0.2 $>2.8\sigma$ outliers; both numbers are below the Chauvenet threshold of 0.5. We treat the low- and high-z distributions differently in this calculation, as they have substantially different photometric data coverage and scatter (Section 5.2.2).

The full set of distances, light-curve parameter measurements (using optical data), and cuts on those data for both the low-z and RAISIN samples are given in Appendix E. For each subsample, selection cuts are summarized in Table 1.

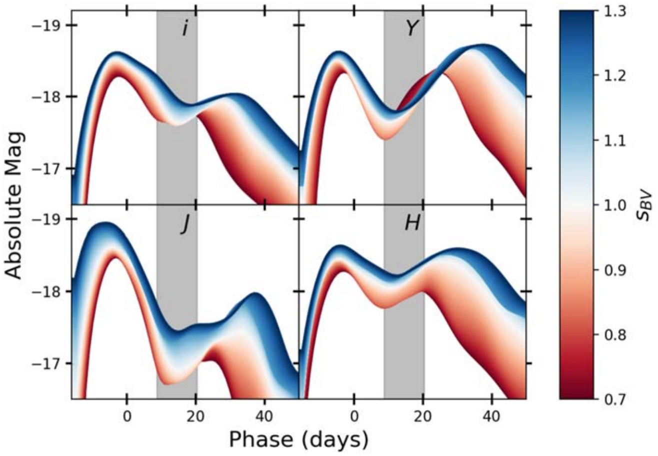

Figure 6. SNooPy model *iYJH* light curves as implemented in SNANA and as a function of the color-stretch parameter, s_{BV}. The rest-frame *Y*-band model in particular has very little sensitivity to s_{BV} at the epochs of the RAISIN data. The phase range within which 68% of RAISIN observations fall are shown in gray bands (for CSP the 68% range covers phases from $\sim$−3 to 40 days).

3.5. Simulations and Bias Corrections

Using the dispersion model from Section 3.3, we use the SNANA (Kessler et al. 2010) simulation framework to generate realizations of each subsample in this analysis (CSP, RAISIN1, and RAISIN2). SNANA is the "industry standard" tool for accurately simulating large SN Ia samples for cosmological parameter measurements, and for this reason both the MDS and DES teams have already developed sophisticated SNANA simulations of their surveys that yield accurate realizations of their survey data. SNANA includes sky noise, survey zero-points, survey cadences, host galaxy properties, realistic shape and color distributions for the SN population, and the quantitative criteria that were used to trigger follow-up observations.

These simulations are presented in Appendix C. In brief, we based our simulations on preexisting CSP (Kessler et al. 2019), PS1 (Scolnic et al. 2018), and DES (Kessler et al. 2019) simulations, but we applied them to a SNooPy model that we implemented within the SNANA framework (Figure 6). We then estimated intrinsic population distributions of the s_{BV} values using the aggregate NIR data, and although NIR data are only weakly dependent on A_V, we simulate a nominal exponential A_V scale of $\tau = 0.2$ mag and vary this scale length in our systematic error budget. This exponential scale is well matched to our measurements from optical observations, from which we estimate $\tau \simeq 0.15-0.18$ mag; preliminary optical +NIR analysis of the RAISIN sample from BayeSN also gives $\tau = 0.21 \pm 0.04$.

The simulations then give the distance bias: the average difference between simulated and measured distance as a function of redshift, shown in Figure 7. We correct the measured distances for the average bias at each SN redshift. The predicted optical distance biases have similar sizes to bias corrections generated for the Pantheon analysis (Scolnic et al. 2018) using the Guy et al. (2010) optical scatter model and the SALT2 standardization model. The NIR bias corrections are dominated by the difference in mean stretch and A_V between the low- and high-z samples. The uncertainties on the differences in these distributions are used to determine systematic uncertainties on the bias corrections.

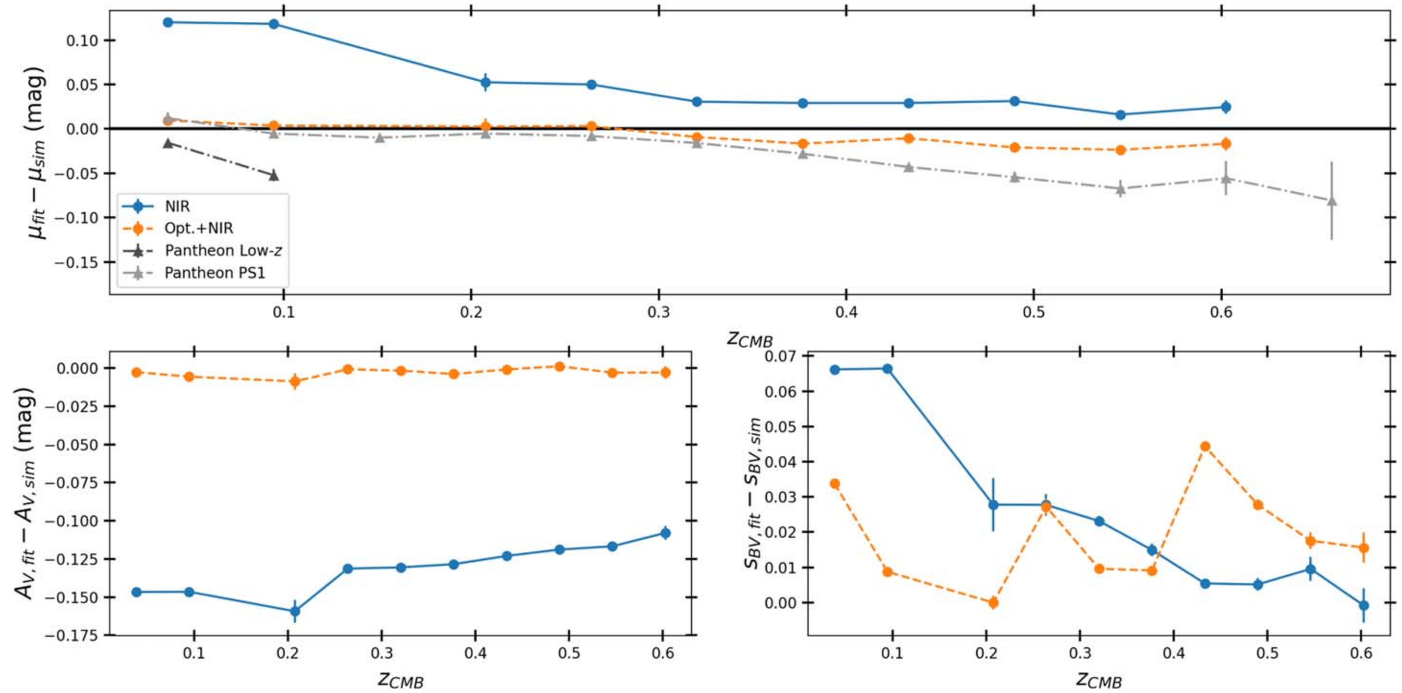

Figure 7. Distance biases (top), A_V biases (bottom left), and s_{BV} biases (bottom right) as a function of redshift. Results are shown for both the NIR-only light-curve fits (blue), which assume zero reddening and $s_{BV} = 1.0$, and the optical+NIR fits (orange), which include A_V and s_{BV} as free parameters. Predicted low-z (black triangles) and PS1 (gray triangles) distance biases from Pantheon are also shown in the top panel. Some bin-to-bin fluctuation in the bias corrections as a function of redshift is caused by simulating SNe at only the exact redshifts of RAISIN objects for a smaller, more computationally efficient simulation.

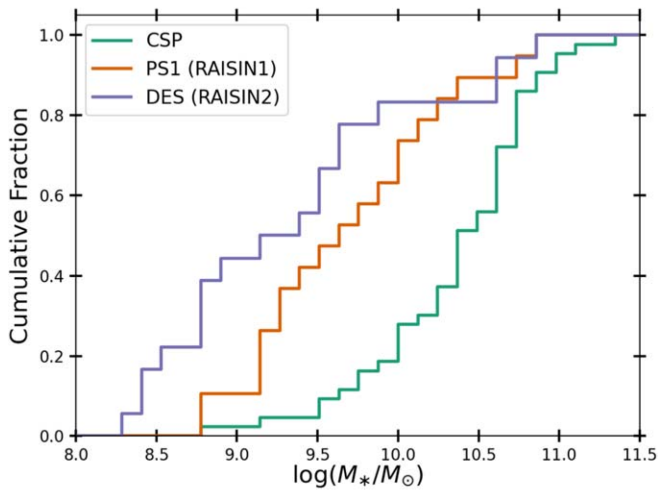

Figure 8. Cumulative fraction of SNe as a function of host galaxy mass for CSP and RAISIN SNe. CSP SNe are found in significantly more massive host galaxies.

3.6. Host Galaxy Mass Dependence

The step-like dependence of SN Hubble residuals on host galaxy mass has been well established (Kelly et al. 2010; Lampeitl et al. 2010; Sullivan et al. 2010), and recently there have been reported—but somewhat conflicting—detections of the host mass step in the NIR (Uddin et al. 2020; Johansson et al. 2021; Ponder et al. 2021). Constraining the wavelength dependence of the mass step could help to distinguish among theories for the origin of the step, e.g., dust properties (Brout & Scolnic 2021) versus progenitor metallicity (Rose et al. 2021b). We attempt to measure and correct for a host galaxy mass step in the RAISIN data. We measure host galaxy masses ourselves to ensure consistency across the sample using a procedure described in Appendix D. We simultaneously estimate the mass step and the average Hubble residual in three redshift bins to ensure that our measurement is independent of cosmological parameters. The resulting masses are shown in Figure 8.

3.7. Systematic Uncertainties

We treat systematic uncertainties in much the same way as previous cosmological analyses (e.g., Scolnic et al. 2018; Brout et al. 2019b; Jones et al. 2019): we determine 1σ uncertainties in data and analysis parameters (e.g., peculiar velocities, Milky Way (MW) reddening, calibration, and bias corrections), apply each systematic to the data or analysis, and construct a covariance matrix of the distances resulting from each analysis choice or data modification. The systematic uncertainty covariance matrix is then added to the (diagonal-only) statistical covariance matrix. The systematic uncertainty covariance matrix is given by

$$C_{sys}^{jk} = \sum_{n=1}^{N} \frac{\partial f(z_j)}{\partial S_n} \frac{\partial f(z_k)}{\partial S_n} \sigma^2(S_n) \qquad (1)$$

for a given set of systematics S_n applied to each light curve or distance measurement. For the nth systematic, $\frac{\partial f(z_j)}{\partial S_n}$ is the change in distance after applying systematic S_n to an SN at redshift z_j. The size of each systematic uncertainty is given by $\sigma(S_n)$.

Details about individual systematic uncertainties are given below. Compared to previous analyses, our choice of the SNooPy model and the limited sample size allows us to omit a few second-order systematic uncertainties, including redshift evolution in nuisance parameters and redshift evolution of the host galaxy mass step. We also do not include the choice of

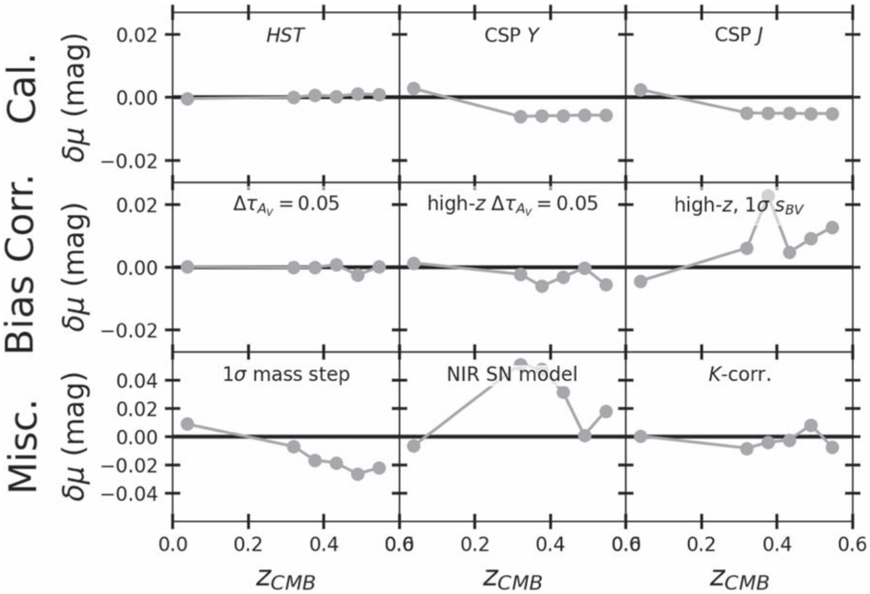

Figure 9. Selected systematic shifts in distance modulus as a function of redshift for this analysis, grouped into calibration systematics (top), bias correction systematics (middle), and other systematics (bottom). The systematics shown in the middle panel are a shift in the scale length of the A_V distribution (left), a shift in the scale length of the A_V distribution for the high-z data only (middle), and 1σ shifts in the high-z stretch distribution parameters (right). The systematics shown in the bottom panel are due to the uncertainty in the size of the mass step (left), the SNooPy model (middle), and K-correction uncertainties (right). The weighted average of each distance vector is subtracted to show relative low- to high-z differences, even if the systematic only changes the distances in one part of the redshift range. For visualization purposes, only bins with at least three SNe are shown to reduce noise while illustrating z-dependent trends.

SN Ia dispersion model as a systematic uncertainty because we have constrained this directly from the low-z Hubble diagram itself. We are therefore not subject to the G10/C11 scatter model degeneracy that causes significant uncertainties in optical-only analyses (e.g., Brout et al. 2019b). The redshift dependence of a subset of our systematic uncertainties is shown in Figure 9.

3.7.1. Calibration

This analysis is limited to two photometric systems, HST and CSP (the Swope telescope). The HST CALSPEC calibration affects both the RAISIN and low-z data sets, while the CSP calibration to CALSPEC affects only the low-z data. The CALSPEC calibration was updated in Bohlin et al. (2020), with the revised uncertainty in the F125W and F160W bands now at the level of 0.5%. The CSP calibration is from Krisciunas et al. (2017); the JH calibration is tied to Vega, while the optical calibration is tied to observations of BD +17° 4708. We have updated the optical CSP zero-points using the latest CALSPEC spectra of BD +17°4708[32]. The CSP JH calibration is uncertain at the level of approximately 2%, and we apply independent 2% JH systematic errors to the CSP magnitudes as a conservative estimate. We also assume a larger, 3% systematic error for the Y-band calibration, as it was calibrated to Castelli & Kurucz (2003) atmospheric models rather than Persson standards (Persson et al. 1998; Krisciunas et al. 2017). Better calibration of low-z samples in the future will enable improved ground-based, NIR measurements.

3.7.2. Bias Corrections

The uncertainty in the host galaxy bias corrections is dominated by uncertainty in the intrinsic distributions of s_{BV} and A_V in our samples. The method of Scolnic & Kessler (2016) gives 1σ uncertainties on the derived population parameters, and we recompute bias corrections after varying the s_{BV} distribution parameters for the low-z and high-z data by their 1σ uncertainties. The population parameters after 1σ variations are shown in Appendix C. We include two additional extinction variants: first, we reduce the exponential scale length by 0.03 in $E(B-V)$ (from 0.13 to 0.1), and second, we reduce the exponential scale length of the extinction distribution by 0.03 in $E(B-V)$ for *only* the CSP sample. These $E(B-V)$ shifts are equivalent to a shift in mean A_V of 0.05 for our default $R_V = 1.52$ or 0.1 for $R_V = 3.1$; they are greater than the measured difference in mean A_V between the low- and high-z samples when optical+NIR data are used in the fitting.

3.7.3. NIR SN Standardization Model

We substitute BayeSN distances for SNooPy distances to estimate the systematic error in the SNooPy NIR SN Ia standardization model. Though BayeSN has not yet been implemented in SNANA, e.g., bias corrections cannot yet be estimated, we can still compare the uncorrected distances after fitting the RAISIN and low-z data with BayeSN. To ensure that the BayeSN distances are fit in the same way as the SNooPy distances, we keep the A_V and shape parameter fixed to values equivalent to the SNooPy values of $A_V = 0$ and $s_{BV} = 1$ (BayeSN $A_V = 0$, $\theta \simeq -1$), and we apply the SNooPy bias corrections to the BayeSN distances, making the assumption that the SNooPy bias corrections remain valid for BayeSN measurements. SNooPy and BayeSN distances are well correlated (see further discussion in Section 5.2.1), and the average Hubble residual between the low- and high-z samples changes by just 2 mmag when using BayeSN instead of SNooPy.

---

[32] Available at https://archive.stsci.edu/hlsps/reference-atlases/cdbs/current_calspec/

3.7.4. Mass Step

We adopt two variants of the host galaxy mass step. In the first, we shift the mass step by its 1σ uncertainties from the maximum likelihood approach described in Appendix D. In the second, we adopt the NIR mass step location suggested by Ponder et al. (2021) of 10.44 dex: we measure the mass step at a location of 10.44 dex, recompute the step, and reapply the step to the data.

3.7.5. K-corrections

Because the Hsiao et al. (2007) model is used to generate SNooPy's *K*-corrections, use of the SNooPy model requires an understanding of the uncertainties in *K*-corrections due to the limited number of SNe that were used to construct the Hsiao et al. (2007) model. To create a model for *K*-corrections with realistic uncertainties, we create composite spectra following the method of Siebert et al. (2019) using a limited number of individual NIR spectra from the Infrared Telescope Facility (Marion et al. 2009, with data from G. H. Marion, private communication) that were used to create the original Hsiao et al. (2007) template. Composite spectra are created at phases of approximately −9, −3, +7, +15, and +39 days, epochs that match the phases of the individual spectra themselves, and then bootstrap-resampled 50 times to create estimated uncertainties. The +15-day composite spectrum is within a few days of the epoch of most RAISIN NIR data.[33] We then use the shape of the Hsiao et al. (2007) template light curve at each wavelength to interpolate between the phases covered by the composite spectra and use a Savitzky−Golay algorithm to smooth over the telluric regions. We then assume that those uncertainties are representative of the uncertainties on the Hsiao et al. (2007) model and shift the model by the standard deviation of the bootstrap-resampled spectra. This will result in a systematic change in the measured distances caused by the statistical uncertainty in the Hsiao et al. (2007) model, particularly at high redshift.

We note some small slope differences between the Hsiao et al. (2007) template and our composite spectra but find good consistency overall. We also inspect the SN 2011fe NIR spectra from Hsiao et al. (2013)—an SN with somewhat narrower than average stretch—and see some broadband color differences that could be attributed to relative calibration errors in the spectra or perhaps intrinsic variation between SNe. Methods such BayeSN, which effectively has an SN stretch-dependent *K*-correction, are capable of modeling this intrinsic variation. Future, well-sampled, public NIR spectral databases will reduce this systematic uncertainty and are an important area to improve future analyses.

3.7.6. Peculiar Velocities and MW $E(B-V)$

We apply peculiar velocity and MW reddening systematics following Scolnic et al. (2018) and Jones et al. (2019). For MW $E(B-V)$, we reduce the Schlafly & Finkbeiner (2011) values by 5% according to the systematic uncertainty in the dust temperature correction. For peculiar velocities, we conservatively vary the mass-to-light bias parameter β in the 2M ++ cosmic flow maps by its 5σ statistical uncertainty (Lavaux & Hudson 2011).

3.8. Cosmological Parameter Measurements

We use a combination of CosmoMC (Lewis & Bridle 2002) and CosmoSIS[34] (Zuntz et al. 2015) with likelihood chains from Planck Collaboration et al. (2020), including temperature, polarization, and lensing, to measure cosmological parameters from the vector of SN distances and the systematic uncertainty covariance matrix. To measure SN-only constraints, we use CosmoMC to sample the likelihood, while for combining SNe with Planck, we use the CosmoSIS importance sampler to combine SN constraints with results from the Planck chains. Luminosity distances d_L from the *w*CDM model, in Mpc, are given by

$$d_L(z, w, \Omega_m, \Omega_\Lambda, \Omega_k) = (1+z)\frac{c}{H_0}\int_0^z \frac{dz}{E(z)},$$
$$E(z) = [\Omega_M(1+z)^3 + \Omega_k(1+z)^2 + \Omega_\Lambda(1+z)^{3(1+w)}]^{1/2}. \quad (2)$$

Here Ω_m, Ω_Λ, and Ω_k are the cosmic matter density, dark energy density, and spatial curvature, respectively. We use the following function to estimate cosmological parameters:

$$\chi^2 = (\hat{\mu} + \Delta\mathcal{M} - \mu_{w\mathrm{CDM}})C^{-1}(\hat{\mu} + \Delta\mathcal{M} - \mu_{w\mathrm{CDM}}), \quad (3)$$

where C is the covariance matrix from the combined statistical and systematic uncertainties, and $\hat{\mu}$ is the distance modulus measured from the data as described in Section 3.2 and including the bias corrections and host mass step as discussed in Sections 3.5 and 3.6. The model distance modulus $\mu_{w\mathrm{CDM}} = 5\log(d_L) - 5$. $\Delta\mathcal{M}$ is the offset between the assumed SNooPy absolute magnitude of an SN Ia, which is also degenerate with the assumed value of H_0, and the best-fit global value.

4. Results

After performing the analysis described in the previous section, we produce the RAISIN NIR-only Hubble diagram shown in Figure 10. The high-*z* distance measurements are presented in Appendix E. The total rms of the Hubble residuals is 0.167 mag, 18% higher than the Pantheon Hubble residuals. However, the CSP scatter for those SNe with NIR data near maximum light is 0.136 mag, slightly *lower* than the Pantheon scatter of 0.141 mag, showing the value of well-sampled NIR light curves near maximum light. Future samples with additional epochs near maximum light and a revised NIR model will reduce the scatter well below that achievable from optical data (Avelino et al. 2019). Additional data in the gap between the low-*z* and RAISIN redshifts would be particularly beneficial in creating an extended NIR Hubble diagram.

4.1. Ω_m and w

By using CosmoMC to constrain cosmological parameters from SNe alone, Figure 11 shows the constraints on nonflat CDM relative to Pantheon and the cosmic acceleration discovery sample from Riess et al. (1998). These data thereby confirm cosmic acceleration with high significance, using a

---

[33] We note that this is also near the epoch in which the *H*-band spectral break occurs (Hsiao et al. 2013), but this would only affect our low-*z* data, where *K*-corrections are small.

[34] https://bitbucket.org/joezuntz/cosmosis/wiki/Home

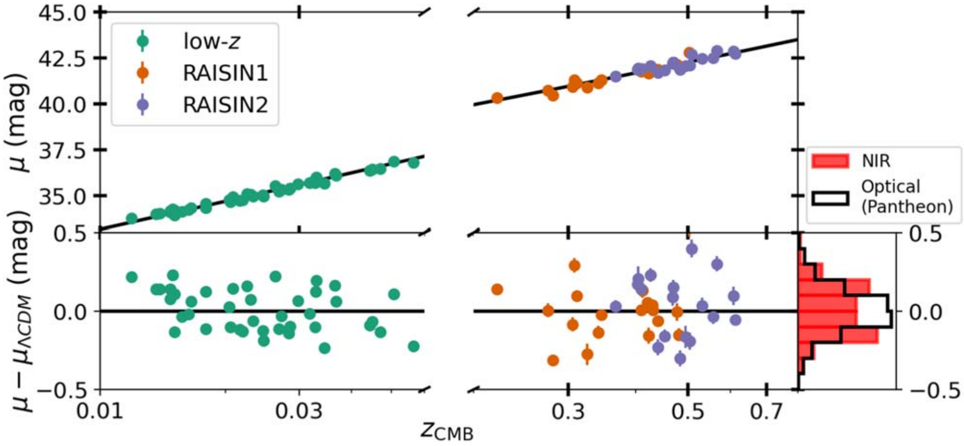

Figure 10. The RAISIN Hubble diagram, with low-z SNe from CSP (green) and high-z samples from RAISIN1 (orange) and RAISIN2 (purple). We show photometric uncertainties only, neglecting the contribution of intrinsic scatter for visual clarity.

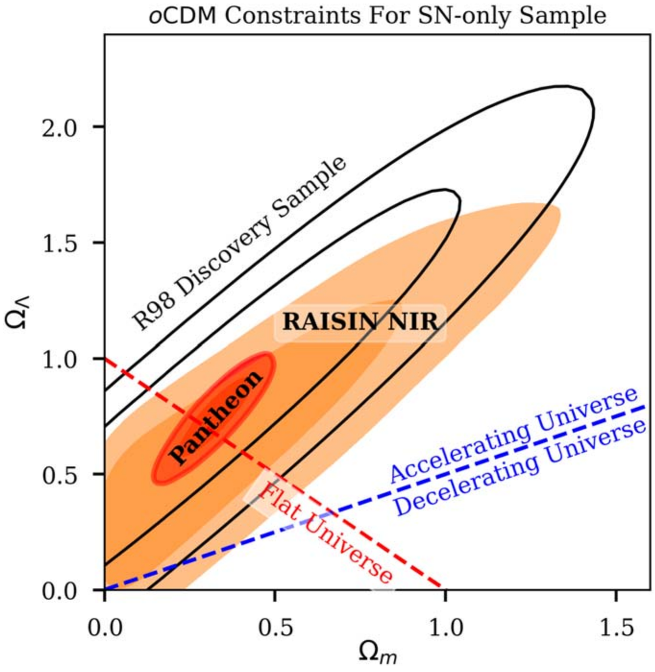

Figure 11. Cosmological parameter measurements from oCDM (a CDM model allowing nonzero curvature) with SNe alone. Open contours show the Riess et al. (1998) discovery sample, red contours show the Pantheon constraints from Scolnic et al. (2018), and the results from RAISIN SNe are in orange. All contours show the 68% and 95% confidence intervals.

new method and wavelength range that has less sensitivity to dust extinction uncertainties. In a flat universe, from RAISIN SNe alone, we find $\Omega_m = 0.258 \pm 0.090$.

With CMB constraints from Planck Collaboration et al. (2020) we find a dark energy equation of state of $1 + w = -0.17 \pm 0.12$ (Figure 12). This measurement is consistent with the previous NIR measurement from Freedman et al. (2009) of $1 + w = -0.05 \pm 0.13\,(\mathrm{stat}) \pm 0.09$ (sys) but with smaller uncertainties.

Statistical and systematic uncertainties in this analysis are approximately equal. The dominant systematic uncertainty in this measurement is the bias correction—predominantly due to uncertainty in the intrinsic s_{BV} distribution—which will improve with larger sample sizes and improved light-curve fitting methods. The second-largest systematic uncertainty is the size of the NIR mass step (Section 5.1), which will similarly improve with larger sample sizes. The full list of systematic uncertainties on the wCDM model is shown in Table 2 and visually in Figure 13. Though we have attempted to be comprehensive in our accounting of systematic uncertainties, we note that there may be substantial additional uncertainties in this novel measurement that will become more apparent only with larger sample sizes.

4.2. The Hubble Constant

In addition to measuring w, we measure H_0 with NIR SN data alone. We use Cepheid distances with CSP and RAISIN SN data to measure the Hubble constant from the distance ladder approach and use SN+CMB data to constrain the H_0 parameter with an "inverse distance ladder" approach (e.g., Cuesta et al. 2015) that combines the angular size of the CMB sound horizon with wCDM constraints from CSP, RAISIN, and Planck.

To measure H_0 from the distance ladder, we use publicly available Cepheid or tip of the red giant branch (TRGB) distances for all 10 SNe with CSP photometry and with independent TRGB or Cepheid measurements to calibrate the NIR luminosity of SNe Ia. Nine of these SNe—SN 2006D, SN 2007af, SN 2007on, SN 2007 sr, SN 2009Y, SN 2011iv, SN 2012fr, SN 2012ht, and SN 2015F[35]—have redshifts of $z < 0.01$ and therefore were not included in our baseline sample for measuring w. One SN, SN 2007A, was already included in our sample, as it has a redshift of $z = 0.017$.

We use a combination of available Cepheid and TRGB distance calibrations (Freedman et al. 2019; Anand et al. 2022; Riess et al. 2021) and take the agnostic approach of giving all available distances as originally provided equal weight. We use Cepheid distances from Riess et al. (2021) for five SNe: SN 2006D, SN 2007A, SN 2009Y, SN 2012ht, and SN 2015F. We use the mean of available Cepheid and TRGB distances for three SNe: SN 2007af (Freedman et al. 2019; Riess et al. 2021), SN 2007sr (Freedman et al. 2019; Anand et al. 2022; Riess et al. 2021), and SN 2012fr (Freedman et al. 2019; Anand et al. 2022; Riess et al. 2021). Finally, we use the mean TRGB distances for two SNe from Freedman et al. (2019) and

---

[35] Photometry for SN 2012fr is published in Contreras et al. (2018), photometry for SN 2012ht and SN 2015F is published in Burns et al. (2018), and photometry for SN 2011iv is published in Gall et al. (2018).

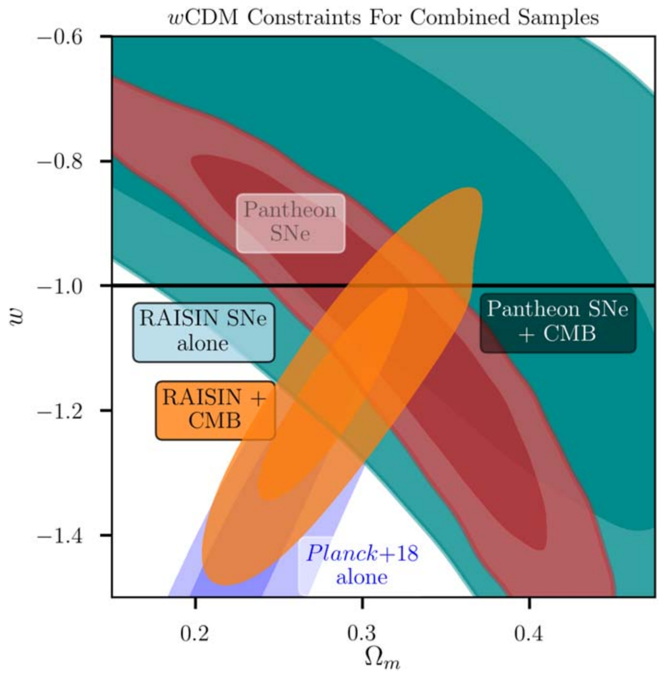

Figure 12. Cosmological parameter measurements from wCDM. RAISIN +CMB cosmological constraints (orange) are consistent with those from the Pantheon sample (black; Scolnic et al. 2018), with a statistically insignificant shift toward phantom dark energy ($w < -1$). All contours show the 68% and 95% confidence intervals.

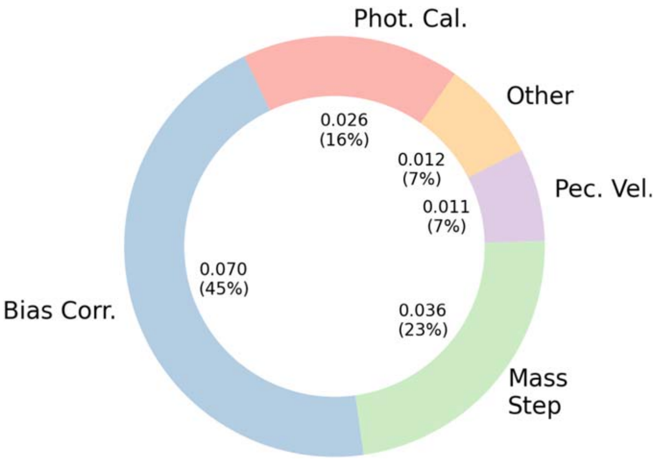

Figure 13. Summary of systematic uncertainties on w for the RAISIN cosmological analysis (Table 2). Bias correction and mass step uncertainties dominate the error budget, with photometric calibration and uncertainties in the peculiar velocities contributing significantly. Other systematic uncertainties are added in quadrature to give the "Other" contribution.

Table 2
Summary of Systematic Uncertainties on w from NIR Data Alone

Error	Δw	$\Delta\sigma_w$	$\sigma_{w,sys}/\sigma_{\rm stat}$
All sys.	−0.040	0.082	0.954
Bias corr.	−0.040	0.070	0.809
− s_{BV}	−0.040	0.069	0.805
− A_V	0.000	0.009	0.099
Mass step	−0.012	0.036	0.425
Phot. cal.	0.006	0.026	0.306
− Low-z	0.005	0.026	0.305
− HST	0.000	0.002	0.025
Pec. vel.	−0.017	0.010	0.110
NIR SN model	0.008	0.008	0.097
Template flux	0.008	0.008	0.097
MW $E(B-V)$	0.000	0.003	0.041
k-corr.	−0.002	0.002	0.026

Note. Summary of systematic uncertainties on the wCDM model with constraints from SNe+Planck. Δw is the shift in w resulting from applying each systematic uncertainty, and $\Delta\sigma_w$ is the additional uncertainty that would need to be added in quadrature to the statistical error to yield the uncertainty on w from a given variant. Note that some variants shift the value of w but do not increase its uncertainties.

Anand et al. (2022), SN 2007on and SN 2011iv, which are in the same host galaxy of NGC 1404. These two SNe are fast decliners (Gall et al. 2018 find $s_{BV} = 0.57 \pm 0.01$ and 0.64 ± 0.01 for SN 2007on and SN 2011iv, respectively), with decline rates below our nominal s_{BV} cuts, so we provide results with and without them.

We use these Cepheid and TRGB distances to calibrate the SN luminosity of the CSP and RAISIN samples following the method of Riess et al. (2021). If we include SN 2007on and SN 2011iv in our H_0 measurement, we measure $H_0 = 77.5 \pm 2.1$ km s^{-1} Mpc^{-1} from Cepheid+TRGB and $H_0 = 76.6 \pm 2.6$ km s^{-1} Mpc^{-1} from TRGB alone. Excluding the two fast-declining SNe in NGC 1404, however, we measure $H_0 = 75.9 \pm 2.2$ km s^{-1} Mpc^{-1} from Cepheid+TRGB and $H_0 = 72.9 \pm 3.0$ km s^{-1} Mpc^{-1} from TRGB distances alone. We note that the statistical significance of this TRGB measurement with a reduced sample is limited, as we have just three TRGB calibrator galaxies and the measurement is statistically consistent with other recent TRGB-based measurements (Freedman et al. 2019; Anand et al. 2022). The majority of the uncertainty derives from the error in the mean of the modest samples of NIR SN calibrators.

Because our distance measurement method does not correct for any dependence of SN luminosity on s_{BV} and our Hubble flow sample excludes such fast-declining objects (we require $s_{BV} > 0.75$), it is possible that these fast decliners, which make up a large fraction of the calibrator sample, could bias our results; therefore, our baseline result excludes the fast decliners.

From the inverse distance ladder in a wCDM model, we find a model parameter $H_0 = 71.2 \pm 3.8$ km s^{-1} Mpc^{-1} (Figure 14). The value of H_0 is consistent with the conventional result of 67.4 ± 0.5 assuming ΛCDM with Planck data alone. Independent approaches to measuring SN distances at cosmological redshifts such as this one demonstrate the ways in which future measurements can help determine what role, if any, the present dark energy could play in the tension between local (e.g., Riess et al. 2016; Huang et al. 2020; Pesce et al. 2020; Wong et al. 2020; Foreman-Mackey 2016; Riess et al. 2021) and CMB H_0 measurements (e.g., Dhawan et al. 2020).

Though the uncertainties on these measurements are large, we find that moving to NIR wavelengths does not appear to change the size of the difference between CMB and local H_0 measurements (see also Burns et al. 2018; Dhawan et al. 2018).

4.3. Comparing to Optical and Optical+NIR Measurements

Finally, Table 3 compares our NIR-only measurement of w to measurements using optical data alone and optical+NIR data from SNooPy. In computing the optical and optical+NIR measurements, we apply the same base set of systematic uncertainties but add calibration uncertainties at the level of 3 mmag for each PS1 band, 5 mmag for each DES band, and

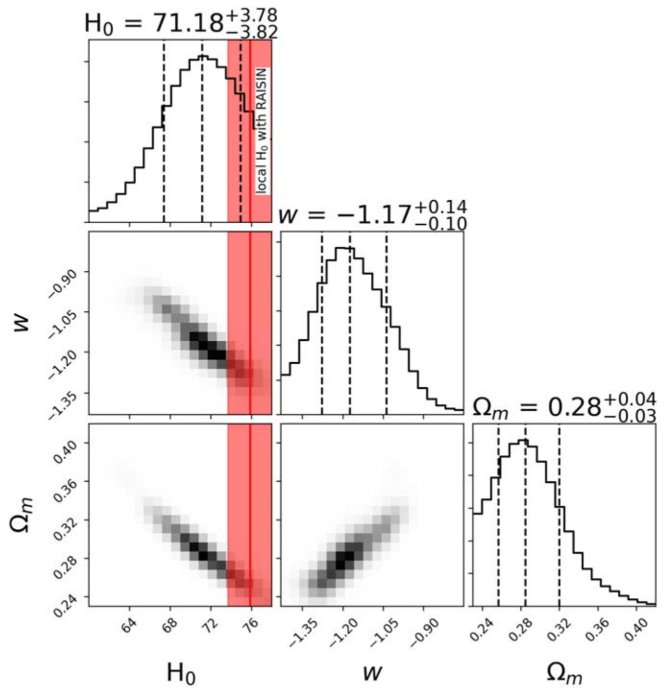

Figure 14. Constraints on H_0, w, and Ω_m from RAISIN and CMB data combined using an inverse distance ladder method. This figure was generated with the `corner` package (Foreman-Mackey 2016).

Table 3
Comparing Optical and NIR Measurements of w

	$w_{\rm stat}$	$w_{\rm stat+sys}$	$\sigma_{w,\rm sys}$	$\Delta\sigma_w/\sigma_{\rm stat}$
Opt. only	-1.099 ± 0.074	-1.102 ± 0.092	0.055	0.739
NIR only	-1.128 ± 0.086	-1.168 ± 0.119	0.082	0.956
Opt.+NIR	-1.043 ± 0.056	-1.059 ± 0.074	0.048	0.864

1% for each optical CSP band (Krisciunas et al. 2017; Burke et al. 2018; Scolnic et al. 2018).

Interestingly, we find substantial shifts when considering optical or optical+NIR data versus NIR data alone. In the NIR-only case versus the optical+NIR case in which NIR data primarily have the effect of constraining the SN color, w shifts by up to 0.11. Though the statistical significance of this shift is not entirely clear given the correlated data and some correlation in the systematic uncertainties, this shift could point to the need for revisions to the NIR or optical SN standardization model in future work, particularly given forthcoming surveys such as the Roman Space Telescope SN survey that will observe in the NIR (Rose et al. 2021a).

Although the sensitivity of the NIR-only measurement to bias correction uncertainties yields a result with significantly higher systematic errors in our baseline analysis, larger sample sizes would result in more precise bias estimations from a better constraint on the redshift-dependent stretch distribution of SNe. However, given that NIR-only approaches will always have difficulty constraining the potential evolution of dust extinction with redshift, we believe that the optimal approach in future work will be an optical+NIR measurement; Table 3 shows that this measurement has the lowest total systematic uncertainty budget of our three wavelength regimes. Though the overall improvement in the precision of w is small, we note that alternative distance measurement methods such as BayeSN (Mandel et al. 2022) appear to more optimally weight the NIR versus optical data and yield significantly reduced distance uncertainties when NIR data are included.

5. Exploring Alternative Analysis Methodologies and Constraining the Mass Step

In this section, we explore variations on our nominal analysis and examine potential systematic uncertainties in the cosmological parameter measurement.

5.1. The Mass Step

Using our nominal distance measurement method, we find a maximum likelihood size of the mass step of $\Delta_M = 0.022 \pm 0.047$ mag at a step location of 10 dex and 0.026 ± 0.040 mag at the Ponder et al. (2021) location of 10.44 dex (the step location is fixed during each fit). These results are used to generate the distance measurements in Section 4 above. However, the differences between the NIR and optical measurements are affected by the fact that stretch is correlated with host galaxy mass; our nominal distance method does not fit for stretch, and there is a median difference of $\Delta s_{BV} = -0.099$ between the high- and low-mass subsets of our sample. Correcting for this stretch differential, as done in an optical-only analysis, would have the effect of making the mass step larger.

To measure the mass step in a way that is more comparable to the way optical mass steps are measured, we test the impact of applying an s_{BV} correction to the NIR distances using the best-fit s_{BV} from optical+NIR data. We see a strong trend between Hubble residual and optical+NIR-derived s_{BV} as shown in Figure 15 and find that the scatter in our Hubble residuals is reduced by 10% by making this correction. We do not see a significant change in the dependence of Hubble residual on s_{BV} in the low-z data (slope -0.622 ± 0.189) compared to the high-z data (slope -0.702 ± 0.244).

After s_{BV} fitting, we measure a larger mass step, as we would predict, of 0.072 ± 0.041. This result is shown in Figure 16. If, instead, we use the location of the mass step from Ponder et al. (2021) of 10.44 dex, we find a mass step of 0.057 ± 0.035 mag. If we adopt the approximate linear, empirical correction between s_{BV} and Hubble residual shown in Figure 15, instead of using the default SNooPy s_{BV}–luminosity relation, we find consistent steps of 0.086 ± 0.043 mag and 0.094 ± 0.037 mag for 10 and 10.44 dex step locations, respectively. We conclude that there is $\sim 2\sigma$ evidence for a mass step in these data even if we do not a priori assume that the SNooPy luminosity–s_{BV} relation is correct.

Using the high-z data alone, we measure a mass step of 0.114 ± 0.081 mag at a step location of 10 dex and a step of 0.122 ± 0.091 mag at 10.44 dex. Unfortunately, the sample is too small to constrain the size of the step with these high-z data alone, which yield a statistically insignificant 1σ evidence for the NIR mass step.

If we use the optical data to measure the mass step with the same SNe, we find a step of 0.11 ± 0.03 mag from SNooPy and 0.08 ± 0.03 mag from SALT3 (the same step size is measured from SALT2). These are consistent with optical mass steps in the literature, which can range from 0.04 ± 0.019 mag from DES (Smith et al. 2020) to 0.119 ± 0.032 from the Nearby Supernova Factory (Aldering et al. 2002; Rigault et al. 2020);

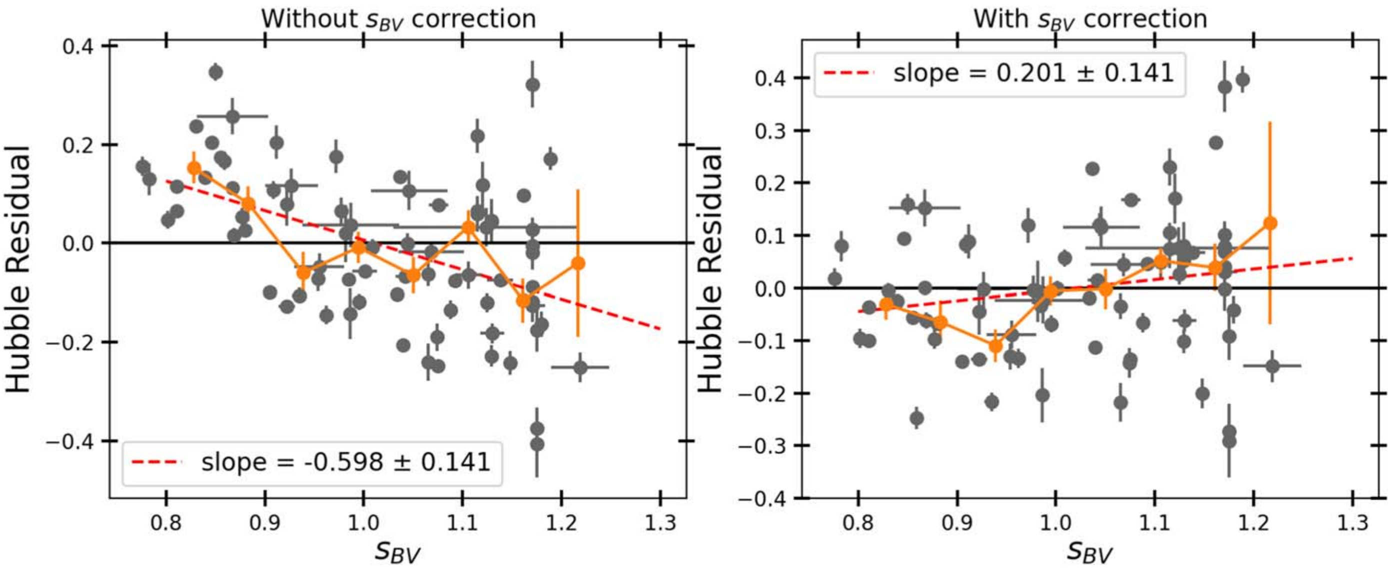

Figure 15. NIR Hubble residuals as a function of s_{BV}, before the Hubble residuals are corrected for s_{BV} (left) and after (right). Correcting for the marginally significant $\sim 2\sigma$ slope in the right panel would shift our high-z distances by just ∼0.015 mag.

the largest data set (Pantheon; Scolnic et al. 2018) yields a step of 0.072 ± 0.01.[36]

These mass step results qualitatively support—albeit with limited significance—the findings of Ponder et al. (2021) and Uddin et al. (2020), who also found evidence that the NIR mass step was of order the same size as the optical mass step.

5.2. Comparing to Alternative Distance Measurement Methods

5.2.1. NIR Distances from BayeSN

Although we have not yet simulated distance biases with the BayeSN SED model, we did compare our SNooPy distances before bias correction to raw BayeSN distances that assume a fixed stretch and zero host dust extinction A_V, analogous to the approach we adopted for SNooPy. We fix the BayeSN primary intrinsic component $\theta = -1$, approximately equivalent to our chosen SNooPy $s_{BV} = 1$. We use the same time of B-band maximum light for both SNooPy and BayeSN and fit only the NIR light-curve data to obtain photometric distance estimates.

As demonstrated in Figure 17, these distances are consistent across the redshift range of our sample, with the average difference between BayeSN and SNooPy distances changing by just 2 mmag from the low-z to high-z samples. As SNooPy has rarely been used at high redshift, this consistency between the two models gives us confidence that the raw distances that we measure with SNooPy are robust.

5.2.2. Optical Distances from SALT3 and SNooPy

In Table 4, we explore the differences between several methods of measuring NIR, optical, and optical+NIR distances. We compare the baseline NIR-only distances to optical +NIR distances with both the baseline $R_V = 1.5$ and an MW-like $R_V = 3.1$. We also compare to optical distances from SALT3, and finally, we use an approach where optical+NIR data are first used to determine s_{BV} and then s_{BV} is fixed to that value in an NIR-only fit that measures the distance. This essentially allows the NIR distances to include the anticipated s_{BV}−luminosity relation.

We find Hubble residual differences of ∼1%−2% between our baseline NIR method and methods using optical data and the default SNooPy value of $R_V = 1.5$ (Folatelli et al. 2010). With $R_V = 3.1$, the difference in distances is much larger, at 0.065 mag between low and high redshift, though we note that using this value of R_V increases the Hubble residual scatter by 28%. In an NIR-only analysis, however, using $R_V = 3.1$ changes the distances by just ∼0.02−0.04 mag owing to the lower sensitivity of the NIR to the value of R_V. Because we allow negative extinction in this analysis and because SNooPy does not model the intrinsic correlation between color and luminosity, the R_V parameter is more analogous to the nuisance parameter β in the Tripp relation than to a physical dust law.

The difference between our baseline distances and SALT3 distances is just 0.005 ± 0.038 mag. Although this difference in distance is small, the bias corrections shown in Figure 7 are ∼0.05 mag smaller in the NIR-only distances, increasing the potential discrepancy between SALT3 and the baseline NIR measurement. However, given the large uncertainties on the distance in measurement, a SALT3-based (or SALT2-based) analysis would still yield a consistent measurement of w.

Finally, the procedure of adjusting the NIR distances by a value of s_{BV} measured in the optical results in a statistically insignificant -0.016 ± 0.027 mag change. The lack of a small s_{BV} correction in our baseline analysis therefore does not appear to have a significant impact on the resulting cosmological parameter estimation. We also explore altering the semiarbitrary s_{BV} cuts in our baseline distance measurements, particularly given that the s_{BV} values tend to cluster near ∼1.18, perhaps due to a limited high-s_{BV} training sample in SNooPy. Fortunately, we find that our analysis is relatively insensitive to the minimum and maximum s_{BV}; both a "loose" cut of $0.6 < s_{BV} < 1.3$ and a "tight" cut of $0.8 < s_{BV} < 1.15$ change the average Hubble residual by just 7 mmag when comparing SNe at $z < 0.1$ to those at $z > 0.1$. The mass step measurement is changed by less than 0.01 mag.

In Figure 18, we examine the dispersion of Hubble residuals for different methods that use optical data. We find that the

---

[36] This value is from the analysis variant in which Scolnic et al. (2018) do not apply bias corrections to the SN shape and color parameters and is the analysis version that is most comparable to our method here.

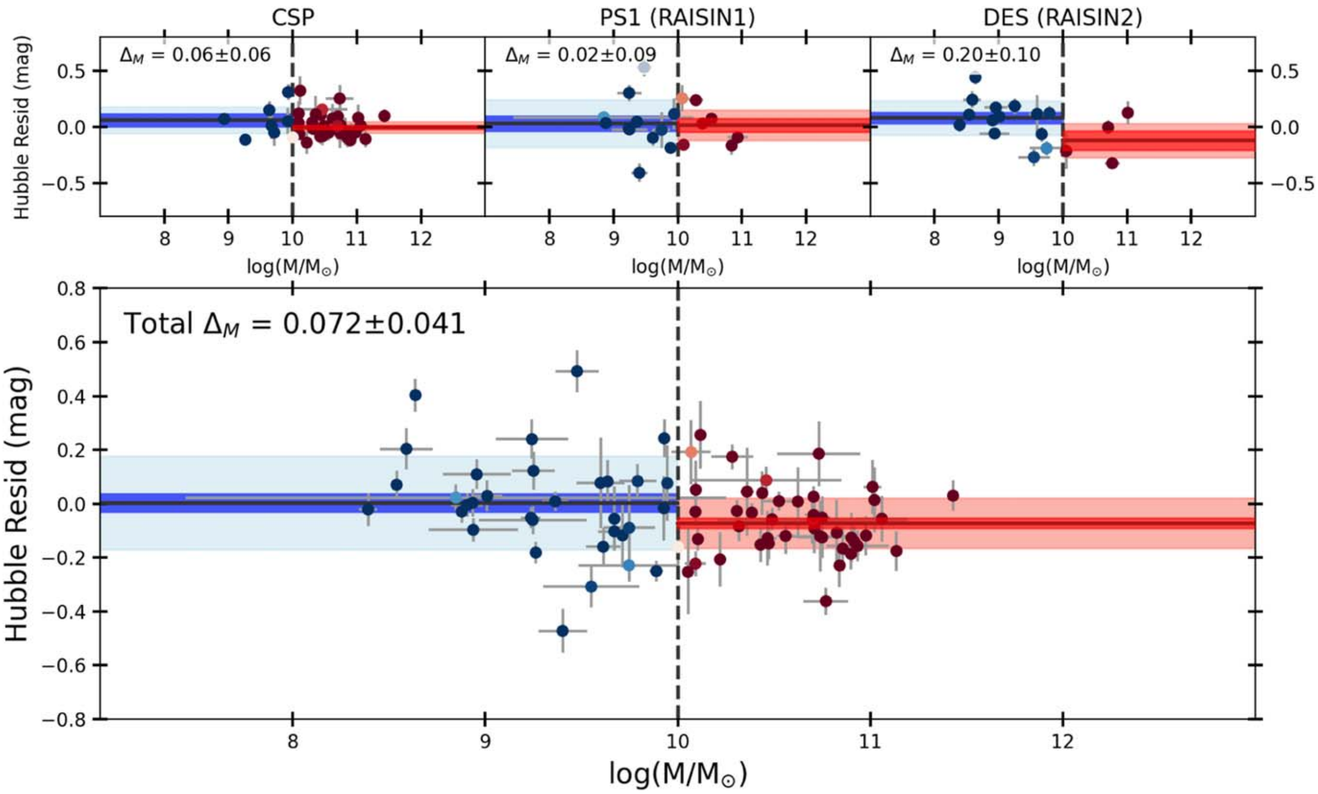

Figure 16. Maximum likelihood, NIR mass step measurements with CSP (top left), RAISIN1 (top middle), RAISIN2 (top right), and all data combined (bottom). Dark shading indicates the uncertainty on the mean for high-mass (red) and low-mass (blue) hosts, while light shading indicates the dispersion of each population. The shading of the points indicates the probability that an SN is in a low-mass host (blue) or high-mass host (red). In this figure (unlike in Figure 10), we correct individual distances for s_{BV} to derive a measurement that is directly comparable to optical analyses. We also simultaneously fit for three z-dependent distance bins to remove the effect of cosmological parameter values on the mass step size.

Hubble residual dispersion is lowest when using the optical +NIR with $R_V = 1.5$ (0.140 mag) or the SALT3 model (0.130 mag). SALT3 appears to standardize SNe Ia more precisely than SNooPy at high redshift, while SNooPy distances are more precise than SALT3 distances for the CSP data on which SNooPy was trained. The SALT3 results are nearly the same as those from SALT2, which was used for most previous optical-only analyses.

If an optical versus NIR difference becomes statistically significant in future work, it could point to unrecognized systematic uncertainties in analyses with optical data, NIR data, or both. In optical analyses, the G10 scatter model is a source of significant uncertainty in correcting for distance-dependent biases (Scolnic et al. 2018; Brout et al. 2019b), and proposed alternative scatter models could shift w by 4% (Brout & Scolnic 2021). In the NIR, differences in stretch−luminosity correlations between Burns et al. (2014) and Burns et al. (2018), for example, may point to systematic uncertainties in SNooPy NIR standardizations. These results show that NIR observations constitute an extremely useful consistency check on optical analyses.

5.3. The Late-time NIR Model

Our Hubble diagram compares SNe observed near maximum light in the low-z CSP sample to SNe observed only at later phases in the higher-z RAISIN sample; the initial NIR epoch in RAISIN occurred at +9 rest-frame days on average. This could introduce systematic uncertainty if the SN standardization model is not as accurate at late times as it is near maximum light, where most previous NIR data exist. Although we account for this systematic uncertainty by using two SN Ia standardization models, both use much of the same training data.

To investigate potential biases due to the phase at which each SN was observed in the NIR, we investigated whether there is a trend in Hubble residuals as a function of the median phase at which each SN was observed. By comparing the Hubble residuals of SNe observed at a median phase of $<+15$ days to those observed at a median phase of $>+15$ days (+15 days is approximately the sample median), we detected a "step" in the NIR Hubble residuals at 3σ significance. This step appears to show that RAISIN SNe Ia observed at a phase of $>+15$ days are fainter by 0.164 ± 0.051 mag than RAISIN SNe Ia observed at a median phase of $<+15$ days. Though this trend is potentially concerning, we note that the difference in stretch between the early- and late-observed samples is 0.12, which could explain ∼0.05 mag of the ∼0.16 mag difference (Figure 15). This selection bias could be caused by the fact that low-stretch SNe are intrinsically fainter, so it may have been harder to classify them and subsequently trigger HST observations prior to maximum light.

To inspect potential biases in the SNooPy model as a function of phase, in Figure 19 we show the SNooPy Y-band template alongside the CSP and RAISIN observations after the observed data have been converted to the rest frame. Both the high- and low-z data agree relatively well with the SNooPy model, albeit with slight offsets at $+10$ days $<$ phase $<$ $+20$ days of ∼0.05 mag. These offsets suggest that the late-phase NIR SNooPy model should be adjusted as more data

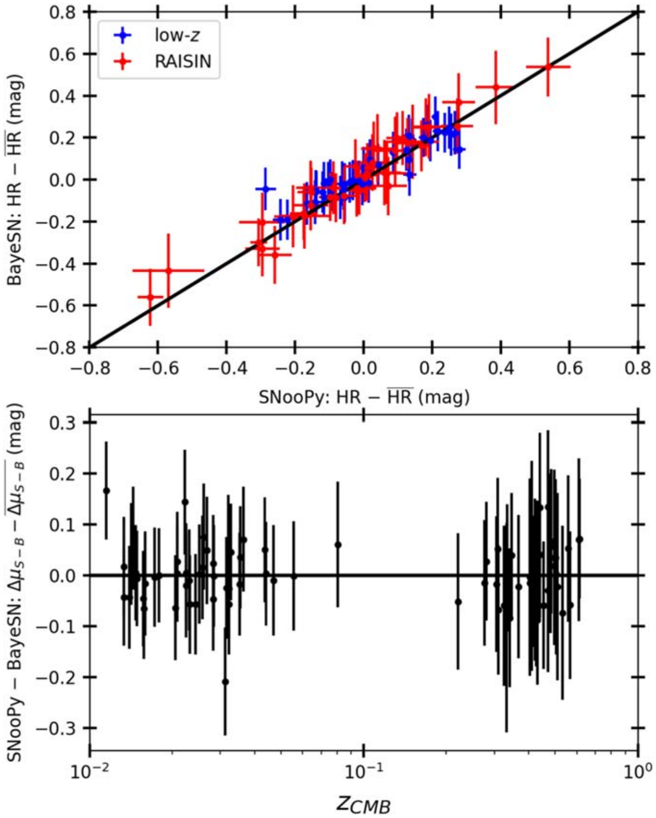

Figure 17. Top: SNooPy vs. BayeSN Hubble residuals for the low-z (blue) and RAISIN (red) samples. Bottom: SNoopy distance moduli minus BayeSN distance moduli as a function of redshift with an average redshift-independent offset removed (cosmological parameter measurements are not affected by a global offset). The average value of the SNooPy distance modulus minus the BayeSN distance modulus changes by only 2 mmag between the low-z and RAISIN samples.

Table 4
Optical+NIR Distance Comparisons

	$\Delta\mu$ (mag)
Optical+NIR ($R_V = 1.5$)	0.011 ± 0.030
Optical+NIR ($R_V = 3.1$)	−0.065 ± 0.032
Optical with SALT3	0.005 ± 0.038
Optical+NIR s_{BV}, NIR dist.	−0.016 ± 0.027

Note. For optical+NIR analysis methods without bias corrections, the difference between low- and high-z distances relative to the baseline NIR-only method.

become available but would only shift the mean high-z distance measured here by approximately 0.02 mag. The variance of the NIR data also appears to increase slightly near the phase at which most of the later RAISIN observations occur, while observations near maximum light have the lowest scatter. The slightly higher scatter of the RAISIN magnitudes compared to CSP might also be an indication of K-correction uncertainties in the high-z distances. We observe similar trends when comparing the J-band SNooPy model to our data.

The apparent dependence of Hubble residual on the phase at which an SN was observed could also be due to subtle errors in the relationship between SN luminosity and s_{BV} or the fact that the NIR SN color−luminosity dependence differs significantly from the relation that would be expected from dust extinction alone. Although retraining the SNooPy model is beyond the scope of this work and will likely require significant additional rest-frame NIR data to be robustly redetermined, additional low-z data and model retraining are important ways in which future NIR analyses could be improved.

6. Discussion

Although this study reaffirms the existence of cosmic acceleration and establishes the value of NIR SN Ia data for cosmological measurements, much of the value of this data set will be in preparing for NIR SN Ia samples from the Roman Space Telescope. Although the SN survey strategy is not yet finalized, Roman will observe in the rest-frame NIR to $z \approx 0.7$, the regime in which cosmological parameter constraints from SNe Ia will likely be more precise than volume-limited baryon acoustic oscillations (Weinberg et al. 2013). Measuring the most precise cosmological constraints from these data will be the path to obtaining the best possible constraints on cosmological parameters.

With Roman on the horizon, the systematic error budget presented here suggests a path forward for improved NIR cosmological constraints. Here is what we need:

1. Larger photometric NIR samples with coverage near maximum light across multiple photometric systems to improve calibration systematics.
2. Larger photometric and spectroscopic NIR samples to improve training of models, and optical-to-NIR measurements of the SN Ia dispersion to constrain any redshift dependence of the value of R_V.
3. Optical-to-NIR SN Ia SED models and standardization methods that separate SN Ia intrinsic dispersion from the effects of host galaxy dust as a function of wavelength and improve the modeling of high-stretch (slowly declining) SNe.
4. Improved constraints on the host galaxy mass step and other host galaxy dependences as a function of wavelength to break degeneracies with dust properties.
5. An untargeted NIR low-z sample with well-understood selection effects.

These improvements would improve the accuracy of the cosmological measurement presented here even without obtaining additional high-z data. A public release of CSP-II NIR spectra and photometry will address several of these key points (Hsiao et al. 2019; Phillips et al. 2019). As we enter the Roman era, new data will also reduce bias correction systematics by constraining the distribution of SN shape and color as a function of redshift. We elaborate on a number of these potential improvements below.

6.1. NIR Dispersion Model

The NIR dispersion model measured both in this work and in the BayeSN SED model shows that NIR distances offer significant independent leverage to constrain distance measurements compared to those obtained only with optical data. Further, NIR data, in combination with optical, provide additional leverage to improve constraints on both R_V and A_V, as demonstrated in recent analyses that use NIR data to break the degeneracy between host galaxy dust and intrinsic SN physics (Thorp et al. 2021; Mandel et al. 2022).

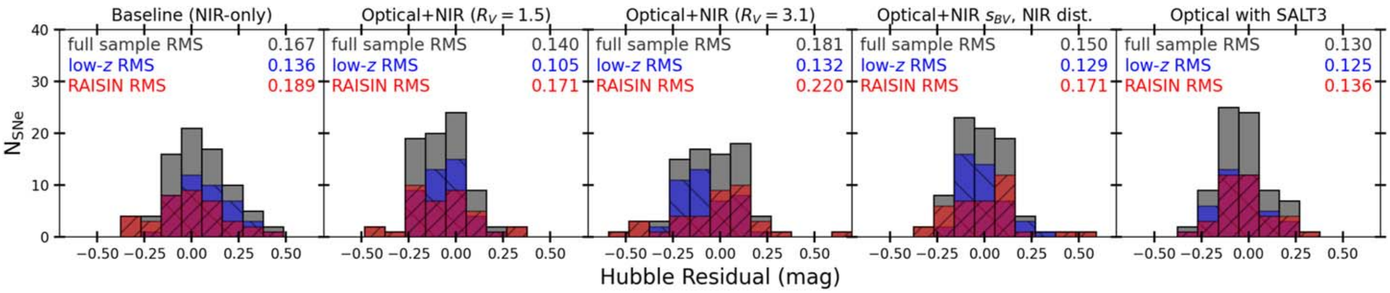

Figure 18. Hubble residual scatter for different analysis variants. From left to right, we show our baseline NIR-only Hubble residuals, optical+NIR SNooPy distances with $R_V = 1.52$ (Folatelli et al. 2010), optical+NIR SNooPy Hubble residuals with $R_V = 3.1$, NIR SNooPy Hubble residuals after applying the s_{BV} parameters measured from optical+NIR data, and optical SALT3 Hubble residuals. The SALT3 panel removes two CSP SNe with colors that are too red ($c > 0.3$) to pass standard SALT cosmology cuts; with these SNe included, scatter increases negligibly to 0.132 mag in the CSP sample.

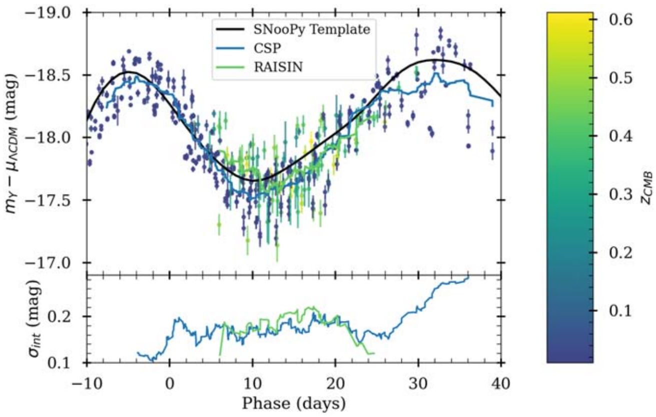

Figure 19. The SNooPy model (black) compared to CSP (blue) and RAISIN (red) measurements after using the SNooPy *K*-corrections and the cosmological distance to convert the observations to rest-frame absolute magnitude. Solid lines in the top panel show the rolling means of the CSP and RAISIN absolute magnitudes, and the rolling standard deviation, with the average peculiar velocity error and photometric noise subtracted in quadrature, is shown in the bottom panel. NIR SN Ia observations appear to have the lowest rms near maximum light and slightly higher rms from ∼10 to 25 days.

In this study, we see that, even without shape and color corrections, just three epochs of NIR data at ∼10−20 days after maximum light are sufficient to constrain dark energy properties. It is possible that even fewer epochs or filters would still yield competitive cosmological constraints, though additional epochs and filters give the valuable ability to avoid data outliers and to constrain dust properties. Much of the systematic uncertainty in this analysis stems from the fact that these SNe were selected for spectroscopic follow-up in the optical. In large, untargeted NIR samples like those from Roman, this source of systematic uncertainty will vanish.

6.2. Building a New, Well-calibrated NIR SED Model

SN Ia analyses and standardization models in the NIR are currently limited by the sample sizes of well-calibrated data sets, both photometric and spectroscopic, which introduce substantial calibration systematics and uncertainties in the precision of the standardization model training itself. New, well-calibrated NIR samples from CSP-II, SIRAH, VISTA, UKIRT (Konchady et al. 2022), and eventually Roman will be needed for improved model training. Simultaneous NIR spectroscopy will also be important for a better understanding of *K*-corrections. The SIRAH sample in particular, with extremely well-calibrated photometry and grism spectroscopy tied to ground-based NIR observations, will be a powerful link between precise NIR cosmological analyses from space and the ground.

This analysis shows that the NIR+optical measurement of *w* has similar precision to the optical measurement alone. Although we find that systematic uncertainties on *w* are lowest when we use NIR data in combination with optical, there is no improvement in the precision of cosmological parameter measurements when adding NIR data in this analysis. This is likely because our light-curve fitting approaches are not yet optimally weighting the SN data at different wavelengths, a problem that previous studies have found can be addressed with improved uncertainty treatments in SN standardization models (Mandel et al. 2011, 2022).

6.3. The Mass Step

The underlying cause of the host galaxy mass step is a subject of debate, with numerous explorations of alternative global host galaxy dependencies (Hayden et al. 2013; Pan et al. 2014) or relationships between Hubble residuals and local host galaxy properties near the SN location (Rigault et al. 2013; Jones et al. 2015a; Rigault et al. 2015; Jones et al. 2018b; Kim et al. 2018; Rigault et al. 2020; Roman et al. 2018; Kelsey et al. 2021). The degeneracy between physical effects, potential data reduction artifacts (Solak et al. 2021), and dust has made measuring the wavelength dependence of the host galaxy mass step, as well as other host galaxy dependencies, extremely important for next-generation cosmological measurements. Measurement of whether a step-like dependence of NIR Hubble residuals on global or local galaxy color (e.g., Roman et al. 2018; Jones et al. 2018b; Kelsey et al. 2021) would be particularly interesting to understand the effects of dust or progenitor ages on SN distance measurements. Previous measurements of the mass step in the NIR have been limited by sparse data (Ponder et al. 2021) and the need to include optical data with the NIR observations to constrain the best-fit parameters such as s_{BV} and A_V (Uddin et al. 2020). Flexible simulation-based approaches (e.g., Pierel et al. 2021) will be necessary to fully understand the impact of different SN–host relationships on cosmological parameter measurements.

Although the galaxy-targeted nature of the CSP sample has made measuring the mass step in this work difficult (nearly all CSP galaxies are in the "high-mass" regime), we do find evidence suggesting that the mass step in the NIR is about the size of the mass step in the optical. We note that our results are not in tension with other recent NIR mass step results, including those of Johansson et al. (2021), who saw that the mass step was insignificant in the JH bands and less significant ($\sim 2\sigma$) in the Y band. Our distances primarily probe the rest-frame Y band, albeit with some i- and J-band overlap, where Johansson et al. (2021) find a mass step of approximately 0.07 ± 0.03 mag. However, our results do not favor the conclusion of Brout & Scolnic (2021) that the mass step is caused by variations in dust properties, as the effect of variation in R_V should decrease by a factor of ∼3 between, e.g., rest-frame V and rest-frame Y. Further study of the origin of the mass step is clearly needed, and larger infrared samples may prove useful.

Future measurements of this and other host galaxy dependencies as a function of wavelength may be necessary to separate intrinsic color, dust, other SN Ia physics, or even multiple SN Ia progenitor models. For example, when measuring the mass step, we did not fit for individual R_V values, as was done in Johansson et al. (2021), or simultaneously constrain the population distribution of R_V values, as was done in Thorp et al. (2021); these methods can help to disentangle the role of dust in the mass step's size. Although SNe Ia are used as an empirical tool for measuring distance, understanding the objects and their connection to stellar populations is also valuable in itself. The evolution of stellar populations and of SN Ia progenitors across the long span of cosmic time that Roman will provide gives an opportunity to understand the nature of SN progenitors and their environments and to use them for more precise cosmological measurements.

7. Conclusions

We present photometric measurements, a Hubble diagram, and NIR-only cosmological constraints from the RAISIN survey. SN candidates were observed in cycles 20 and 23 by HST and combined with low-z, NIR-observed SNe from CSP to yield an NIR Hubble diagram and a better understanding of cosmological parameter measurements in the NIR. From CSP data we build a new, optical-to-NIR dispersion model for SNe Ia to predict distance-dependent biases and measure the independence of SN Ia distances in the optical and NIR. We find that NIR-derived distances are well correlated with distances derived from optical data but offer some independent information. The dispersion of our NIR-only distances is 0.18 mag, ∼25% larger than the Pantheon sample at 0.141 mag but not standardized using shape or color information. When measuring the host galaxy mass step after applying shape corrections to our distances, in order to match the procedures used in optical analyses, we measure an NIR mass step of 0.072 ± 0.041 mag at a step location of 10 dex and 0.123 ± 0.034 mag at a step location of 10.44 dex.

In combination with CMB constraints from Planck Collaboration et al. (2020) and assuming a flat wCDM model, we measure $1 + w = -0.17 \pm 0.12$ (stat+sys), consistent with the ΛCDM expectation of $w = -1$. This NIR measurement of w may embed unknown systematic uncertainties that will become apparent when future, larger NIR samples are analyzed. The dominant systematic uncertainties in this analysis stem from bias corrections, which will be improved by future SN standardization models that extend to the NIR; building these models will be facilitated by larger NIR sample sizes on the way from CSP-II, SIRAH, VISTA, and UKIRT. We find that combined cosmological parameter measurements from optical +NIR data appear to have lower systematic uncertainties than when using optical data alone. We also see shifts in w of up to 0.1 among optical, optical+NIR, and NIR data alone, pointing to the possibility of inconsistency in the optical versus NIR SN standardization models.

We also measure $H_0 = 75.9 \pm 2.2\ \mathrm{km\ s^{-1}\ Mpc^{-1}}$ from a local distance ladder approach tied to eight NIR-observed SNe Ia with Cepheid or TRGB distances versus $H_0 = 71.2 \pm 3.8\ \mathrm{km\ s^{-1}\ Mpc^{-1}}$ using a so-called "inverse distance ladder" approach anchored to CMB measurements of the angular size of the sound horizon. Future NIR measurements can help to constrain whether the present dark energy density or systematic uncertainties due to SN Ia dust could play any role in the H_0 tension.

Finally, these data will help us to better understand the behavior and standardization of SNe Ia in the NIR and assist the community in preparing for data from the Roman Space Telescope. Improved dispersion models will help improve distances by using an optical+NIR combination, and wavelength-dependent measurements of the dependence of SN Ia distance measurements on host galaxy properties will break the degeneracies with dust properties. When combined with future data sets from SIRAH and improved SN Ia standardization models that can be trained with this data set, we hope the data published here will have legacy value for the SN Ia community in the Roman Space Telescope era.[37]

We would like to acknowledge that much of the data and analysis in this manuscript were made possible through the work of our friend and colleague Dr. Andrew S. Friedman, who passed away during the final stages of this project. We would also like to thank G. Narayan and N. Drakos for useful discussions and their assistance with HST photometry and K-corrections. We would like to thank R. Kessler for implementing the latest SNooPy model in SNANA and C. Rojas-Bravo for assistance with the spectra. We would also like to thank the anonymous referee for many helpful suggestions.

Support for this work was provided by a Gordon and Betty Moore Foundation postdoctoral fellowship to D.O.J. at the University of California, Santa Cruz, and by NASA through the NASA Hubble Fellowship grant HF2-51462.001 awarded by the Space Telescope Science Institute, which is operated by the Association of Universities for Research in Astronomy, Inc., for NASA, under contract NAS5-26555. The Cambridge University team acknowledges support from the European Research Council under the European Union's Horizon 2020 research and innovation program (ERC grant agreement No. 101002652); the ASTROSTAT-II collaboration, enabled by the Horizon 2020, EU grant agreement No. 873089; and the Cambridge Centre for Doctoral Training in Data-Intensive Science funded by the UK Science and Technology Facilities Council (STFC). L.G. acknowledges financial support from the Spanish Ministerio de Ciencia e Innovación (MCIN), the Agencia Estatal de Investigación (AEI) 10.13039/501100011033, and the European Social Fund (ESF) "Investing in your future" under the 2019 Ramón y Cajal program RYC2019-027683-I and the PID2020-115253GA-I00 HOSTFLOWS project, from Centro Superior de Investigaciones Científicas (CSIC) under the PIE project 20215AT016, and the program Unidad de Excelencia Mara de Maeztu CEX2020-001058-M. M. R.S. is supported by the NSF Graduate Research Fellowship

---

[37] The data used in this analysis are published at https://doi.org/10.5281/zenodo.6349657.

Program under grant 1842400. The UCSC team is supported in part by NASA grants 14-WPS14-0048, NNG16PJ34C, and NNG17PX03C; NSF grants AST-1518052 and AST-1815935; NASA through grant No. AR-14296 from the Space Telescope Science Institute, which is operated by AURA, Inc., under NASA contract NAS 5-26555; the Gordon and Betty Moore Foundation; the Heising-Simons Foundation; and fellowships from the Alfred P. Sloan Foundation and the David and Lucile Packard Foundation to R.J.F. Based on observations with the NASA/ESA Hubble Space Telescope obtained from the Data Archive at the Space Telescope Science Institute, which is operated by the Association of Universities for Research in Astronomy, Inc., under NASA contract NAS5-26555. Support for program Nos. 13046 and 14216 was provided through grants from the STScI under NASA contract NAS5-26555. The Carnegie Supernova Project has been supported by the National Science Foundation under grants AST0306969, AST0607438, AST1008343, AST1613426, AST1613455, and AST1613472. L.K. thanks the UKRI Future Leaders Fellowship for support through the grant MR/T01881X/1. This research has made use of the NASA/IPAC Extragalactic Database (NED), which is funded by the National Aeronautics and Space Administration and operated by the California Institute of Technology.

This paper includes data gathered with the 6.5 m Magellan Telescopes located at Las Campanas Observatory, Chile. Some of the observations reported here were also obtained at the MMT Observatory, a joint facility of the University of Arizona and the Smithsonian Institution, and the W. M. Keck Observatory, which is operated as a scientific partnership among the California Institute of Technology, the University of California, and the National Aeronautics and Space Administration. The Observatory was made possible by the generous financial support of the W. M. Keck Foundation. The authors also wish to recognize and acknowledge the very significant cultural role and reverence that the summit of Maunakea has always had within the indigenous Hawaiian community. We are most fortunate to have the opportunity to conduct observations from this mountain. This paper also uses observations obtained at the international Gemini Observatory, a program of NSF's NOIRLab, which is managed by the Association of Universities for Research in Astronomy (AURA) under a cooperative agreement with the National Science Foundation on behalf of the Gemini Observatory partnership: the National Science Foundation (United States), National Research Council (Canada), Agencia Nacional de Investigacin y Desarrollo (Chile), Ministerio de Ciencia, Tecnologa e Innovacin (Argentina), Ministrio da Cincia, Tecnologia, Inovaes e Comunicaes (Brazil), and Korea Astronomy and Space Science Institute (Republic of Korea). Finally, we include data acquired at the Anglo-Australian Telescope. We acknowledge the traditional owners of the land on which the AAT stands, the Gamilaroi people, and pay our respects to elders past and present.

Software: PythonPhot (Jones et al. 2015b), hstphot (https://github.com/srodney/hstphot), TinyTim (Krist et al. 2011), HOTPANTS (Becker 2015), ZOGY (Zackay et al. 2016), corner (Foreman-Mackey 2016), SNANA (Kessler et al. 2010), LePHARE (Arnouts & Ilbert 2011), SNooPy (Burns et al. 2011, 2014), RVSAO (Kurtz & Mink 1998), Marz (Hinton et al. 2016).

Appendix A
Photometric Measurements from HST

In this appendix, we describe the photometric measurement of RAISIN SNe from HST. The photometric measurements themselves are given in Appendix B.

First, we used AstroDrizzle to combine RAISIN FLT images downloaded from the Mikulski Archive for Space Telescopes (MAST) and created geometric distortion-corrected images for each epoch of each SN. For a given SN, each epoch of observations is drizzled; then the output, drizzled images are aligned to a reference image via `tweakreg` so that SN coordinates are consistent in all epochs; and then the data from each epoch are redrizzled. Finally, we subtract the drizzled template image from each image containing the SN. We make use of `sndrizpipe`,[38] a pipeline for HST drizzling and image subtraction originally written for the CANDELS and CLASH HST Multi-Cycle Treasury programs (Grogin et al. 2011; Postman et al. 2012) that has continued being actively developed in the past few years. Images were drizzled to $0\farcs11$ pixel^{-1}, slightly smaller than the native pixel scale of WFC3, to improve the resolution of the HST PSF (we found minimal differences between $0\farcs09$ and $0\farcs13$ pixel^{-1} choices). The photometric zero-points that we use are derived from the latest HST calibrations of Bohlin et al. (2020).

SN positions from discovery data or optical imaging are known to approximately $1''$ precision or better and are given in Table 5. We use centroiding algorithms from the `hstphot`[39] and `PythonPhot` (Jones et al. 2015b) packages to refine those positions. The best centroid was given by the weighted average of coordinates measured from F125W images for RAISIN1 and F160W images for RAISIN2. Because SNe Ia are fainter in redder bands and host galaxies are often brighter, coordinates from F125W images tend to be more reliable when available.

Using the measured SN coordinates, we performed aperture photometry with a fixed $0\farcs4$ radius using the zero-points and aperture corrections determined from standard star observations.[40] We found that, due to the undersampled and somewhat variable HST PSF, aperture photometry was more reliable than PSF photometry for these images. There are few stars in a typical RAISIN frame from which to determine the PSF on an epoch-by-epoch basis, and, likely due to the breathing of HST and the undersampled WFC3 PSF, we found that the PSF was too variable for a PSF model based on archival data to be sufficient. By performing artificial star tests, we found that we were unable to perform PSF photometry without introducing millimagnitude-level biases.

As the drizzling process produces pixels with correlated noise, uncertainties were estimated by planting 1000 fake stars per epoch at random locations. Fake stars were generated using a P330E PSF model (again created using `hstphot`), and each fake star had a magnitude equal to the measured SN mag in a given epoch. The dispersion in these fake star magnitudes was added in quadrature to the Poisson noise from the SN to give the total uncertainty due to sky background variation, correlated pixels, and Poisson noise. Given that our final pixel scale is near the native pixel size of WFC3-IR, the noise in the recovered stars is likely dominated by Poisson noise of the sky background.

---

[38] https://github.com/srodney/sndrizpipe

[39] https://github.com/srodney/hstphot

[40] https://www.stsci.edu/hst/instrumentation/wfc3/data-analysis/photometric-calibration/ir-photometric-calibration

Table 5
RAISIN Coordinates, Redshifts, and Discovery Dates

ID	α	δ	$z_{\rm Helio}$	$z_{\rm CMB}$	$z_{\rm source}$[a]	MJD$_{\rm disc}$
PS1-480464	09:59:12.147	03:13:17.555	0.220	0.221	host	55243
PS1-450082	23:33:25.446	00:18:37.609	0.250	0.249	SN	56233
PS1-540087	22:21:30.369	00:07:46.110	0.275	0.275	host	56505
PS1-520188	14:22:05.831	52:32:40.679	0.280	0.280	host	56469
DES16E2cxw	00:40:42.701	−43:55:18.948	0.293	0.293	host	57686
PS1-440005	03:31:57.424	−28:53:00.481	0.306	0.306	host	56206
PS1-520062	16:17:48.345	54:37:59.502	0.308	0.308	SN	56442
PS1-500100	08:46:33.237	45:21:21.978	0.310	0.311	host	56383
PS1-500301	14:22:11.455	52:37:54.908	0.325	0.325	host	56394
PS1-470041	08:45:21.034	44:45:17.194	0.331	0.332	host	56290
PS1-480794	09:58:10.055	01:21:50.792	0.334	0.334	host	56332
PS1-490521	09:55:27.619	01:34:30.925	0.340	0.341	SN	56358
PS1-470110	03:28:16.989	−28:37:23.988	0.346	0.346	host	56299
DES16E2clk	00:36:48.876	−44:08:23.460	0.367	0.367	SN	57680
DES16C2cva	03:34:44.035	−29:19:02.028	0.403	0.403	host	57686
DES15X2kvt	02:21:46.262	−05:38:23.640	0.404	0.404	SN	57298
PS1-450339	02:25:09.004	−03:21:12.182	0.410	0.410	host	56234
DES15E2nlz	00:35:51.350	−44:40:36.444	0.410	0.410	SN	57356
PS1-530251	22:18:32.238	01:06:53.316	0.413	0.412	host	56477
DES15C1nhv	03:39:00.948	−27:50:35.520	0.421	0.421	host	57355
PS1-550202	23:27:11.964	−00:46:59.074	0.422	0.421	host	56558
PS1-490037	09:59:49.727	00:48:59.738	0.422	0.423	host	56354
DES16E2cqq	00:39:50.076	−43:33:53.388	0.426	0.426	host	57682
PS1-440236	02:28:24.442	−04:25:28.243	0.430	0.429	host	56197
PS1-470240	08:42:53.508	45:54:04.910	0.430	0.431	SN	56302
DES16X1cpf	02:16:49.512	−04:13:06.096	0.436	0.436	host	57681
DES15E2mhy	00:41:17.134	−43:53:10.104	0.439	0.439	host	57329
PS1-560027	02:23:24.170	−03:05:02.026	0.440	0.439	SN	56167
DES16E1dcx	00:35:52.440	−43:21:29.232	0.453	0.453	host	57694
DES15X2nkz	02:22:13.210	−05:52:18.228	0.469	0.469	host	57356
DES16S1bno	02:50:03.823	−00:01:17.724	0.470	0.470	SN	57653
PS1-540118	23:27:17.446	−00:02:53.063	0.477	0.477	host	56508
PS1-560054	23:33:10.992	−00:20:11.692	0.482	0.480	host	56562
DES16S2afz	02:46:24.329	−01:13:31.044	0.483	0.483	host	57626
DES16E2rd	00:32:21.334	−43:50:46.032	0.494	0.494	host	57629
DES16X3zd	02:26:56.465	−04:25:09.804	0.495	0.495	host	57325
PS1-510457	12:25:33.373	48:08:11.868	0.502	0.503	host	56420
DES16S1agd	02:52:20.062	−00:54:40.284	0.504	0.504	host	57633
DES15C3odz	03:27:55.027	−28:33:52.092	0.508	0.508	host	57378
PS1-520107	12:16:38.631	47:48:57.881	0.519	0.520	SN	56444
DES16C1cim	03:39:30.362	−26:38:57.048	0.531	0.531	host	57667
DES16C3cmy	03:27:13.440	−27:29:20.724	0.556	0.556	host	57680
DES15E2uc	00:37:53.419	−43:18:51.552	0.566	0.566	host	57252
DES15X2mey	02:20:30.785	−06:26:47.472	0.608	0.608	host	57327
DES16X3cry	02:24:10.548	−03:49:51.996	0.612	0.612	host	57686

Notes. Coordinates, redshifts, and approximate discovery MJD (the first $S/N > 5$ detection) for RAISIN SNe.
[a] SN redshifts are accurate to $\sigma_z \simeq 0.01$, while host redshifts are accurate to better than $\sigma_z = 0.001$.

The expected bias in the photometry given the centroid uncertainties derived above is derived by Rest et al. (2014), their Appendix D. This requires an estimate of how much the magnitude changes when the coordinate is incorrect by 1 pixel. P330E images show that this is approximately 0.022 mag for a 0.″11 pixel scale, but typical centroid uncertainties are closer to ∼0.02 pixels. We corrected for these biases, but in practice we find that they are typically <1 mmag.

A.1. Host Galaxy Noise

SNe Ia on top of bright host galaxies can have biased measurements or underestimated errors. The additional noise introduced by a bright host galaxy tends to create significant subtraction residuals by increasing the effect of small PSF changes between the template and SN images. We occasionally see significant dipole-like subtraction artifacts.

To model this effect, we used `TinyTim` to create up to 25 fake stars near the *same host galaxy* as each SN. We require that the fake stars are at least 0.″7 from the SN position and from each other, which is >4 times the FWHM of the F160W PSF. We cannot measure the noise at the exact location of the SN, but we can gain a statistical sense of the noise as a function of host galaxy surface brightness from these fake stars.

The results of this test are shown in Figure 20. Small error bars give the uncertainty on the average magnitude in each

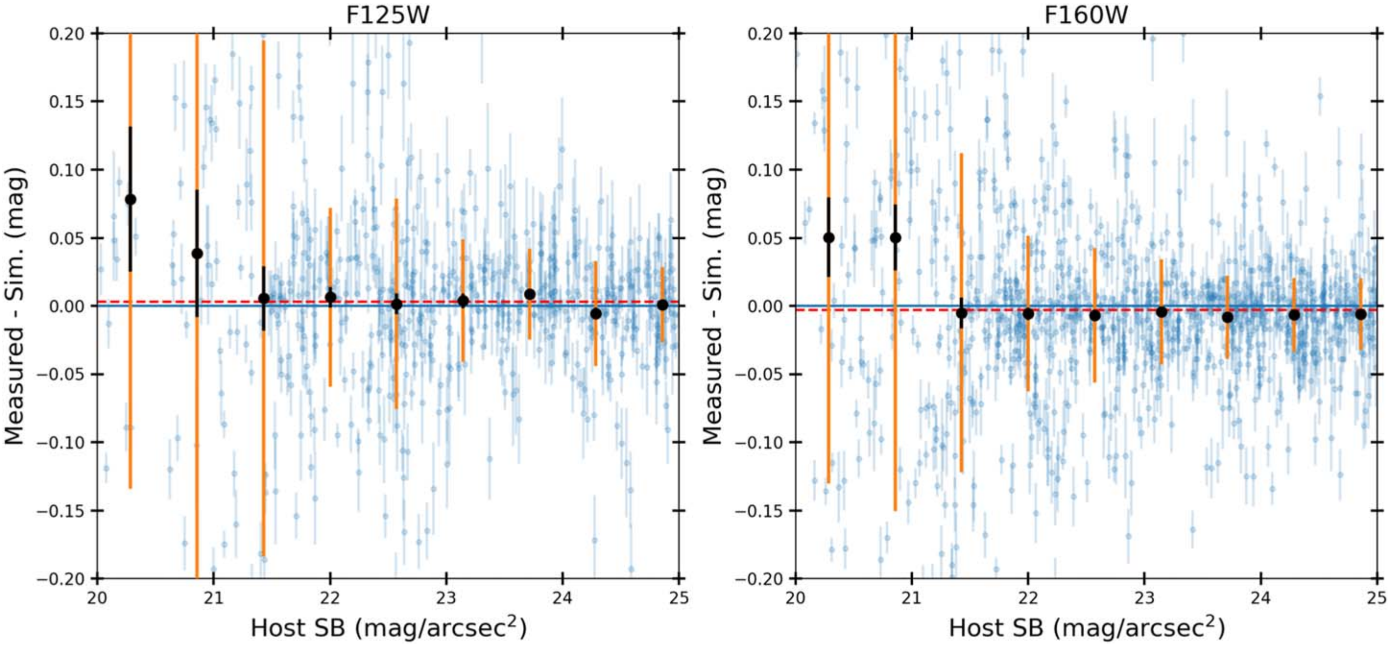

Figure 20. Dispersion of fake star magnitudes as a function of host galaxy surface brightness at the SN location for F125W (left) and F160W (right). Large error bars (orange) show the dispersion, while small error bars (green) show the error on the mean. We restrict to the sample of SNe with predicted host galaxy error less than 0.1 mag and verify with visual inspections that the subtracted images for these SNe appear reliable.

surface brightness bin, and large error bars give the dispersion of the fake magnitudes in each bin. To compute more realistic uncertainties, we then subtract the measured magnitude uncertainties in quadrature from the total magnitude dispersion of the fake stars. These quantities give the extra uncertainty that should be added in quadrature to each SN magnitude as a function of the brightness of the host galaxy underneath the SN. SNe with estimated host galaxy uncertainties of greater than 0.1 mag are removed from the sample; we chose this cut based on visual inspection, which shows that such SNe typically have subtraction artifacts likely due to misalignments or "breathing" of HST and are unlikely to provide reliable, unbiased photometry. Our team attempted applying convolutional subtraction algorithms to the data including HOTPANTS (Becker 2015) and ZOGY (Zackay et al. 2016) but did not achieve improved results for these bright hosts. Five SNe were removed from the final analysis based on excessive host galaxy noise.

A.2. Residual SN Flux in Template Imaging

The RAISIN programs took HST template imaging between 129 and 285 days after the estimated time of maximum light for subtracting from the HST images with SN light. To test that our time interval between SN images and template images was sufficient, we used early- and late-time observations of SN 2012fr, which has *YJ* imaging at ∼150 days after maximum light from Contreras et al. (2018). With these data, we can extrapolate to later times to estimate the residual flux of RAISIN SNe at the time the template was taken.

For all RAISIN SNe, we use this estimated template flux to correct the magnitudes of RAISIN SN observations for which the closest rest-frame band is *Y*. Due to the faster decline of SNe in the *J* band, the *J*-band correction is expected to be negligible. To account for variability in the typical decline rate of SNe at late times in the NIR, we created a version of our analysis in which we conservatively increase the predicted late-time template flux by 0.5 mag for each RAISIN SN and correct the photometry for this revised template flux prediction. We include this analysis variant in our systematic error budget (Section 3.7). Unfortunately, SN 2012fr is the only SN for which high-quality NIR data exist at ∼6 months after maximum light. We predict that 36 of 47 RAISIN SNe would have declined by <5 mag, giving expected magnitude corrections that are more than 1% for these SNe, with a maximum predicted correction of ∼3.7%. We note that this source of uncertainty could be eliminated by revisiting the sites of RAISIN SNe to obtain templates with zero flux from the SNe.

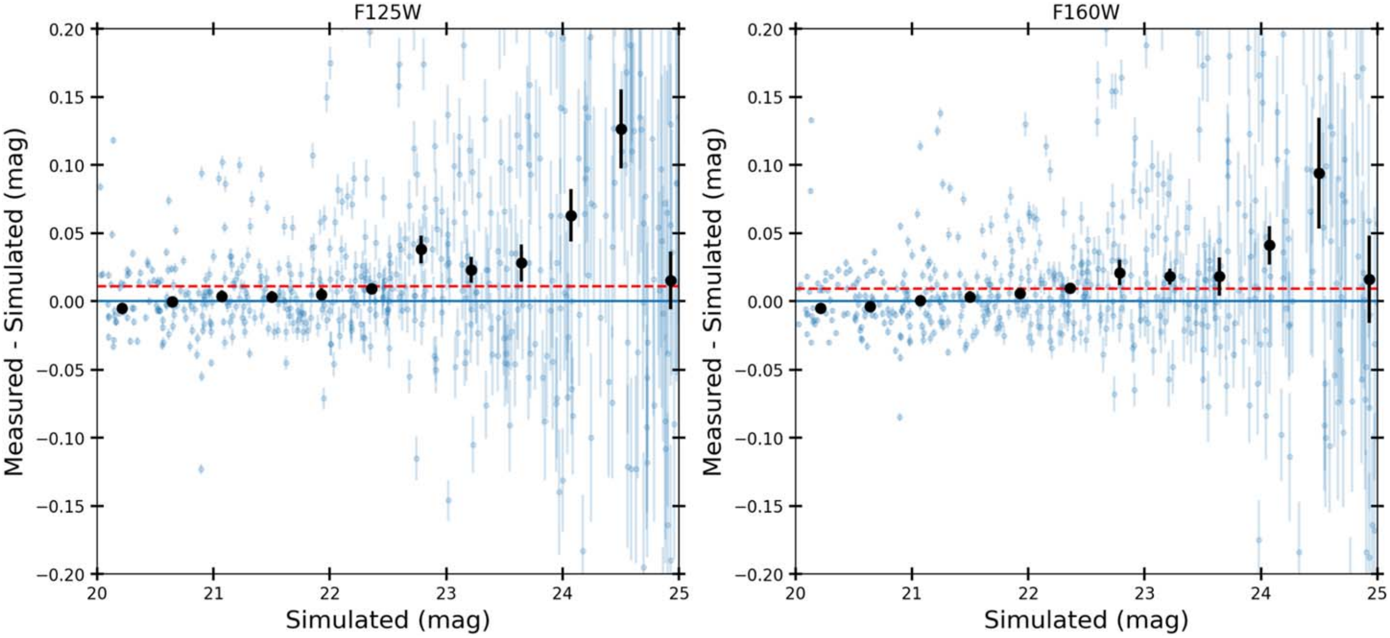

Figure 21. Measured fake star magnitudes minus simulated magnitudes as a function of mag for F125W (left) and F160W (right), with the median bias shown in red. We find just 1 mmag biases for sources brighter than 22 mag and ∼1% median biases overall, likely due to centroiding errors that are corrected in the real data thanks to multiple observational epochs.

A.3. End-to-end Fake Star Tests

Finally, to verify both our photometric measurement technique and our drizzling procedure, we used `TinyTim` to simulate fake, geometrically distorted stars in the FLT images. Then, we drizzled those images, subtracted them by a template, and measured output photometry on the sources detected in those images.

The results of these tests are shown in Figure 21. The median F125W and F160W biases are ⩽1 mmag for bright sources and ∼1% for all sources. However, because these tests use only a single epoch of data, this 1% bias may be due to inaccurate fake star centroids. In the real RAISIN data this bias is likely not present because we use multiple epochs to determine the precise PSF centroid.

Appendix B
Coordinates and Photometric Measurements of RAISIN SNe

Table 6 contains coordinates and HST photometry for the RAISIN sample. Optical light curves and spectra are provided in the online data release accompanying this paper at https://doi.org/10.5281/zenodo.6349657.

Table 6
RAISIN Photometry

SNID	MJD	filter	$m_{\rm SN}$ (mag)	$\sigma_{\rm SN}$ (mag)	$m_{\rm host}$ (mag)	$\sigma_{\rm host}$ (mag)	σ_c ($''$)	$\Delta_m^{\rm tmpl}$ (mag)	$\sigma_{\rm tmpl}$ (mag)
PS1-480464	56370	F160W	24.017 ± 0.080	0.073	23.304	0.033	0.006	0.000	0.000
PS1-480464	56370	F125W	22.437 ± 0.039	0.022	23.459	0.033	0.006	0.009	0.005
PS1-480464	56362	F160W	24.333 ± 0.114	0.109	23.304	0.033	0.006	0.000	0.000
PS1-480464	56362	F125W	22.726 ± 0.047	0.033	23.459	0.033	0.006	0.011	0.007
PS1-480464	56357	F160W	24.253 ± 0.122	0.117	23.304	0.035	0.006	0.000	0.000
PS1-480464	56357	F125W	22.921 ± 0.049	0.035	23.459	0.034	0.006	0.013	0.008
PS1-450082	56265	F125W	22.834 ± 0.238	0.030	20.889	0.236	0.003	0.014	0.008
PS1-450082	56265	F160W	24.573 ± 0.250	0.150	20.564	0.200	0.003	0.000	0.000
PS1-450082	56272	F125W	22.505 ± 0.237	0.022	20.889	0.236	0.003	0.010	0.006
PS1-450082	56278	F160W	24.469 ± 0.235	0.124	20.564	0.200	0.003	0.000	0.000
PS1-450082	56278	F125W	22.339 ± 0.237	0.022	20.889	0.236	0.003	0.009	0.005
PS1-450082	56272	F160W	24.606 ± 0.239	0.132	20.564	0.199	0.003	0.000	0.000
PS1-540087	56528	F125W	22.873 ± 0.078	0.043	21.797	0.065	0.002	0.011	0.006
PS1-540087	56536	F160W	24.962 ± 0.303	0.294	21.539	0.073	0.002	0.000	0.000
PS1-540087	56536	F125W	23.002 ± 0.078	0.045	21.797	0.064	0.002	0.012	0.007
PS1-540087	56528	F160W	23.748 ± 0.114	0.088	21.539	0.072	0.002	0.000	0.000
PS1-540087	56523	F160W	23.394 ± 0.103	0.072	21.539	0.074	0.002	0.000	0.000
PS1-540087	56523	F125W	22.657 ± 0.074	0.036	21.797	0.065	0.002	0.009	0.005
PS1- 520188	56488	F125W	22.534 ± 0.035	0.027	26.192	0.021	0.001	0.022	0.013
PS1-520188	56501	F160W	24.140 ± 0.075	0.071	26.190	0.024	0.001	0.000	0.000
PS1-520188	56501	F125W	22.573 ± 0.034	0.026	26.192	0.022	0.001	0.023	0.014
PS1-520188	56494	F160W	23.815 ± 0.048	0.041	26.190	0.025	0.001	0.000	0.000
PS1-520188	56494	F125W	22.689 ± 0.034	0.026	26.192	0.021	0.001	0.026	0.015
PS1-520188	56488	F160W	23.133 ± 0.037	0.028	26.190	0.024	0.001	0.000	0.000
DES16E2cxw	57715	F125W	22.771 ± 0.275	0.021	20.420	0.274	0.002	0.008	0.005
DES16E2cxw	57715	F160W	23.874 ± 0.200	0.072	20.203	0.187	0.002	0.000	0.000
DES16E2cxw	57723	F125W	22.691 ± 0.275	0.020	20.420	0.274	0.002	0.007	0.004
DES16E2cxw	57723	F160W	23.902 ± 0.204	0.082	20.203	0.187	0.002	0.000	0.000
DES16E2cxw	57730	F125W	22.455 ± 0.274	0.018	20.420	0.273	0.002	0.006	0.003
DES16E2cxw	57730	F160W	24.314 ± 0.213	0.102	20.203	0.187	0.002	0.000	0.000
PS1-440005	56229	F125W	22.965 ± 0.071	0.033	21.715	0.063	0.007	0.014	0.008
PS1-440005	56229	F160W	24.079 ± 0.127	0.090	21.387	0.090	0.007	0.000	0.000
PS1-440005	56235	F160W	24.502 ± 0.159	0.131	21.387	0.090	0.007	0.000	0.000
PS1-440005	56242	F125W	22.734 ± 0.070	0.031	21.715	0.063	0.007	0.011	0.007
PS1-440005	56242	F160W	24.137 ± 0.119	0.078	21.387	0.090	0.007	0.000	0.000
PS1-440005	56235	F125W	22.998 ± 0.075	0.042	21.715	0.063	0.007	0.014	0.008
PS1-520062	56473	F125W	23.082 ± 0.077	0.033	21.979	0.069	0.002	0.016	0.009
PS1-520062	56473	F160W	25.973 ± 0.315	0.310	21.769	0.056	0.002	0.000	0.000
PS1-520062	56482	F125W	22.894 ± 0.074	0.030	21.979	0.068	0.002	0.013	0.008
PS1-520062	56482	F160W	25.101 ± 0.197	0.189	21.769	0.056	0.002	0.000	0.000
PS1-520062	56468	F125W	23.087 ± 0.080	0.040	21.979	0.069	0.002	0.016	0.009
PS1-520062	56468	F160W	24.669 ± 0.100	0.084	21.769	0.054	0.002	0.000	0.000
PS1-500100	56424	F160W	24.034 ± 0.076	0.072	25.917	0.024	0.002	0.000	0.000
PS1- 500100	56424	F125W	22.806 ± 0.042	0.036	26.200	0.021	0.002	0.015	0.009
PS1-500100	56416	F160W	24.521 ± 0.116	0.114	25.917	0.021	0.002	0.000	0.000
PS1-500100	56411	F125W	23.141 ± 0.041	0.035	26.200	0.021	0.002	0.020	0.012
PS1-500100	56411	F160W	24.920 ± 0.134	0.133	25.917	0.016	0.002	0.000	0.000
PS1-500100	56416	F125W	22.959 ± 0.047	0.042	26.200	0.021	0.002	0.017	0.010
PS1-500301	56418	F125W	23.058 ± 0.166	0.038	21.263	0.161	0.002	0.027	0.016
PS1-500301	56431	F160W	23.823 ± 0.134	0.046	21.080	0.126	0.002	0.000	0.000
PS1-500301	56431	F125W	22.813 ± 0.164	0.030	21.263	0.162	0.002	0.021	0.012
PS1-500301	56423	F160W	23.995 ± 0.140	0.060	21.080	0.126	0.002	0.000	0.000
PS1-500301	56423	F125W	22.956 ± 0.166	0.037	21.263	0.161	0.002	0.025	0.014
PS1-500301	56418	F160W	24.027 ± 0.147	0.077	21.080	0.125	0.002	0.000	0.000
PS1-470041	56333	F160W	23.018 ± 0.193	0.026	20.335	0.191	0.018	0.000	0.000
PS1-470041	56333	F125W	22.488 ± 0.289	0.023	20.518	0.288	0.018	0.006	0.004
PS1-470041	56325	F160W	23.109 ± 0.193	0.019	20.335	0.192	0.018	0.000	0.000
PS1-470041	56325	F125W	22.632 ± 0.289	0.022	20.518	0.288	0.018	0.007	0.004
PS1-470041	56320	F160W	23.964 ± 0.205	0.074	20.335	0.191	0.018	0.000	0.000
PS1-470041	56320	F125W	23.121 ± 0.291	0.040	20.518	0.288	0.018	0.012	0.007
PS1-470041	56395	F125W	24.080 ± 0.302	0.091	20.518	0.288	0.018	0.028	0.016
PS1-470041	56395	F160W	23.642 ± 0.202	0.062	20.335	0.192	0.018	0.000	0.000
PS1-480794	56368	F125W	23.284 ± 0.053	0.034	23.014	0.041	0.002	0.013	0.007

Table 6
(Continued)

SNID	MJD	filter	$m_{\rm SN}$ (mag)	$\sigma_{\rm SN}$ (mag)	$m_{\rm host}$ (mag)	$\sigma_{\rm host}$ (mag)	σ_c ($''$)	$\Delta_m^{\rm tmpl}$ (mag)	$\sigma_{\rm tmpl}$ (mag)
PS1-480794	56361	F160W	24.189 ± 0.087	0.080	22.905	0.034	0.002	0.000	0.000
PS1-480794	56361	F125W	23.064 ± 0.058	0.040	23.014	0.042	0.002	0.010	0.006
PS1-480794	56355	F160W	23.786 ± 0.060	0.049	22.905	0.035	0.002	0.000	0.000
PS1-480794	56368	F160W	24.635 ± 0.165	0.161	22.905	0.036	0.002	0.000	0.000
PS1-480794	56355	F125W	22.887 ± 0.054	0.034	23.014	0.042	0.002	0.009	0.005
PS1- 490521	56396	F160W	23.974 ± 0.084	0.066	22.011	0.052	0.001	0.000	0.000
PS1-490521	56396	F125W	22.979 ± 0.080	0.032	22.226	0.073	0.001	0.005	0.003
PS1-490521	56389	F160W	24.295 ± 0.097	0.082	22.011	0.052	0.001	0.000	0.000
PS1-490521	56389	F125W	23.089 ± 0.079	0.027	22.226	0.074	0.001	0.006	0.003
PS1-490521	56383	F125W	23.197 ± 0.077	0.021	22.226	0.074	0.001	0.007	0.004
PS1-490521	56383	F160W	24.300 ± 0.081	0.062	22.011	0.052	0.001	0.000	0.000
PS1-470110	56326	F160W	24.419 ± 0.079	0.074	23.854	0.027	0.007	0.038	0.022
PS1-470110	56321	F125W	22.968 ± 0.054	0.038	23.948	0.038	0.007	0.022	0.013
PS1-470110	56321	F160W	23.979 ± 0.072	0.067	23.854	0.026	0.007	0.025	0.014
PS1-470110	56326	F125W	23.133 ± 0.058	0.045	23.948	0.037	0.007	0.026	0.015
PS1-470110	56334	F160W	24.592 ± 0.108	0.105	23.854	0.025	0.007	0.044	0.026
PS1-470110	56334	F125W	23.198 ± 0.053	0.038	23.948	0.037	0.007	0.027	0.016
DES16E2clk	57707	F125W	23.375 ± 0.058	0.036	22.835	0.046	0.001	0.010	0.006
DES16E2clk	57712	F160W	24.640 ± 0.147	0.141	22.709	0.042	0.001	0.014	0.008
DES16E2clk	57719	F125W	23.310 ± 0.054	0.028	22.835	0.046	0.001	0.009	0.005
DES16E2clk	57719	F160W	24.514 ± 0.117	0.111	22.709	0.037	0.001	0.012	0.007
DES16E2clk	57707	F160W	24.873 ± 0.195	0.191	22.709	0.039	0.001	0.017	0.010
DES16E2clk	57712	F125W	23.364 ± 0.053	0.028	22.835	0.046	0.001	0.010	0.006
DES16C2cva	57729	F160W	24.126 ± 0.074	0.054	22.106	0.051	0.015	0.007	0.004
DES16C2cva	57721	F160W	24.586 ± 0.081	0.063	22.106	0.051	0.015	0.010	0.006
DES16C2cva	57714	F160W	24.798 ± 0.090	0.074	22.106	0.051	0.015	0.012	0.007
DES15X2kvt	57321	F160W	24.926 ± 0.166	0.162	23.081	0.036	0.002	0.010	0.006
DES15X2kvt	57327	F160W	24.722 ± 0.131	0.126	23.081	0.036	0.002	0.008	0.005
DES15X2kvt	57337	F160W	24.081 ± 0.102	0.096	23.081	0.034	0.002	0.005	0.003
PS1-450339	56282	F125W	23.432 ± 0.070	0.063	24.447	0.031	0.001	0.010	0.006
PS1- 450339	56266	F125W	23.527 ± 0.060	0.052	24.447	0.030	0.001	0.011	0.007
PS1-450339	56266	F160W	24.604 ± 0.112	0.109	24.387	0.026	0.001	0.008	0.005
PS1-450339	56272	F125W	23.541 ± 0.059	0.051	24.447	0.030	0.001	0.011	0.007
PS1-450339	56282	F160W	24.293 ± 0.098	0.094	24.387	0.028	0.001	0.006	0.004
PS1-450339	56272	F160W	24.665 ± 0.140	0.137	24.387	0.029	0.001	0.008	0.005
DES15E2nlz	57404	F160W	24.366 ± 0.058	0.053	25.538	0.023	0.007	0.025	0.014
DES15E2nlz	57396	F160W	24.641 ± 0.065	0.061	25.538	0.022	0.007	0.032	0.018
DES15E2nlz	57390	F160W	24.604 ± 0.086	0.083	25.538	0.022	0.007	0.031	0.018
PS1-530251	56515	F125W	23.766 ± 0.092	0.087	25.038	0.030	0.002	0.015	0.009
PS1-530251	56508	F160W	24.884 ± 0.185	0.183	25.120	0.027	0.002	0.012	0.007
PS1-530251	56508	F125W	23.830 ± 0.100	0.096	25.038	0.028	0.002	0.016	0.009
PS1-530251	56502	F160W	24.541 ± 0.141	0.139	25.120	0.024	0.002	0.009	0.005
PS1-530251	56502	F125W	23.613 ± 0.068	0.062	25.038	0.030	0.002	0.013	0.008
PS1-530251	56515	F160W	24.662 ± 0.150	0.148	25.120	0.024	0.002	0.010	0.006
PS1-550202	56600	F160W	24.425 ± 0.070	0.057	22.584	0.042	0.002	0.014	0.008
PS1-550202	56586	F160W	24.761 ± 0.113	0.105	22.584	0.042	0.002	0.018	0.011
PS1-550202	56593	F125W	23.616 ± 0.069	0.043	22.692	0.054	0.002	0.023	0.013
PS1-550202	56593	F160W	24.661 ± 0.086	0.075	22.584	0.042	0.002	0.017	0.010
PS1-550202	56610	F160W	23.898 ± 0.052	0.030	22.584	0.042	0.002	0.008	0.005
PS1-550202	56586	F125W	23.520 ± 0.064	0.035	22.692	0.054	0.002	0.021	0.012
DES15C1nhv	57401	F160W	23.655 ± 0.045	0.036	24.039	0.026	0.001	0.025	0.015
DES15C1nhv	57387	F160W	24.035 ± 0.051	0.043	24.039	0.027	0.001	0.036	0.021
DES15C1nhv	57394	F160W	23.955 ± 0.045	0.036	24.039	0.026	0.001	0.034	0.020
PS1-490037	56390	F125W	23.568 ± 0.119	0.095	22.154	0.073	0.000	0.028	0.017
PS1-490037	56376	F125W	23.161 ± 0.092	0.057	22.154	0.072	0.000	0.019	0.011
PS1- 490037	56376	F160W	24.209 ± 0.153	0.144	21.858	0.052	0.000	0.014	0.008
PS1-490037	56381	F125W	23.358 ± 0.092	0.057	22.154	0.072	0.000	0.023	0.013
PS1-490037	56390	F160W	24.769 ± 0.231	0.225	21.858	0.052	0.000	0.025	0.014
PS1-490037	56381	F160W	24.450 ± 0.167	0.159	21.858	0.051	0.000	0.018	0.011
DES16E2cqq	57731	F160W	24.139 ± 0.050	0.037	23.247	0.034	0.002	0.006	0.003
DES16E2cqq	57721	F160W	24.552 ± 0.051	0.039	23.247	0.033	0.002	0.008	0.005
DES16E2cqq	57714	F160W	24.897 ± 0.082	0.075	23.247	0.033	0.002	0.011	0.007
PS1-440236	56242	F160W	24.150 ± 0.065	0.062	28.020	0.020	0.000	0.009	0.005

Table 6
(Continued)

SNID	MJD	filter	$m_{\rm SN}$ (mag)	$\sigma_{\rm SN}$ (mag)	$m_{\rm host}$ (mag)	$\sigma_{\rm host}$ (mag)	σ_c ($''$)	$\Delta_m^{\rm tmpl}$ (mag)	$\sigma_{\rm tmpl}$ (mag)
PS1-440236	56234	F125W	23.580 ± 0.042	0.037	29.261	0.021	0.000	0.019	0.011
PS1-440236	56234	F160W	24.640 ± 0.094	0.092	28.020	0.019	0.000	0.014	0.008
PS1-440236	56242	F125W	23.471 ± 0.036	0.030	29.261	0.021	0.000	0.018	0.010
PS1-440236	56229	F160W	24.872 ± 0.129	0.127	28.020	0.023	0.000	0.017	0.010
PS1-440236	56229	F125W	23.659 ± 0.041	0.034	29.261	0.022	0.000	0.021	0.012
PS1-470240	56333	F160W	24.507 ± 0.076	0.076	⋯	⋯	0.001	⋯	⋯
PS1-470240	56333	F125W	23.638 ± 0.039	0.039	⋯	⋯	0.001	⋯	⋯
PS1-470240	56350	F125W	23.469 ± 0.040	0.040	⋯	⋯	0.001	⋯	⋯
PS1-470240	56350	F160W	23.779 ± 0.045	0.045	⋯	⋯	0.001	⋯	⋯
PS1-470240	56325	F160W	24.662 ± 0.047	0.047	⋯	⋯	0.001	⋯	⋯
PS1-470240	56325	F125W	23.659 ± 0.055	0.055	⋯	⋯	0.001	⋯	⋯
PS1-470240	56320	F160W	24.561 ± 0.066	0.066	⋯	⋯	0.001	⋯	⋯
PS1-470240	56320	F125W	23.522 ± 0.037	0.037	⋯	⋯	0.001	⋯	⋯
DES16X1cpf	57708	F160W	23.703 ± 0.201	0.034	20.531	0.198	0.004	0.010	0.006
DES16X1cpf	57716	F160W	23.592 ± 0.200	0.025	20.531	0.199	0.004	0.009	0.005
DES16X1cpf	57723	F160W	23.424 ± 0.200	0.026	20.531	0.198	0.004	0.008	0.005
DES15E2mhy	57357	F160W	24.070 ± 0.072	0.049	21.922	0.053	0.002	0.027	0.016
DES15E2mhy	57373	F160W	24.293 ± 0.078	0.057	21.922	0.053	0.002	0.033	0.020
DES15E2mhy	57363	F160W	24.378 ± 0.078	0.058	21.922	0.052	0.002	0.036	0.021
PS1- 560027	56601	F160W	24.147 ± 0.082	0.079	25.655	0.022	0.001	0.007	0.004
PS1-560027	56593	F125W	23.494 ± 0.041	0.036	26.393	0.019	0.001	0.014	0.008
PS1-560027	56593	F160W	24.495 ± 0.090	0.087	25.655	0.023	0.001	0.010	0.006
PS1-560027	56611	F160W	23.800 ± 0.049	0.044	25.655	0.022	0.001	0.005	0.003
PS1-560027	56587	F125W	23.509 ± 0.043	0.038	26.393	0.020	0.001	0.015	0.009
PS1-560027	56587	F160W	24.784 ± 0.124	0.122	25.655	0.022	0.001	0.013	0.008
DES16E1dcx	57715	F160W	24.177 ± 0.135	0.124	21.997	0.053	0.002	0.004	0.002
DES16E1dcx	57730	F160W	24.218 ± 0.076	0.055	21.997	0.052	0.002	0.004	0.003
DES16E1dcx	57730	F125W	23.525 ± 0.083	0.047	22.416	0.068	0.002	0.007	0.004
DES16E1dcx	57722	F160W	24.594 ± 0.143	0.133	21.997	0.053	0.002	0.006	0.004
DES16E1dcx	57722	F125W	23.733 ± 0.084	0.049	22.416	0.068	0.002	0.009	0.005
DES16E1dcx	57715	F125W	23.487 ± 0.083	0.048	22.416	0.068	0.002	0.007	0.004
DES15X2nkz	57384	F160W	24.529 ± 0.074	0.069	23.892	0.029	0.003	0.032	0.019
DES15X2nkz	57391	F160W	24.853 ± 0.108	0.104	23.892	0.029	0.003	0.042	0.025
DES15X2nkz	57399	F160W	24.630 ± 0.082	0.078	23.892	0.028	0.003	0.035	0.020
DES16S1bno	57686	F160W	24.823 ± 0.084	0.080	26.342	0.026	0.001	0.009	0.006
DES16S1bno	57693	F160W	24.409 ± 0.074	0.070	26.342	0.024	0.001	0.007	0.004
DES16S1bno	57701	F160W	24.134 ± 0.054	0.048	26.342	0.025	0.001	0.005	0.003
PS1-540118	56528	F160W	24.572 ± 0.097	0.091	23.302	0.033	0.001	0.017	0.010
PS1-540118	56536	F160W	24.721 ± 0.099	0.093	23.302	0.034	0.001	0.020	0.012
PS1-540118	56523	F160W	24.262 ± 0.077	0.070	23.302	0.032	0.001	0.013	0.008
PS1-560054	56603	F125W	23.667 ± 0.073	0.063	24.039	0.038	0.001	0.024	0.014
PS1-560054	56587	F160W	24.522 ± 0.109	0.106	23.871	0.025	0.001	0.017	0.010
PS1-560054	56587	F125W	23.444 ± 0.066	0.055	24.039	0.036	0.001	0.019	0.011
PS1-560054	56592	F160W	24.831 ± 0.192	0.190	23.871	0.028	0.001	0.022	0.013
PS1- 560054	56603	F160W	24.432 ± 0.116	0.112	23.871	0.030	0.001	0.015	0.009
PS1-560054	56592	F125W	23.726 ± 0.102	0.095	24.039	0.037	0.001	0.025	0.015
DES16S2afz	57657	F160W	24.244 ± 0.065	0.052	22.778	0.039	0.016	0.005	0.003
DES16S2afz	57663	F160W	24.420 ± 0.085	0.076	22.778	0.038	0.016	0.007	0.004
DES16S2afz	57671	F160W	24.296 ± 0.072	0.061	22.778	0.038	0.016	0.006	0.003
DES16E2rd	57657	F160W	23.980 ± 0.195	0.074	19.559	0.180	0.007	0.030	0.018
DES16E2rd	57663	F160W	24.049 ± 0.200	0.087	19.559	0.180	0.007	0.032	0.019
DES16E2rd	57671	F160W	23.632 ± 0.191	0.064	19.559	0.180	0.007	0.021	0.012
DES16X3zd	57657	F160W	24.558 ± 0.124	0.120	23.247	0.031	0.001	0.018	0.010
DES16X3zd	57663	F160W	24.546 ± 0.102	0.098	23.247	0.032	0.001	0.018	0.010
DES16X3zd	57672	F160W	24.240 ± 0.113	0.108	23.247	0.033	0.001	0.013	0.008
PS1-510457	56457	F160W	25.043 ± 0.112	0.098	21.964	0.054	0.002	0.033	0.019
PS1-510457	56444	F160W	25.221 ± 0.121	0.108	21.964	0.054	0.002	0.039	0.023
PS1-510457	56439	F160W	25.086 ± 0.088	0.071	21.964	0.053	0.002	0.034	0.020
DES16S1agd	57672	F160W	24.285 ± 0.063	0.051	22.833	0.037	0.003	0.009	0.005
DES16S1agd	57657	F160W	24.565 ± 0.085	0.076	22.833	0.038	0.003	0.011	0.007
DES16S1agd	57663	F160W	24.501 ± 0.104	0.098	22.833	0.035	0.003	0.011	0.006
DES15C3odz	57429	F160W	24.508 ± 0.065	0.061	25.733	0.022	0.007	0.021	0.012
DES15C3odz	57421	F160W	25.022 ± 0.094	0.091	25.733	0.023	0.007	0.033	0.019

Table 6
(Continued)

SNID	MJD	filter	m_{SN} (mag)	σ_{SN} (mag)	m_{host} (mag)	σ_{host} (mag)	σ_c ($''$)	Δ_m^{tmpl} (mag)	σ_{tmpl} (mag)
DES15C3odz	57414	F160W	25.291 ± 0.136	0.134	25.733	0.023	0.007	0.042	0.025
PS1-520107	56473	F160W	24.132 ± 0.055	0.048	23.998	0.027	0.001	0.036	0.021
PS1-520107	56482	F160W	24.114 ± 0.058	0.051	23.998	0.027	0.001	0.035	0.020
PS1-520107	56468	F160W	24.064 ± 0.049	0.041	23.998	0.027	0.001	0.034	0.020
DES16C1cim	57721	F160W	24.318 ± 0.060	0.050	23.086	0.033	0.002	0.007	0.004
DES16C1cim	57712	F160W	24.527 ± 0.063	0.053	23.086	0.034	0.002	0.008	0.005
DES16C1cim	57706	F160W	24.772 ± 0.095	0.088	23.086	0.036	0.002	0.010	0.006
DES16C3cmy	57706	F160W	24.541 ± 0.068	0.064	25.646	0.023	0.001	0.010	0.006
DES16C3cmy	57720	F160W	24.492 ± 0.061	0.057	25.646	0.022	0.001	0.010	0.006
DES16C3cmy	57712	F160W	24.743 ± 0.075	0.071	25.646	0.024	0.001	0.012	0.007
DES15E2uc	57293	F160W	24.889 ± 0.081	0.075	23.465	0.030	0.016	0.029	0.017
DES15E2uc	57299	F160W	24.614 ± 0.082	0.075	23.465	0.033	0.016	0.022	0.013
DES15E2uc	57309	F160W	24.396 ± 0.060	0.051	23.465	0.031	0.016	0.018	0.011
DES15X2mey	57357	F160W	24.556 ± 0.092	0.086	23.068	0.032	0.001	0.029	0.017
DES15X2mey	57365	F160W	24.722 ± 0.092	0.086	23.068	0.032	0.001	0.034	0.020
DES15X2mey	57374	F160W	24.525 ± 0.083	0.075	23.068	0.035	0.001	0.029	0.017
DES16X3cry	57713	F125W	24.019 ± 0.043	0.026	24.218	0.034	0.001	0.007	0.004
DES16X3cry	57720	F125W	24.500 ± 0.051	0.037	24.218	0.035	0.001	0.011	0.006
DES16X3cry	57720	F160W	24.626 ± 0.054	0.046	24.015	0.028	0.001	0.007	0.004
DES16X3cry	57728	F125W	24.455 ± 0.064	0.054	24.218	0.034	0.001	0.011	0.006
DES16X3cry	57728	F160W	24.349 ± 0.080	0.076	24.015	0.025	0.001	0.006	0.003

Appendix C
Simulating the RAISIN Sample

Here we describe our simulations of the RAISIN sample. These simulations rely on an optical selection function that was determined for the PS1 and DES analyses (Scolnic et al. 2018; Kessler et al. 2019). We modeled the sample under the assumption that the RAISIN SNe were selected in an unbiased way from the subset of Pan-STARRS and DES SNe with spectroscopic classifications, and the typical S/N of the RAISIN optical light curves compared to the full PS1/DES spectroscopic samples shows this to be a reasonable approximation. Though RAISIN targeted SNe in specific redshift ranges, those redshift ranges—$0.25 < z < 0.45$ for RAISIN1 and $0.4 < z < 0.6$ for RAISIN2—were within one standard deviation of the mean redshifts of the PS1 and DES SN spectroscopic surveys. Therefore, much of the necessary work for building these simulations for RAISIN was already undertaken by the MDS and DES teams. The main difference for RAISIN is the use of a new SN model, SNooPy, with the new optical-to-NIR dispersion model discussed in Section 3.3. We implemented the SNooPy model in SNANA by using the `Python`-based SNooPy code to generate a grid of model realizations as a function of s_{BV} and A_V, which SNANA may then use for both simulations and light-curve fitting (Figure 6). We then added a module to the SNANA simulation engine containing the SNooPy dispersion model, which generates correlated-random band-to-band offsets to be applied to the simulated magnitudes; this results in simulated distance-dependent biases. Both the SNooPy models and the SNooPy dispersion model are publicly available in SNANA.

For the low-z simulations, we do not have sky noise and zero-point information for the original NIR observations. However, SNANA is able to estimate these quantities by using the magnitudes and uncertainties in the data themselves to create a "simulation library." Other low-z survey characteristics and selection effects were modeled in the Pantheon analysis (Scolnic et al. 2018), and we use the magnitude-based SN detection efficiency determined in that work to simulate the low-z CSP sample here. For the high-z simulations, our simulation library is built from observations of the RAISIN SNe themselves, which allows us to simulate SNe at the specific redshifts of the RAISIN objects and control for possible differences between the mean survey observing conditions and the conditions during which the RAISIN SNe were observed.

Finally, we require that simulated distributions of x_1 and c parameters for SALT2 are replaced by distributions of the stretch parameter s_{BV} and the extinction A_V. Even though the light curves in NIR bands are less sensitive to s_{BV} and A_V than those in optical bands, an NIR-only approach with the RAISIN data does not allow shape/color to be corrected for, and therefore the results will be very sensitive to sample-to-sample differences in these parameters and the optical selection effects that will bias the sample toward, e.g., high s_{BV} and low A_V. We therefore adapt the method of Scolnic & Kessler (2016) to determine the intrinsic s_{BV} distribution for the low-z and high-z samples. The distribution of the s_{BV} parameter is treated as an asymmetric Gaussian following Scolnic & Kessler (2016), and we estimate the s_{BV} distribution by fitting s_{BV} with our NIR data.

For A_V, our baseline analysis assumes that the mean intrinsic dust extinction is independent of redshift, but we vary this assumption in our systematic error budget. We simulate an exponential dust distribution with $\tau_{A_V} = 0.2$ mag, which we find is a good approximate match to the optical+NIR data in Figure 22 and matches nominal dust distributions from the SN rate analysis of Rodney et al. (2014). We also find that varying τ globally has a minimal impact on the redshift dependence of our predicted bias corrections. Our two A_V-related systematic uncertainty analysis variants reduce the A_V scale length first by 0.05 for both samples (a small additional uncertainty) and second by 0.05 for the low-z sample only.

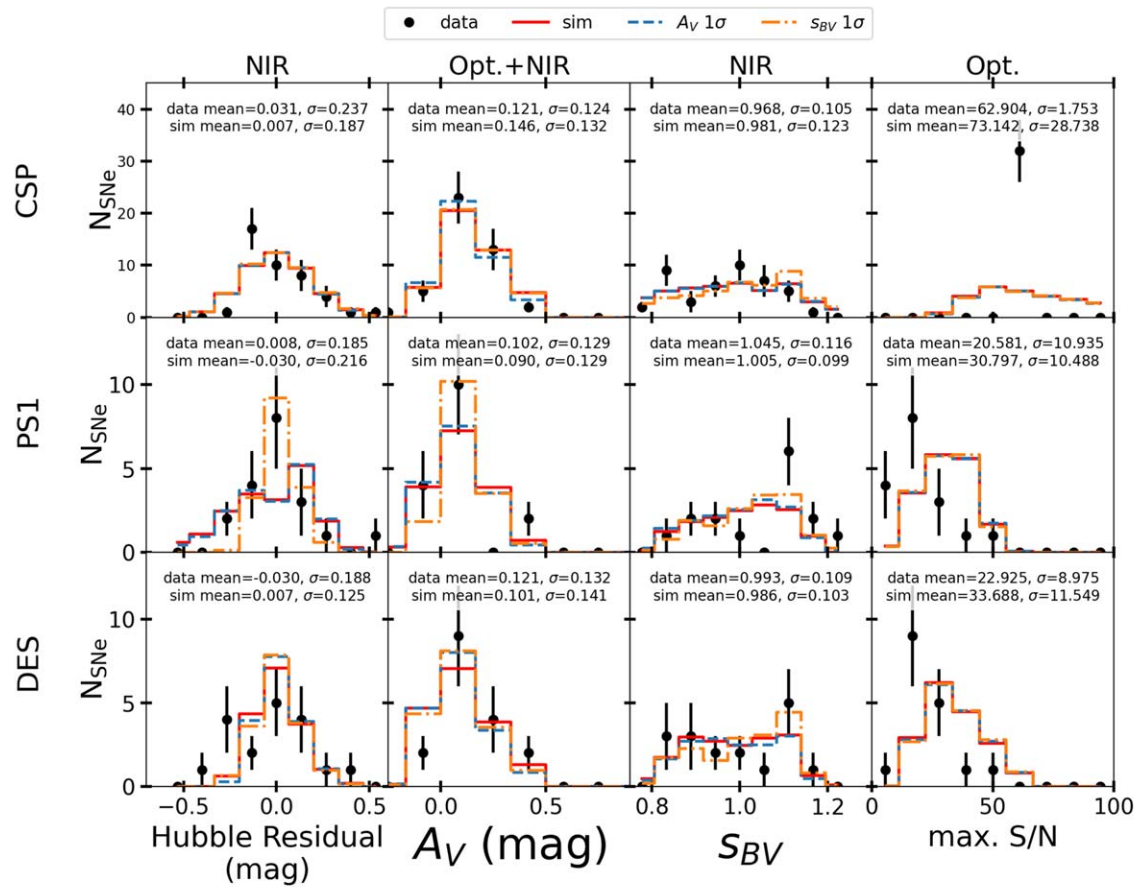

Figure 22. RAISIN simulations (red) compared to the data (black). Histograms of Hubble residuals, A_V, s_{BV}, and maximum S/N are shown for the CSP sample (top), the RAISIN1 sample (middle), and the RAISIN2 sample (bottom). Various combinations of data are used for comparison purposes as indicated above each column. Simulations after applying a 1σ shift to parameters of the A_V and s_{BV} distributions are shown in blue and orange, respectively. Some discrepancy in maximum S/N may be due to statistical fluctuation due to the small sample sizes in this analysis or uncertainty in the chosen SNooPy model.

The low-z sample from CSP used a galaxy-targeted approach to find SNe, which gives a sample of predominantly massive host galaxies and, as a result, increases the fraction of fast-declining SNe in the sample (Childress et al. 2013). For this reason we assume a priori that the low-z and RAISIN samples have different intrinsic stretch and color distributions. However, because the DES and MDS samples were selected in much the same way, and to avoid statistical noise, we assume that the intrinsic distributions of shape and color in these SN samples are the same. This is an approximation that is necessary owing to limited statistics, but the Scolnic & Kessler (2016) measurements of intrinsic population parameters in high-z samples show that this may be a good approximation. However, some evolution in population parameters (Nicolas et al. 2021) is expected, and larger samples at both high and low z in future analyses will allow constraints on this evolution, as well as a more robust determination of the stretch and color distributions themselves.

The resulting stretch and color distributions are shown in Figure 22. We find that both the s_{BV} and A_V distributions are statistically consistent between low- and high-z samples, albeit with relatively large uncertainties.

Finally, throughout this analysis we assume the default SNooPy total-to-selective extinction ratio of $R_V = 1.52$ from Folatelli (2010, their Table 8), which reduces dispersion about the Hubble diagram compared to choosing the MW value of $R_V = 3.1$ (Figure 18). The lower-than-expected value of R_V may be due to the lack of an intrinsic color variation component of the SNooPy model (Thorp et al. 2021; Mandel et al. 2022) and the fact that extinction is allowed to be (unphysically) negative in this analysis. By using the CSP third data release and allowing SNooPy to fit for R_V, we find that SNooPy gives a median $R_V \simeq 2$, though unfortunately we find that the high-z RAISIN data are insufficient to constrain R_V with SNooPy.

Because data at NIR wavelengths are a factor of ∼4–5 less sensitive to dust than the optical, distance error due to uncertainty in the value of R_V is a sub-percent-level effect and will not be a significant component of the error budget in this analysis. We note that in the NIR fitting itself we treat A_V as a constant, and therefore this effect will only change the distances in the bias correction stage.

The maximum S/N distributions are shown on the right side of Figure 22. Generally, the simulations expect slightly higher S/N than is observed in the data for high z. Because the larger PS1 and DES samples have a similar S/N near maximum light compared to the subset with RAISIN observations—nearly identical for PS1 and marginally higher S/N in the DES RAISIN subset—we choose not to modify the simulations here. The low-z S/N, on the other hand, has an unusual shape that we were unable to reproduce, perhaps due to small sample sizes; in the full SNooPy sample, before applying our selection cuts, we do not see the same concentration around a narrow range of S/N. In future, larger NIR samples it will be much easier to understand such artifacts in the data. We are unsure whether the NIR sample was selected in the same way as the rest of the CSP sample, but we assume that for this analysis; the simulations developed for past analyses are therefore sufficient given systematic uncertainties on the s_{BV} and A_V distributions. A low-z sample that selects NIR-observed SNe in an unbiased way is a key potential improvement for future cosmological analyses.

C.1. Distance Measurement Methodologies

Using the RAISIN simulations, we test the assumption that NIR-only distance measurements are most precise when s_{BV} and A_V are fixed to a constant value. From simulations, we measure a Hubble residual rms of 0.16 mag, slightly lower than the 0.19 mag measured from the real RAISIN data, when s_{BV} and A_V are fixed to a constant. When we attempt to use the NIR data alone to fit for A_V, the Hubble residual rms increases to 0.28 mag, and when we fit for both s_{BV} and A_V, we measure an rms of 0.25 mag. However, when we use the NIR data alone to fit for s_{BV}, we find that the rms is unchanged from the s_{BV} fixed case; this may be because the simulated SNooPy model does not include the increase in scatter at later phases that we observe and discuss in Section 5.3. However, despite this modest discrepancy, both the simulations and real RAISIN data appear to show no benefit from fitting to A_V and/or s_{BV} with NIR data alone.

Appendix D
Host Mass Measurement

Host galaxy masses were reported by the CSP, DES, and MDS teams (Krisciunas et al. 2017; Jones et al. 2018b; Smith et al. 2020). However, to ensure consistency between all methods, we estimated the host galaxy masses of SNe in the RAISIN and low-z samples ourselves. For the low-z sample we used data from GALEX (Martin et al. 2005), Sloan Digital Sky Survey (SDSS) DR16 (Ahumada et al. 2020), PS1 DR2 (Flewelling et al. 2020), and the Two Micron All Sky Survey (2MASS; Skrutskie et al. 2006), while for the high-z sample we used only SDSS and PS1 as the other catalogs do not have sufficient depth for the faint, high-z RAISIN galaxies. For RAISIN2, we also used SN-free DES photometry from Wiseman et al. (2020). Finally, because PS1 3π images may be contaminated by SN light, we used MDS single-season template images for RAISIN1 SNe. The stacked images make it possible to detect $\log(M_*/M_\odot) = 10$ SN host galaxies with sufficient depth to measure masses on either side of the typical mass step location.

To find the host galaxy for each SN, we use SExtractor to determine the "directional light radius" between potential host galaxies and each SN (Sullivan et al. 2006; Gupta et al. 2016), a method that incorporates the size and orientation of each galaxy to determine which galaxy is the most likely host. Each most probable host was confirmed by eye, and thanks to HST imaging, we were able to determine which galaxies were the host without significant ambiguity. We then used SExtractor to measure the elliptical parameters of each galaxy in the r band, and then we used elliptical aperture photometry to measure the magnitudes of each galaxy in each available bandpass. The aperture size was chosen to extend slightly beyond the isophotal radius determined by SExtractor and was also extended to account for the increased PSF sizes of 2MASS and WISE. Any contamination by foreground stars was removed by using SExtractor to identify possible contaminants and masking those objects by setting the value of the pixels SExtractor deemed as belonging to those objects to the median value of the nearby pixels.

Once aperture photometry was measured, we used LePHARE (Arnouts & Ilbert 2011) with Bruzual & Charlot (2003) spectral templates and a Chabrier initial mass function (Chabrier 2003) to determine the stellar masses of each host galaxy. The templates include nine exponentially decreasing star formation histories in three metallicity bins, and we allow $E(B-V)$ to vary from 0 to 0.4 in steps of 0.1 mag with a range of extinction laws. Uncertainties on these masses were estimated by Monte Carlo sampling of the photometry using the photometric uncertainties for each band and assuming a 1% error floor for bright galaxies. We note that mass estimation requires determining an absolute magnitude, making these mass estimates dependent on an assumed cosmology and the SN brightness residual. However, none of our mass estimates would change from <10 dex to >10 dex with modest adjustments in cosmological parameters; a 20% shift in w at a redshift of 0.6 would result in a systematic shift of just 0.03 dex relative to a low-z mass.

We compare these masses to estimates from Roman et al. (2018) for the low-z sample and Smith et al. (2020) for the high-z sample. Out of the 15 SNe with host masses in Roman et al. (2018), only one SN, SN 2004ey, disagrees with our high- versus low-mass designations. We do see a large median offset of -0.5 dex when subtracting the Roman et al. (2018) masses from ours, but we find that this is due to our addition of GALEX and 2MASS data; running LePHARE on our optical-only measurements gives a marginally significant median difference of $+0.21 \pm 0.08$ dex for these SNe. For DES masses, we find a median difference of just 0.06 dex between our masses and those of Smith et al. (2020), with no disagreement between our high- and low-mass designations. Figure 8 shows histograms of the masses for CSP, RAISIN1, and RAISIN2 SNe; due to the targeted nature of the low-z CSP data, the CSP SNe are found in significantly more massive host galaxies.

For a given mass step location, with $\log(M_*/M_\odot) = 10$ as the default, we assume that the uncertainties on the mass estimates are Gaussian and use these uncertainties to compute the probability that each SN has a mass greater than or less than the value at the step location. We then built a maximum likelihood, Gaussian mixture model that includes free parameters of the intrinsic dispersions for CSP, RAISIN1, and RAISIN2 (RAISIN2 has higher dispersion, as it uses one filter instead of two for most SNe); median Hubble residuals at low, medium, and high redshifts to remove sensitivity to the cosmological model; and a single mass step parameter. This procedure largely follows Jones et al. (2018a). We correct for the measured mass step in our data and apply two systematic uncertainties based on the value and location of the mass step as discussed in Section 3.7.4.

Appendix E
Distance Measurements for RAISIN and Low-*z* SNe

Table 7 contains NIR distances and optical+NIR stretch (s_{BV}) and A_V measurements for RAISIN, computed using SNooPy and assuming an R_V of 1.52.

Table 7
RAISIN Distances and Cuts

ID	$z_{\rm Helio}$	Raw Distance (mag)	Rest-frame Bands	Bias Corr. (mag)	$\sigma_{\rm tmax}$ (days)	Avg. $\sigma_{\rm phot}$ (mag)	Cuts
PS1-480464	0.220	40.188 ± 0.033	Y, J	0.040	0.120	0.073	⋯
PS1-450082	0.250	⋯	⋯	⋯	0.310	0.234	bad host sub.
PS1-540087	0.275	40.621 ± 0.043	Y, J	0.073	0.350	0.145	⋯
PS1-520188	0.280	40.350 ± 0.025	Y, J	0.073	0.050	0.040	⋯
DES16E2cxw	0.293	⋯	⋯	⋯	0.160	0.237	bad host sub.
PS1-440005	0.306	40.771 ± 0.044	Y, J	0.049	0.410	0.102	⋯
PS1-520062	0.308	41.168 ± 0.047	Y, J	0.049	0.290	0.128	⋯
PS1-500100	0.310	40.991 ± 0.032	Y, J	0.046	0.390	0.069	⋯
PS1-500301	0.325	40.727 ± 0.068	Y, J	0.038	0.420	0.145	⋯
PS1-470041	0.331	⋯	⋯	⋯	0.120	0.242	bad host sub.
PS1-480794	0.334	⋯	⋯	⋯	0.280	0.077	high s_{BV}
PS1-490521	0.340	40.982 ± 0.042	Y, J	0.033	0.430	0.082	⋯
PS1-470110	0.346	41.128 ± 0.033	Y, J	0.035	0.190	0.074	⋯
DES16E2clk	0.367	41.340 ± 0.039	Y, J	0.041	0.240	0.103	⋯
DES16C2cva	0.403	41.699 ± 0.055	Y	0.019	0.330	0.080	⋯
DES15X2kvt	0.404	41.741 ± 0.078	Y	0.019	0.710	0.132	⋯
PS1-450339	0.410	41.577 ± 0.034	i, Y	0.022	0.450	0.082	⋯
PS1-530251	0.413	41.720 ± 0.045	i, Y	0.024	0.500	0.120	⋯
DES15E2nlz	0.410	41.715 ± 0.047	Y	0.021	0.390	0.066	⋯
DES15C1nhv	0.421	⋯	⋯	⋯	0.370	0.043	Chauvenet
PS1-550202	0.422	41.698 ± 0.033	i, Y	0.025	0.800	0.073	⋯
PS1-490037	0.422	41.500 ± 0.051	i, Y	0.025	0.370	0.147	⋯
DES16E2cqq	0.426	41.905 ± 0.042	Y	0.025	0.380	0.063	⋯
PS1-470240	0.430	41.712 ± 0.024	i, Y	0.025	0.410	0.065	⋯
DES16X1cpf	0.436	⋯	⋯	⋯	0.380	0.201	bad host sub.
PS1-440236	0.430	41.732 ± 0.024	i, Y	0.025	0.340	0.070	⋯
DES15E2mhy	0.439	41.528 ± 0.051	Y	0.029	0.340	0.079	⋯
PS1- 560027	0.440	41.690 ± 0.027	i, Y	0.024	0.210	0.075	⋯
DES16E1dcx	0.453	41.679 ± 0.040	i, Y	0.029	0.340	0.105	⋯
DES15X2nkz	0.469	42.025 ± 0.056	Y	0.037	0.560	0.095	⋯
DES16S1bno	0.470	42.094 ± 0.046	Y	0.037	0.510	0.076	⋯
PS1-540118	0.477	41.938 ± 0.058	Y	0.004	0.490	0.084	⋯
PS1-560054	0.482	41.813 ± 0.040	i, Y	0.004	0.250	0.112	⋯
DES16S2afz	0.483	41.706 ± 0.051	Y	0.033	0.300	0.068	⋯
DES16E2rd	0.494	⋯	⋯	⋯	0.210	0.194	bad host sub.
DES16X3zd	0.495	41.905 ± 0.071	Y	0.030	0.220	0.103	⋯
PS1-510457	0.502	42.625 ± 0.065	Y	0.004	0.890	0.106	⋯
DES16S1agd	0.504	41.925 ± 0.055	Y	0.031	0.490	0.086	⋯
DES15C3odz	0.508	42.538 ± 0.058	Y	0.031	0.320	0.094	⋯
PS1-520107	0.519	⋯	⋯	⋯	1.960	0.049	possible non-Ia
DES16C1cim	0.531	42.282 ± 0.049	Y	0.024	0.570	0.070	⋯
DES16C3cmy	0.556	42.326 ± 0.048	Y	0.017	0.250	0.066	⋯
DES15E2uc	0.566	42.710 ± 0.048	Y	0.019	0.640	0.070	⋯
DES15X2mey	0.608	42.700 ± 0.058	Y	0.025	0.280	0.093	⋯
DES16X3cry	0.612	42.567 ± 0.028	i, Y	0.025	0.340	0.062	⋯

Note. Distance moduli from RAISIN SNe, calibrated to our best-fit H_0 of 75.4 km s^{-1} Mpc^{-1}. The "raw distance" (Column (3)) does not include the bias correction (Column (5)), which is added to the raw distance prior to cosmological parameter fitting. "Rest-frame Bands" (Column (4)) indicates the rest-frame SNooPy templates that were used to fit the RAISIN observations.

ORCID iDs

D. O. Jones https://orcid.org/0000-0002-6230-0151
K. S. Mandel https://orcid.org/0000-0001-9846-4417
R. P. Kirshner https://orcid.org/0000-0002-1966-3942
A. Avelino https://orcid.org/0000-0002-2938-7822
D. Brout https://orcid.org/0000-0001-5201-8374
C. Burns https://orcid.org/0000-0003-4625-6629
R. J. Foley https://orcid.org/0000-0002-2445-5275
Y.-C. Pan https://orcid.org/0000-0001-8415-6720
M. R. Siebert https://orcid.org/0000-0003-2445-3891
R. Chornock https://orcid.org/0000-0002-7706-5668
W. L. Freedman https://orcid.org/0000-0003-3431-9135
A. Friedman https://orcid.org/0000-0003-1334-039X
L. Galbany https://orcid.org/0000-0002-1296-6887
E. Hsiao https://orcid.org/0000-0003-1039-2928
G. H. Marion https://orcid.org/0000-0002-2966-3508
P. E. Nugent https://orcid.org/0000-0002-3389-0586
M. M. Phillips https://orcid.org/0000-0003-2734-0796
A. Rest https://orcid.org/0000-0002-4410-5387
A. G. Riess https://orcid.org/0000-0002-6124-1196

M. Sako https://orcid.org/0000-0003-2764-7093
M. Smith https://orcid.org/0000-0002-3321-1432
W. M. Wood-Vasey https://orcid.org/0000-0001-7113-1233

References

Abbott, T. M. C., Abdalla, F. B., Allam, S., et al. 2018, ApJS, 239, 18
Ahumada, R., Allende Prieto, C., Almeida, A., et al. 2020, ApJS, 249, 3
Aldering, G., Adam, G., Antilogus, P., et al. 2002, Proc. SPIE, 4836, 61
Anand, G. S., Tully, R. B., Rizzi, L., Riess, A. G., & Yuan, W. 2022, ApJ, 932, 15
Arnouts, S., & Ilbert, O. 2011, LePHARE: Photometric Analysis for Redshift Estimate, Astrophysics Source Code Library, ascl:1108.009
Avelino, A., Friedman, A. S., Mandel, K. S., et al. 2019, ApJ, 887, 106
Barone-Nugent, R. L., Lidman, C., Wyithe, J. S. B., et al. 2012, MNRAS, 425, 1007
Becker, A. 2015, HOTPANTS: High Order Transform of PSF ANd Template Subtraction, Astrophysics Source Code Library, ascl:1504.004
Betoule, M., Kessler, R., Guy, J., et al. 2014, A&A, 568, A22
Blondin, S., & Tonry, J. L. 2007, ApJ, 666, 1024
Bohlin, R. C., Hubeny, I., & Rauch, T. 2020, AJ, 160, 21
Brout, D., Sako, M., Scolnic, D., et al. 2019a, ApJ, 874, 106
Brout, D., & Scolnic, D. 2021, ApJ, 909, 26
Brout, D., Scolnic, D., Kessler, R., et al. 2019b, ApJ, 874, 150
Brout, D., Scolnic, D., Popovic, B., et al. 2022, arXiv:2202.04077
Brout, D., Taylor, G., Scolnic, D., et al. 2021, arXiv:2112.03864
Bruzual, G., & Charlot, S. 2003, MNRAS, 344, 1000
Burke, D. L., Rykoff, E. S., Allam, S., et al. 2018, AJ, 155, 41
Burns, C. R., Parent, E., Phillips, M. M., et al. 2018, ApJ, 869, 56
Burns, C. R., Stritzinger, M., Phillips, M. M., et al. 2011, AJ, 141, 19
Burns, C. R., Stritzinger, M., Phillips, M. M., et al. 2014, ApJ, 789, 32
Castelli, F., & Kurucz, R. L. 2003, in IAU Symp. 210, Modelling of Stellar Atmospheres, ed. N. Piskunov, W. W. Weiss, & D. F. Gray (Cambridge: Cambridge Univ. Press), A20
Chabrier, G. 2003, PASP, 115, 763
Chambers, K. C., Magnier, E. A., Metcalfe, N., et al. 2016, arXiv:1612.05560
Childress, M., Aldering, G., Antilogus, P., et al. 2013, ApJ, 770, 108
Conley, A., Sullivan, M., Hsiao, E. Y., et al. 2008, ApJ, 681, 482
Contreras, C., Hamuy, M., Phillips, M. M., et al. 2010, AJ, 139, 519
Contreras, C., Phillips, M. M., Burns, C. R., et al. 2018, ApJ, 859, 24
Cuesta, A. J., Verde, L., Riess, A., & Jimenez, R. 2015, MNRAS, 448, 3463
Dhawan, S., Brout, D., Scolnic, D., et al. 2020, ApJ, 894, 54
Dhawan, S., Jha, S. W., & Leibundgut, B. 2018, A&A, 609, A72
Flewelling, H. A., Magnier, E. A., Chambers, K. C., et al. 2020, ApJS, 251, 7
Folatelli, G., Phillips, M. M., Burns, C. R., et al. 2010, AJ, 139, 120
Foley, R. J., Narayan, G., Challis, P. J., et al. 2010, ApJ, 708, 1748
Foreman-Mackey, D. 2016, JOSS, 1, 24
Freedman, W. L., Burns, C. R., Phillips, M. M., et al. 2009, ApJ, 704, 1036
Freedman, W. L., Madore, B. F., Hatt, D., et al. 2019, ApJ, 882, 34
Friedman, A. S., Wood-Vasey, W. M., Marion, G. H., et al. 2015, ApJS, 220, 9
Fruchter, A. S., & Hook, R. N. 2002, PASP, 114, 144
Gall, C., Stritzinger, M. D., Ashall, C., et al. 2018, A&A, 611, A58
Grogin, N. A., Kocevski, D. D., Faber, S. M., et al. 2011, ApJS, 197, 35
Gupta, R. R., Kuhlmann, S., Kovacs, E., et al. 2016, AJ, 152, 154
Guy, J., Astier, P., Baumont, S., et al. 2007, A&A, 466, 11
Guy, J., Sullivan, M., Conley, A., et al. 2010, A&A, 523, A7
Hamuy, M., Phillips, M. M., Suntzeff, N. B., et al. 1996, AJ, 112, 2398
Hayden, B. T., Gupta, R. R., Garnavich, P. M., et al. 2013, ApJ, 764, 191
Hinton, S. R., Davis, T. M., Lidman, C., Glazebrook, K., & Lewis, G. F. 2016, A&C, 15, 61
Holtzman, J. A., Marriner, J., Kessler, R., et al. 2008, AJ, 136, 2306
Hounsell, R., Scolnic, D., Foley, R. J., et al. 2018, ApJ, 867, 23
Hsiao, E. Y., Conley, A., Howell, D. A., et al. 2007, ApJ, 663, 1187
Hsiao, E. Y., Marion, G. H., Phillips, M. M., et al. 2013, ApJ, 766, 72
Hsiao, E. Y., Phillips, M. M., Marion, G. H., et al. 2019, PASP, 131, 014002
Huang, C. D., Riess, A. G., Yuan, W., et al. 2020, ApJ, 889, 5
Jha, S., Riess, A. G., & Kirshner, R. P. 2007, ApJ, 659, 122
Johansson, J., Cenko, S. B., Fox, O. D., et al. 2021, ApJ, 923, 237
Jones, D. O., Riess, A. G., & Scolnic, D. M. 2015a, ApJ, 812, 31
Jones, D. O., Riess, A. G., Scolnic, D. M., et al. 2018a, ApJ, 867, 108
Jones, D. O., Scolnic, D. M., Foley, R. J., et al. 2019, ApJ, 881, 19
Jones, D. O., Scolnic, D. M., Riess, A. G., et al. 2017, ApJ, 843, 6
Jones, D. O., Scolnic, D. M., Riess, A. G., et al. 2018b, ApJ, 857, 51
Jones, D. O., Scolnic, D. M., & Rodney, S. A. 2015b, PythonPhot: Simple DAOPHOT-type Photometry in Python, Astrophysics Source Code Library, ascl:1501.010
Kattner, S., Leonard, D. C., Burns, C. R., et al. 2012, PASP, 124, 114
Kelly, P. L., Hicken, M., Burke, D. L., Mandel, K. S., & Kirshner, R. P. 2010, ApJ, 715, 743
Kelsey, L., Sullivan, M., Smith, M., et al. 2021, MNRAS, 501, 4861
Kenworthy, W. D., Jones, D. O., Dai, M., et al. 2021, ApJ, 923, 265
Kessler, R., Bassett, B., Belov, P., et al. 2010, PASP, 122, 1415
Kessler, R., Narayan, G., Avelino, A., et al. 2019, PASP, 131, 094501
Kim, Y.-L., Smith, M., Sullivan, M., & Lee, Y.-W. 2018, ApJ, 854, 24
Kirshner, R. P. 2010, in Dark Energy: Observational and Theoretical Approaches, ed. P. Ruiz-Lapuente (Cambridge: Cambridge Univ. Press), 151
Konchady, T., Oelkers, R. J., Jones, D. O., et al. 2022, ApJS, 258, 24
Krisciunas, K., Contreras, C., Burns, C. R., et al. 2017, AJ, 154, 211
Krisciunas, K., Garnavich, P. M., Stanishev, V., et al. 2007, AJ, 133, 58
Krisciunas, K., Suntzeff, N. B., Phillips, M. M., et al. 2004, AJ, 128, 3034
Krist, J. E., Hook, R. N., & Stoehr, F. 2011, Proc. SPIE, 8127, 81270J
Kurtz, M. J., & Mink, D. J. 1998, PASP, 110, 934
Lampeitl, H., Smith, M., Nichol, R. C., et al. 2010, ApJ, 722, 566
Lasker, J., Kessler, R., Scolnic, D., et al. 2019, MNRAS, 485, 5329
Lavaux, G., & Hudson, M. J. 2011, MNRAS, 416, 2840
Lewis, A., & Bridle, S. 2002, PhRvD, 66, 103511
Lira, P., Suntzeff, N. B., Phillips, M. M., et al. 1998, AJ, 115, 234
Mandel, K. S., Narayan, G., & Kirshner, R. P. 2011, ApJ, 731, 120
Mandel, K. S., Scolnic, D. M., Shariff, H., Foley, R. J., & Kirshner, R. P. 2017, ApJ, 842, 93
Mandel, K. S., Thorp, S., Narayan, G., Friedman, A. S., & Avelino, A. 2022, MNRAS, 510, 3939
Mandel, K. S., Wood-Vasey, W. M., Friedman, A. S., & Kirshner, R. P. 2009, ApJ, 704, 629
Marion, G. H., Höflich, P., Gerardy, C. L., et al. 2009, AJ, 138, 727
Martin, D. C., Fanson, J., Schiminovich, D., et al. 2005, ApJL, 619, L1
Nicolas, N., Rigault, M., Copin, Y., et al. 2021, A&A, 649, A74
Pan, Y.-C., Sullivan, M., Maguire, K., et al. 2014, MNRAS, 438, 1391
Perlmutter, S., Aldering, G., Goldhaber, G., et al. 1999, ApJ, 517, 565
Persson, S. E., Murphy, D. C., Krzeminski, W., Roth, M., & Rieke, M. J. 1998, AJ, 116, 2475
Pesce, D. W., Braatz, J. A., Reid, M. J., et al. 2020, ApJL, 891, L1
Peterson, E. R., Kenworthy, W. D., Scolnic, D., et al. 2021, arXiv:2110.03487
Planck Collaboration, Aghanim, N., Akrami, Y., et al. 2020, A&A, 641, A6
Phillips, M. M. 1993, ApJL, 413, L105
Phillips, M. M. 2012, PASA, 29, 434
Phillips, M. M., Contreras, C., Hsiao, E. Y., et al. 2019, PASP, 131, 014001
Phillips, M. M., Lira, P., Suntzeff, N. B., et al. 1999, AJ, 118, 1766
Pierel, J. D. R., Jones, D. O., Dai, M., et al. 2021, ApJ, 911, 96
Ponder, K. A., Wood-Vasey, W. M., Weyant, A., et al. 2021, ApJ, 923, 197
Postman, M., Coe, D., Benítez, N., et al. 2012, ApJS, 199, 25
Pskovskii, I. P. 1977, SvA, 21, 675
Rest, A., Scolnic, D., Foley, R. J., et al. 2014, ApJ, 795, 44
Rest, A., Stubbs, C., Becker, A. C., et al. 2005, ApJ, 634, 1103
Riess, A. G., Filippenko, A. V., Challis, P., et al. 1998, AJ, 116, 1009
Riess, A. G., Macri, L. M., Hoffmann, S. L., et al. 2016, ApJ, 826, 56
Riess, A. G., Press, W. H., & Kirshner, R. P. 1996, ApJ, 473, 88
Riess, A. G., Yuan, W., Macri, L. M., et al. 2021, arXiv:2112.04510
Rigault, M., Aldering, G., Kowalski, M., et al. 2015, ApJ, 802, 20
Rigault, M., Brinnel, V., Aldering, G., et al. 2020, A&A, 644, A176
Rigault, M., Copin, Y., Aldering, G., et al. 2013, A&A, 560, A66
Rodney, S. A., Riess, A. G., Strolger, L.-G., et al. 2014, AJ, 148, 13
Roman, M., Hardin, D., Betoule, M., et al. 2018, A&A, 615, A68
Rose, B. M., Baltay, C., Hounsell, R., et al. 2021a, arXiv:2111.03081
Rose, B. M., Rubin, D., Strolger, L., & Garnavich, P. M. 2021b, ApJ, 909, 28
Schlafly, E. F., & Finkbeiner, D. P. 2011, ApJ, 737, 103
Schlafly, E. F., Finkbeiner, D. P., Jurić, M., et al. 2012, ApJ, 756, 158
Scolnic, D., Brout, D., Carr, A., et al. 2021, arXiv:2112.03863
Scolnic, D., Casertano, S., Riess, A., et al. 2015, ApJ, 815, 117
Scolnic, D., & Kessler, R. 2016, ApJL, 822, L35
Scolnic, D. M., Jones, D. O., Rest, A., et al. 2018, ApJ, 859, 101
Siebert, M. R., Foley, R. J., Jones, D. O., et al. 2019, MNRAS, 486, 5785
Skrutskie, M. F., Cutri, R. M., Stiening, R., et al. 2006, AJ, 131, 1163
Smith, M., D'Andrea, C. B., Sullivan, M., et al. 2020, AJ, 160, 267
Solak, H., Kessler, R., & Jones, D. O. 2021, PASP, 133, 024001
Stanishev, V., Goobar, A., Amanullah, R., et al. 2018, A&A, 615, A45
Stetson, P. B. 1987, PASP, 99, 191
Stritzinger, M. D., Phillips, M. M., Boldt, L. N., et al. 2011, AJ, 142, 156

Sullivan, M., Conley, A., Howell, D. A., et al. 2010, MNRAS, 406, 782
Sullivan, M., Le Borgne, D., Pritchet, C. J., et al. 2006, ApJ, 648, 868
The Dark Energy Survey Collaboration 2005, arXiv:astro-ph/0510346
Thorp, S., Mandel, K. S., Jones, D. O., Ward, S. M., & Narayan, G. 2021, MNRAS, 508, 4310
Tripp, R. 1998, A&A, 331, 815
Uddin, S. A., Burns, C. R., Phillips, M. M., et al. 2020, ApJ, 901, 143
Villar, V. A., Hosseinzadeh, G., Berger, E., et al. 2020, ApJ, 905, 94
Weinberg, D. H., Mortonson, M. J., Eisenstein, D. J., et al. 2013, PhR, 530, 87
Weyant, A., Wood-Vasey, W. M., Joyce, R., et al. 2018, AJ, 155, 201
Wiseman, P., Smith, M., Childress, M., et al. 2020, MNRAS, 495, 4040
Wong, K. C., Suyu, S. H., Chen, G. C. F., et al. 2020, MNRAS, 498, 1420
Wood-Vasey, W. M., Friedman, A. S., Bloom, J. S., et al. 2008, ApJ, 689, 377
Zackay, B., Ofek, E. O., & Gal-Yam, A. 2016, ApJ, 830, 27
Zuntz, J., Paterno, M., Jennings, E., et al. 2015, A&C, 12, 45